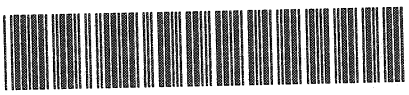

CERN/LHCC 2002-004
RD39 Status Report
09 January 2002

RD39 STATUS REPORT

RD39 Collaboration

K. Borer, S. Janos and K. Pretzl
Laboratorium für Hochenergiephysik der Universität Bern, Sidlerstarsse 5, CH-3012 Bern, Switzerland

B. Dezillie and Z. Li*
Brookhaven National Laboratory, Upton, NY 11973-5000, USA

C. da Viá, V. Granata, S. Watts
Brunel University, Uxbridge, Middlesex UB8 3PH, UK

L. Casagrande, P. Collins, S. Grohmann, E. Heijne, C. Lourenço, T.O. Niinikoski*, B. Perea Solano, V.G. Palmieri and P. Sonderegger
CERN, CH-1211 Geneva, Switzerland

E. Borchi, M. Bruzzi and S. Pirollo
Dipartimento di Energetica, Universitá di Firenze, I-50139 Firenze, Italy

S. Chapuy and Z. Dimcovski
Department de Radiologie, Universite de Geneve, CH-1211 Geneva, Switzerland

W. Bell, S.R.H. Devine, V. O'Shea, G. Ruggiero and K. Smith
Department of Physics and Astronomy, University of Glasgow, Glasgow G12 8QQ, UK

P. Berglund
Low Temperature Laboratory, Helsinki University of Technology, FI-02150 Espoo, Finland

W. de Boer, A. Dierlamm, E. Grigoriev, F. Hauler, S. Heising and L. Jungermann
IEKP University of Karlsruhe, D-76128 Karlsruhe, Germany

M. Abreu, P. Rato Mendes and P. Sousa
LIP, Av. E. Garcia, P-1000 Lisbon, Portugal

V. Cindro, M. Mikuz and M. Zavrtanik
Jozef Stefan Institute, Exp. Particle Physics Dep., PO Box 3000, 1001 Ljubljana, Slovenia

A. Esposito, I. Konorov, Rita De Masi and S. Paul
Physik Department E18, Technische Universität München, D-85748 Garching, Germany

S. Buontempo, N. D'Ambrosio and S. Pagano
Dipartimento di Fisica, Universitá "Federico II" and INFN, I-80125 Napoli, Italy

V. Eremin and E. Verbitskaya
Ioffe Physico-Technical Institute, Russian Academy of Sciences, St. Petersburg 194021, Russia

---

* co-spokesperson

Executive summary

The Part I of this report describes the status of the RD39 Collaboration, focusing on the results and achievements since our last Status Report, which was presented in January 2000. The Part II describes our proposed new program and the planned extension of the present projects.

The activities of RD39 evolved during the years 2000 and 2001 towards 3 projects in common with the NA60, COMPASS and TOTEM/CMS experiments. In addition to these, the collaboration continued the fundamental research of heavily irradiated silicon detectors at low temperatures, carried out presently in the form of two projects, called Basic Research, and Device Physics.

After the initial discovery of the recovery of the charge collection efficiency (CCE) of radiation damaged silicon at low temperatures (Lazarus effect), the RD39 collaboration has explored and exploited the benefits of low temperatures for silicon detectors. Cooling to the optimum temperature of 130 K yields the following advantages:

- Reduction of the charged fractions of radiation-induced deep-level defects in the active volume of the detector
- Effective and easily controllable manipulation, by free carrier injection, of the charged fraction of the deep-level defects
- Detector edge surface passivation effect, due to the charged deep levels, allows to operate at high voltage
- Negligible bulk and surface current generation rate, even after large damage
- Much higher mobility of free carriers (a factor of about 5 for both carriers at 130 K)
- High thermal conductivity of silicon (a factor of 3 between 300 K and 130 K).

The first four of these items are discussed extensively in Sections 2 and 3 of the present report. A series of models is presented in Section 2, which theoretically explains the Lazarus effect and related phenomena at low temperatures. The models are self-consistent with each other, and agree with other measurements using Transient Current Techniques (TCT), Photo Induced Current Transient Spectroscopy (PICTS), and Deep Level Transient Spectroscopy (DLTS), although the results of DLTS fail to agree quantitatively with some of the parameters extracted from the fits of the Lazarus effect model and of the temperature dependence of the reverse current. Measurements of the Lorentz angle up to 8 T and down to 78 K indicate that the Hall scattering factor requires further study.

Two tracker detectors were designed, constructed and successfully tested for intense primary beams of lead ions and protons, in the framework of the RD39/NA60 Common project. These may be considered as a proof of the principle and of the feasibility of small tracking devices for very high fluences of charged particles. The ion beam tracker survived the lead ion radiation dose of 90 Grad in the most exposed spots of the sensors (see Section 4).

The proton beam tracker uses deep submicron CMOS preamplifiers operating at a temperature close to that of the microstrip sensors. These amplifiers were designed by the MIC group to be as fast as the technology permits, and cryoacceleration was seen to make the circuits even faster, reducing their shaping time to 3.5 ns, as described in Section 4. Similar

effects were observed in the APV25 readout circuits of the RD39/COMPASS Common project (Section 7).

The low-mass module design and assembly techniques were developed in the RD39/TOTEM project. The results indicate that at low temperatures the module mass may be reduced because of the high thermal conductivity of silicon, and because the sensor power dissipation is minimal. An important factor in the mass reduction is also the integration of a cooling microtube in the module structure (see Section 6).

The RD39/TOTEM sensors need to operate at a few mm distance from the LHC beam, and the dead area of their edge must be minimized. Tests were carried out in view of fabricating edgeless sensors, and the promising results are also reported in Section 6.

The development of efficient low-mass cooling systems and detector module construction techniques has been an important part of the projects in common with the three experiments. In the future it can be expected that this and other engineering questions will require additional attention. These projects, together with the fundamental research, pave the way towards constructing an entirely cryogenic tracker inside the solenoid of a detector, at a hadron collider with very high luminosity, such as the upgraded Super LHC with a planned luminosity of 10^{35} $cm^{-2}s^{-1}$. The conceptual design of such a tracker will be discussed in Section 9, which describes also the planned development work toward this major goal.

The extension of the present projects is described in Section 10. The proposed future work in the Device Physics and Basic Research projects will focus on the understanding of the radiolytic defects and their kinetics at low temperatures, and on the design of segmented sensors with extreme radiation hardness. Classical and new techniques of characterization will be used: CCE, TCT and DLTS measurements will be supplemented by PICTS and EPR studies, and much faster TCT techniques is under development. The fast TCT will be compatible both with the higher mobility in silicon at low temperatures, and with the requirements of the future colliders with very high luminosity. The new EPR method is based on microwave photoconductivity rather than transverse susceptibility, and has an enhancement of 10^4 in sensitivity in silicon.

The TOTEM and COMPASS projects will allow to set important milestones in the near and medium term, and they will provide a practical framework for the testing of the ideas for future large cryogenic trackers.

In many respects silicon behaves at 130 K in a manner somewhat similar to diamond at higher temperatures, but the processing technology is much better developed, and the cost and availability of the raw material of the sensors are also much more favorable. As the sensing area and the number of readout channels in the future trackers are likely to increase substantially from those of the trackers presently built for LHC, the RD39 considers the cost as an important parameter, and will therefore give preference to simpler processing of the sensors and to standard commercial processing of the readout electronics. New and more exotic materials, however, will not be excluded, in view of their possible benefits in the inmost layers of the LHC detectors, where the fluence may be too high even for cryogenic silicon detectors. Work focusing on the low-temperature characterization and operation was already started on new epitaxial SiC, as reported in Section 10.

PART I

Status of RD39

1 INTRODUCTION

RD39 presented the last Status Report [1] in January 2000, together with a request for extension, which was recommended by LHCC and was approved by RB for two years. The present document describes the work carried out since then, and we have a great pleasure to report excellent progress in the proposed work. We note also that the program of work was expanded after the original approval, to include important contributions in the design, construction, tests and operation of two beam trackers for the NA60 experiment, which was approved only later in 2000.

The main activities of RD39 evolved during the years 2000 and 2001 towards 3 projects in common with the NA60, COMPASS and TOTEM/CMS experiments. These profited from shared resources that would have been insufficient if the projects would have been independent. In addition to these, the collaboration continued the fundamental research of heavily irradiated silicon detectors at low temperatures, carried out presently in the form of two projects, named Basic Research, and Device Physics. These programs were conducted mainly outside CERN, but they also profited from shared knowhow and expertise.

Our theoretical and experimental studies of heavily irradiated silicon at low temperatures, carried out in the framework of the two last mentioned projects, progressed substantially. Theoretical models were developed for the following:

1. Temperature dependence of the leakage current in irradiated detectors;
2. Electric field distribution in heavily irradiated detectors;
3. Simulation of the temperature dependence of the charge collection efficiency in a wide temperature range;
4. Polarization of silicon detectors by minimum ionizing particles;
5. Electric field shape during free carrier injection.

The models were used for extracting the deep level defect parameters from fits to our experimental data. These are summarized in Sections 2. In Section 3 we present new CCE data and results on the measurement of the Lorentz angle at high field down to 78 K; we also summarize findings of Photo Induced Current Transient Spectroscopy (PICTS) studies of defect clusters formed under irradiation by fast neutrons.

Section 4 describes two microstrip tracker detectors, which were designed, constructed and successfully tested for intense primary beams of lead ions and protons of the RD39/NA60 Common project. The operation of these in the physics runs was also assured, and the data analysis is underway. The tracker modules feature small numbers of strips, with very fast strip signals and high-speed readout. The proton beam tracker uses deep submicron CMOS preamplifiers operating at a temperature close to that of the microstrip sensors, and cryoacceleration reduced their shaping time to a 3.5 ns.

We also applied the cryogenic silicon sensor technology to monitoring the position and intensity of the NA60 lead ion beam, as reported in Section 5. Such devices could be used for monitoring the luminosity in the high-flux regions of the LHC experiments, and they could also

be used in LHC magnet cryostats, both for luminosity monitoring and for beam loss monitoring.

In Section 6 we shall describe the low-mass module design and assembly techniques, which were developed in the RD39/TOTEM Common project. At low temperatures the module mass may be reduced because of the high thermal conductivity of silicon, and because the sensor power dissipation is minimal. An important factor in the mass reduction is also the integration of a cooling microtube in the module structure. The RD39/TOTEM sensors need to operate at a few mm distance from the LHC beam, and the dead area of their edge must be minimized. Tests were carried out in view of fabricating edgeless sensors, and the promising results are also reported in Section 6.

Section 7 concludes the Part I of this report by reporting the progress of the COMPASS tracker, which will operate in the intense M2 beams of muons and hadrons, with more than 10^8 particles/spill. The APV25 readout ASIC of CMS was characterized at 130 K, and cryoacceleration effects were observed.

Note concerning the term "cryogenic" in this report

The cryogenic temperatures are defined somewhat arbitrarily to begin at 100 K, which is below the optimum temperature of 130 K for the Lazarus effect. We are, however, using the expressions "cryogenic detector" and "cryogenic tracker" in our report. This can be justified because we are using cryogenic coolants, such as liquid N_2 and liquid Ar, for absorbing the heat from the detector modules. This term should therefore be taken in a more wide sense. Moreover, in the thermal design of the detectors we are using the technology and knowhow developed for cryogenic instrumentation.

Reference of Section 1

[1] K. Borer et al., *RD39 Status Report*, CERN/LHCC 2000-010, 6 January 2000

2 DEVICE PHYSICS STUDIES

The cooling of the detector is traditionally considered as a method to reduce the leakage current, which is a main factor influencing the performance of the detector, via the reduction of the signal-to-noise ratio. This statement is valid for the non-irradiated detectors processed on pure semiconductors, in particular on high-resistivity silicon, in which the concentration of deep levels is significantly lower than the effective charge density in the detector space charge region (SCR). As usual, the leakage current in such a detector is low enough, and the component of the current generated in the SCR has a negligible influence on any other characteristics, such as

- the thickness of the SCR;
- electric field distribution in the SCR;
- the charge collection efficiency.

In the case of irradiated detectors, the increase of the leakage current is mainly due to the introduction of high concentrations of radiation-induced deep levels, and therefore the cooling of the detector may lead to additional effects. There are several reasons for that:

- In irradiated detectors the leakage current is mainly generated in the bulk. The high density of the bulk-generated current leads to a high concentration of free carriers in the detector SCR.
- The high concentration of free carriers in the SCR influences strongly the steady state occupancy of deep levels in the forbidden gap of silicon.
- The operation of the detector at low temperature will make the free carrier trapping effect stronger, and could magnify the influence of radiation-induced deep levels on the detector characteristics.

These features motivated a detailed investigation of the detector performance at low temperatures, without neglecting any factors such as the leakage current. In view of this, several studies were carried out, using irradiated detectors, of the temperature and dose dependences of the CCE, reverse leakage current, electric field, polarization, and of the dependence of these parameters on current density injected deliberately for the manipulation of the space charge.

2.1 Temperature dependence of the leakage current in irradiated detector

Investigations on the reverse current were carried out for silicon p^+-n-n^+ detectors manufactured at BNL from standard Wacker Si with a resistivity of 1.2-3 kOhm·cm. The typical current-voltage (I-V) curves of investigated detectors at RT are presented in Figure 1. The measurements of the temperature dependence of the reverse current were performed in the range of 200 to 400 K, and at a bias voltage larger than the full depletion voltage (V_{fd}). Therefore, at any temperature, the measured current is due to carrier generation in the entire volume of the detector (bulk generation current I_{gen}).

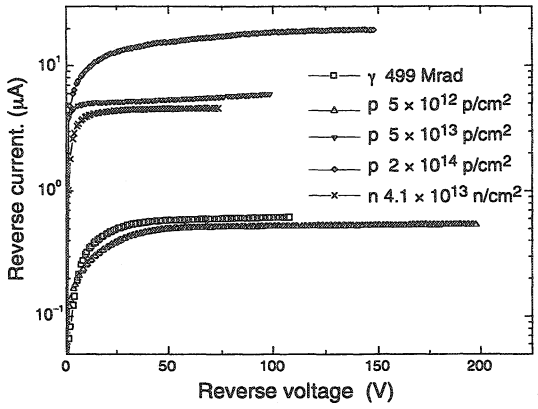

Figure 1: Current-voltage characteristics of irradiated detectors at room temperature.

According to Shockley-Read-Hall (SRH) statistics [1], the bulk-generated current is related to the parameters of the deep levels (DL): the activation energy E_t, and the carrier capture cross sections for electrons (σ_e) and holes (σ_h).

In the case of negligible concentrations of free carriers in the bands ($n, p \approx 0$, such as in the case of SCR), the current generation rate for a single level is:

$$U = \frac{\sigma_e \sigma_h v_{th} n_i N_t}{\sigma_e \exp\left(\frac{E_t - E_i}{kT}\right) + \sigma_h \exp\left(\frac{E_i - E_t}{kT}\right)}, \quad (1)$$

where n_i is the intrinsic free carrier concentration, E_i is the midgap energy, v_{th} are thermal velocities of electrons and holes, respectively; $E_c - E_t$ and E_t - E_v are activation energies for carrier transitions between DL and conduction/valence bands; k is the Boltzmann constant, and T is the temperature. In the case of multiple energy levels, each level gives an independent contribution to the total generation rate of the current $U = \sum_i U_i$.

It follows from Eq. (1) that the dominant parameter of DL, which controls the temperature dependence of generation current $I(T)$, is the DL energy E_t. However, for the correct analysis of the experimental data, the temperature dependences of the fundamental parameters — thermal velocity $v_{th} \sim T^{1/2}$ and intrinsic concentration $n_i \sim \exp(-E_g/2kT)$ (where E_g is the energy band gap) — have been taken into account. The influence of T on σ is still not quite clear and there are different experimental estimations of the temperature dependence of σ. A theoretical study [2] suggests a power function $\sigma \sim T^m$ with a m ranging from –3 to 0. Therefore, for the modeling of $I(T)$ based on Eq. (1), m was set as a free variable to obtain the optimal fit of the experimental data (finally m = –2 was used).

Diode detectors were exposed to γ, p, and n radiation. Among the samples, the γ-irradiated diodes feature a reverse current which corresponds to the model of carrier generation via a single energy level. The temperature dependence of the reverse current, for a detector irradiated by γ-rays to a dose of 499 Mrad), is close to an exponential of $1/T$ in the range of four orders of magnitude of current, as predicted by Eq. (1). This confirms that γ-rays produce only point defects in the crystal lattice. On the other hand, neutrons generate mainly defect clusters, and protons generate both point defects and defect clusters [3].

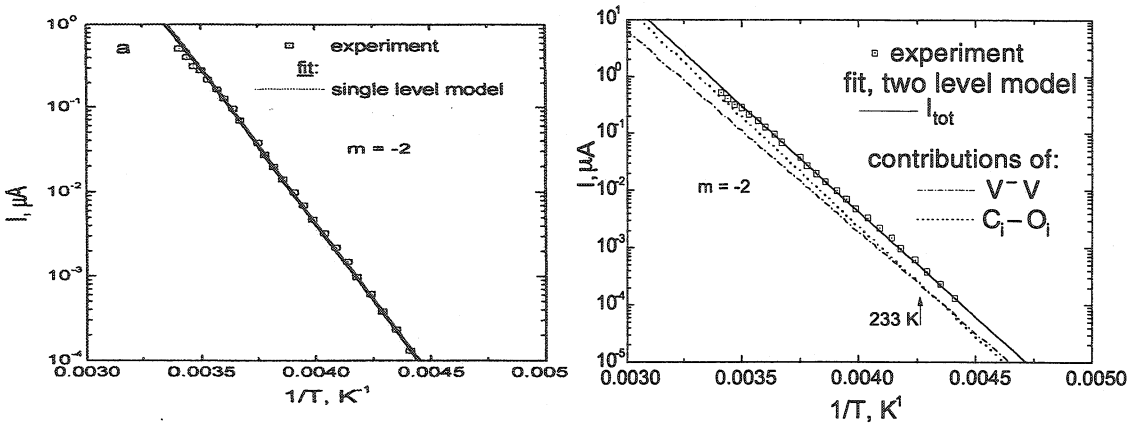

Figure 2: Experimental dependence of the reverse current on temperature of Si detector irradiated by γ-rays and its fits according to a single-level (left) and two-level generation models (right).

The two-level fit of $I(T)$ for the γ-irradiated detector, shown on the right in, was performed using the parameters of VV^- and the C_i-O_i complexes listed in Table 1. The contribution of the C_i-O_i complexes to the total current, right) dominates from RT down to 233 K, whereas the divacancy level controls the current at lower temperatures.

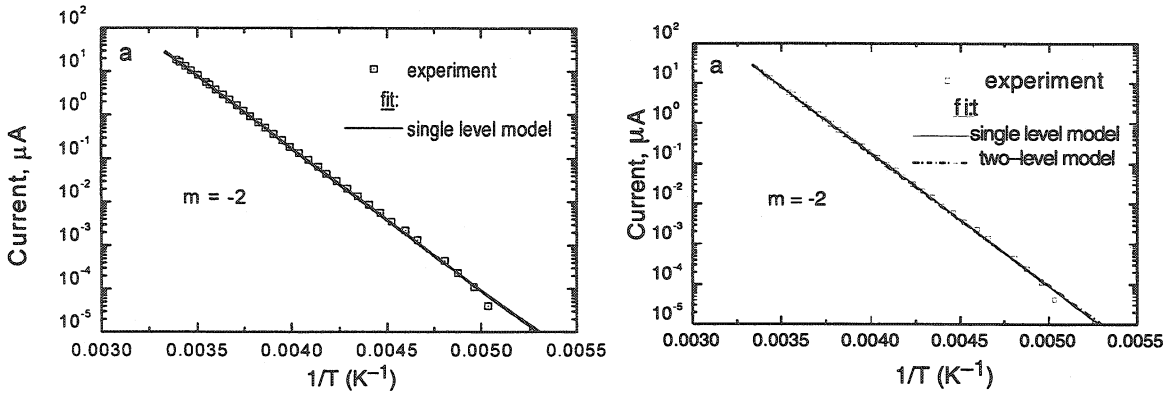

Figure 3: Experimental dependence of the reverse current on temperature of Si detector # 923-D39 irradiated by proton fluence of $2 \cdot 10^{14}$ cm^{-2} and the corresponding fits to the single-level (left) and two-level generation models (right). On the horizontal scale is displayed the inverse temperature in the units K^{-1}, in both cases.

The experimental $I(T)$ for detectors irradiated by protons, and their single-level model fits with parameters specified in Table 1, are shown in Figure 3. The resulting reverse current activation energy for proton-irradiated detectors is smaller than that for γ-irradiated detectors. This suggests that a second generation channel, with an energy level just adjacent to the mid gap, may contribute to the reverse current. This is reasonable because of the difference in the dominant defects introduced by γ-rays and protons (point defects as compared to cluster defects, respectively), and because of the corresponding changes evinced in deep level spectra measured by DLTS (Figure 4) [3]. The deep level defined in [4] as a hole trap DL11 (E_v + 0.52 eV) is observed both in Si irradiated by protons and in Si irradiated by neutrons [4], [5]. The fit of the reverse current, using a two-level generation current model, for detectors irradiated by protons, is shown on the right in Figure 3. The two energy levels are those of VV^- and DL11 (with DL11 at E_v + 0.515 eV, Table 1). The VV^- dominates in the reverse current at $T > 237$ K.

A. γ-irradiated Si, dose 499 Mrad			
Parameter	Single-level model	Two-level model	
Defect label		VV^-	C_i-O_i
R		$[VV^-]/[C_i\text{-}O_i] = 0.05$	
$E_c - E_t$, eV	0.395	0.42	0.76
E_t, eV	0.725	0.70	0.36
σ, cm^2	$1\cdot10^{-13}$	$1\cdot10^{-13}$	$1\cdot10^{-13}$
N_t, cm^{-3}	$2.4\cdot10^{14}$	$3.2\cdot10^{13}$	$6.4\cdot10^{14}$

B. Proton irradiated Si, fluence $2\cdot10^{14}$ cm^{-2}			
Parameter	Single-level model	Two-level model	
Defect label		VV^-	DL11
R		$[VV^-]/[DL11] = 20$	
$E_c - E_t$, eV	0.463	0.420	0.605
E_t, eV	0.657	0.700	0.515
σ, cm^2	$1\cdot10^{-13}$	$1\cdot10^{-13}$	$1\cdot10^{-14}$
N_t, cm^{-3}	$6.2\cdot10^{14}$	$2.4\cdot10^{15}$	$1.2\cdot10^{14}$

C. Neutron irradiated Si, fluence 4.2 10^{13} cm^{-2}			
Parameter	Single-level model	Two-level model	
Defect label		VV^-	DL11
R		$[VV^-]/[DL11] = 10$	
$E_c - E_t$, eV	0.471	0.420	0.606
E_t, eV	0.649	0.700	0.514
σ, cm^2	$1\cdot10^{-13}$	$1\cdot10^{-13}$	$1\cdot10^{-14}$
N_t, cm^{-3}	$1.1\cdot10^{14}$	$3.9\cdot10^{14}$	$3.9\cdot10^{13}$

Table 1: Parameters of deep levels derived from the fits of the reverse current of Si detectors irradiated by gamma rays, protons or neutrons. In all cases $m = -2$ (see text).

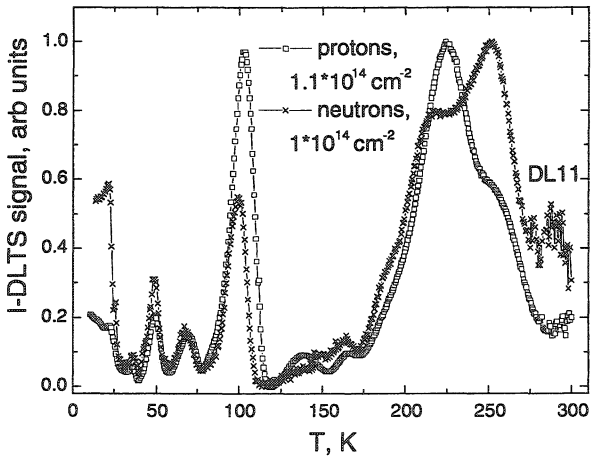

Figure 4: Experimental normalized I-DLTS spectra of silicon detectors irradiated by protons and neutrons.

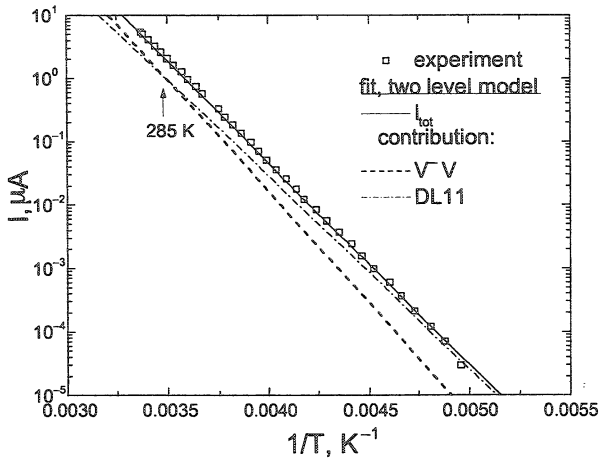

Figure 5: Experimental dependence of the reverse current on temperature of Si detector # 899-97 irradiated by neutron fluence of $4.2 \cdot 10^{13}$ cm^{-2}, and the corresponding fit to the two-level generation model.

An even stronger contribution of the DL11 is nicely observed for a detector irradiated by neutrons up to a fluence of $4.2 \cdot 10^{13}$ cm^{-2}. The single-level generation model yields $E_a \sim 0.65$ eV (Table 1) which is slightly reduced as compared to that for Si detectors irradiated by protons. The two-level fit of the $I(T)$ curve (Figure 5) yields the concentration ratio $[VV^-]/[DL11] \sim 10$, indicating that the relative introduction rate of DL11 centers is enlarged, comparing with proton irradiation.

The analysis of the curves $I(T)$ yields absolute concentrations of DLs significantly higher than those predicted from their introduction rates determined using the DLTS method. One of the possible explanations is related with the unknown occupancy of the deep levels at the temperature where the DLTS peak is measured. Hence, the contribution of this level to the space charge concentration, which determines the thickness of depletion region and the reverse current, can hardly be estimated accurately from the DLTS measurements.

Finally it is possible to conclude that:

- For silicon detectors, irradiated by high-energy protons or by neutrons or γ-rays, the activation energy of the reverse current is in the range of 0.65 to 0.72 eV, evaluated in the framework of the SRH model of carrier generation. These values of E_a differ from the positions of known radiation-induced defects in the band gap. Hence, a reasonable model of the generation process requires partial contributions of two independent generation centers, with different concentrations for various types of radiation.
- For detector irradiated by γ-rays $E_a = 0.72$ eV, which is larger than that for the other types of radiation. The model for the generation current, proposed in this study, considers the contributions of VV^- and the C_i-O_i complexes, each positioned at ≥ 0.7 eV from the corresponding energy band.
- The generation current in detectors irradiated by neutrons or protons may be modeled by considering contributions of VV^- and a deep level adjacent to the mid-gap ($E_v + 0.52$ eV).
- The relative yield of the mid-gap defects is up to twice higher in the detectors irradiated by neutrons, comparing with those irradiated by protons.
- The values of the product σN_t, as determined from the analysis of the $I(T)$ curves for irradiated detectors, are significantly higher than those determined from the DLTS spectra.

2.2 Electric Field Distribution in Heavily Irradiated Silicon Detectors

The first observations of nonuniform electric field distribution in heavily neutron irradiated ($> 10^{14}$ n/cm^2) semiconductor detectors, featuring so-called double junction (DJ) [6] and double peak (DP) [7] effects (Figure 6), with physical considerations on their origin, were published in 1992 and 1995. The quantitative explanation of these effects was proposed in 2000 [8]. It is based on the properties of radiation-induced deep levels in silicon, which act as deep traps, and on the distribution of the thermally generated free carrier concentration in the detector bulk. The model predicts $E(x)$ at any reverse bias and at any temperature.

Model

The values of the following three variables are essential to the determination of the local effective concentration in space charge region (SCR) of the detectors:

- Steady state concentrations of charged deep donors (N^+_{DD}) and acceptors (N^-_{DA}), both depend on the temperature.
- The thermally generated bulk current, which depends on the concentration and spectra of the deep levels (DL) and on the temperature.

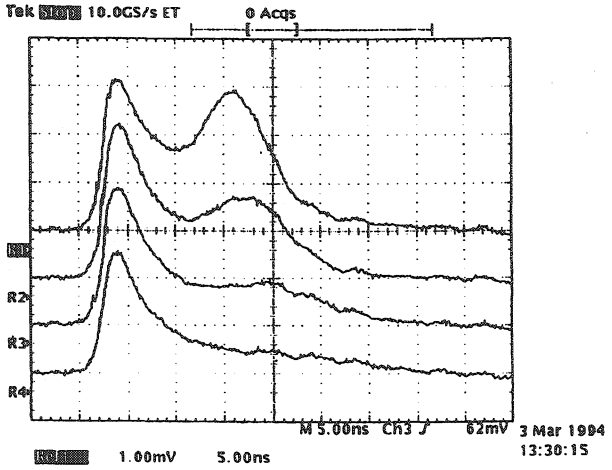

Figure 6: Current pulse response at different temperatures as measured in [7] for a neutron irradiated detector (fluence of $\Phi_n = 3.29\text{x}10^{13}$ cm^{-2}): R1 – 305 K, R2 – 280K, R3 – 260 K, R4 – 240 K. The reverse bias is 550 V. The charge is injected at the n$^+$ side, which is a high-field side after space charge sign inversion.

The physical idea to explain the DJ/DP effects is qualitatively illustrated in Figure 7. In Figure 7a, the regular electric field profile in fully depleted detector without DLs (non-irradiated) is shown. The electric field is close to uniform due to low concentration of shallow levels.

The thermally generated current

$$j = Gd \tag{2}$$

is constant along the SCR depth d, due to constant current generation rate G. However, its electron and hole components j_n and j_p are linearly distributed in the bulk (Figure 7b), as a consequence of the continuity equation

$$j_n = Gx; \quad j_p = G\,(d - x). \tag{3}$$

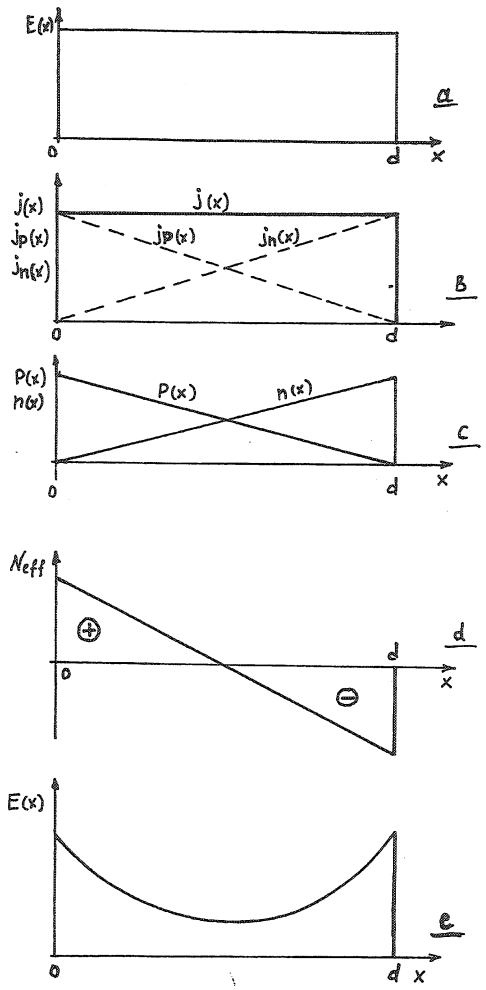

Figure 7: The diagrams illustrate the proposed model of the origin of double peak electric field distribution in a deep level rich detector. a) electric field distribution in fully depleted detector without DLs; b) the thermally generated current density distribution : j-total current, j_n and j_p the electron and hole current components respectively; c) free carrier density distribution; d) N_{eff} distribution; e) electric field distribution (p^+ contact is at x=0, and n^+ contact is at $x = d$.

Consequently, the concentrations of free carriers, which are proportional to the current components, are linearly distributed in the detector bulk as well, as is shown in Figure 7c.

This non-uniform free carrier distribution offers a strong support to the argument that, in a detector with high concentration of deep traps (N_{DA} acceptors and N_{DD} donors), the steady-state filling of these traps by trapped carriers will be non-uniform. Assuming the concentration of trapped carriers to be proportional to the concentration of free carriers, it becomes clear that in the part of the detector adjacent to the p^+-contact (at $x = 0$), the positive charge accumulated by the deep donors will be higher than the negative charge accumulated by the deep acceptors. Similarly, in the opposite end near the n^+-contact (at $x = d$), negative trapped charge will be dominant (Figure 7d). Finally, because the Poisson equation

$$\nabla \cdot \mathbf{E} = \frac{-eN_{eff}}{\varepsilon\varepsilon_0} \tag{4}$$

must be satisfied, two peaks do appear in the electric field distribution $E(x)$, as shown by Figure 7e. These are located in the SCR near the contacts of an over-depleted detector. In Eq. (4) ε_0 and ε are the permittivities of vacuum and silicon, respectively.

The same features of free carrier distribution can also be observed in a non-depleted detector. In this case the SCR is split into two regions which are adjacent to the contacts. The electrically neutral region (ENR) between the SCRs conducts the current generated in both SCRs, and maintain the higher hole concentration at the p^+ contact and, vice versa, higher electron concentration at the n^+ contact. This predominates the positive N_{eff} at the p^+ side and the negative N_{eff} at n^+ side. It is clear that such a detector structure will be double side sensitive at $V < V_{fd}$ as was observed in [6].

Modeling of DJ and DP effects

In the calculation of the electric field distribution $E(x)$, the system of equations includes the equations for local free carrier concentrations, contributing to the bulk generation current in proportion with their drift velocities which depend on the electric field. These and the effective concentration of space charge, with coordinate-dependent charged fractions of deep levels F^+, F^-

$$N_{eff}(x) = F^+(x)N_{DD} - F^-(x)N_{DA}, \tag{5}$$

together with the one-dimensional Poisson equation (4), were solved numerically.

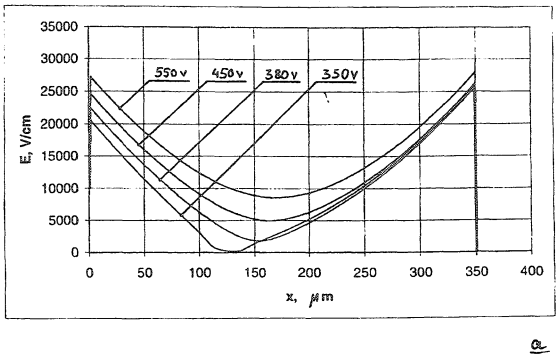

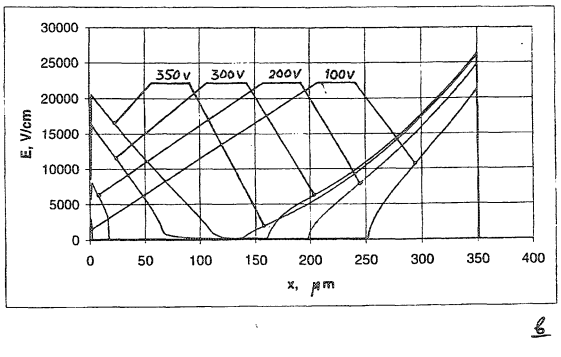

Figure 8: The calculated electric field distribution for the detector containing deep acceptor DA4 (E_c-0.52eV, $N_{DA} = 4x10^{15}$ cm^{-3}) and deep donor DD3 (E_v+0.52eV $N_{DD} = 4.6x10^{14}$ cm^{-3}) at different biases. a) $E(x)$ for a fully depleted detector (DP electric field distribution); b) $E(x)$ for a partially depleted detector (DJ effect).

The set of $E(x)$ shown in Figure 8 is calculated according to the model of a detector containing two deepest DLs: the acceptor level DA4 and the donor level DD3, assuming that the detector operates at a temperature of 305 K and at a bias V = 550 V, which correspond to the experimental condition for the pulse R1 presented in Figure 6.

Assuming in the first approximation of the analysis of the experimental current pulses that $x \propto t$ and $E \propto I$, the main features of the distribution of the field $E(x)$ in the detector observed in [7] are:

- the electric field has two maxima located at the p^+ and n^+ contacts;
- the magnitudes of E_{max} for both peaks are nearly equal;
- E_{min} is located close to the middle of the detector thickness.

The two free parameters, the concentrations of DA4 and DD3, were adjusted to obtain best qualitative coincidence with the two-peaked features of $E(x)$. The simulated $E(x)$ (Figure 8), at $T = 305$ K and $V = 550$ V, and with the parameters of the DLs listed in the figure caption, agrees well with the experimental data and confirms the concept developed here: the main process, which controls $E(x)$ in heavily irradiated detectors, is the interaction of the free carriers, originating and giving rise to the bulk generated current in the SCR, with deep trapping centers. It is also predicted by the calculation that a reduction in the applied bias V (curves for 450, 380, and 300 V) will lead to an increase of the inhomogeneity of $E(x)$; however, the DP distribution is still conserved.

At $V < 350$V the SCR becomes split between p^+ ($x = 0$) and n^+ ($x = d$) contacts with an electrically neutral region in between, whose thickness increases with decreasing bias. Such an electric field distribution is analogous with a structure with two junctions at the contacts, i.e. a DJ structure, as observed in [6]. The main junction forms at the n^+-contact with the main portion of the applied bias V dropping across it, and a smaller fraction of V is applied to the SCR at the p^+ contact.

The set of current responses of Figure 6, measured at different temperatures, clearly shows the main trend in the changes of $E(x)$ related to detector cooling:

- The second peak in the current response disappears. This fact indicates that the maximum of the electric field is still at the n^+ contact.
- At 240 K the electric field near the p^+ contact gradually falls down to a value close to 0.

Figure 9a presents the calculated $E(x)$ from 305K to 240K based on the parameters of DL (DA4 and DD3) as used above. The calculated $E(x)$ does not show the same features which follow from Figure 6. The $E(x)$ at p^+ contact becomes higher with cooling than that at the n^+ contact, and the $E(x)$ becomes more homogeneous. To adjust the model, the donor level DD3, which introduces the positive space charge near the p^+-contact, was replaced by a deeper donor DD2 with an activation energy of $E_v + 0.48$ eV, and the activation energy of DA4 was changed to $E_c - 0.525$eV, which is within the range of the experimental error for the DLTS technique. The main characteristics of the calculated $E(x)$ (Figure 9b) agree well with the experimental data. At $T = 305$ K the calculation shows a DP $E(x)$ with practically equal electric field maxima at both contacts. When cooling down, the sharp peak of $E(x)$ at the n^+ contact changes little, but the peak at the p^+ contact decreases with temperature and gets close to zero at 240 K, as was observed from the experimental pulse shape.

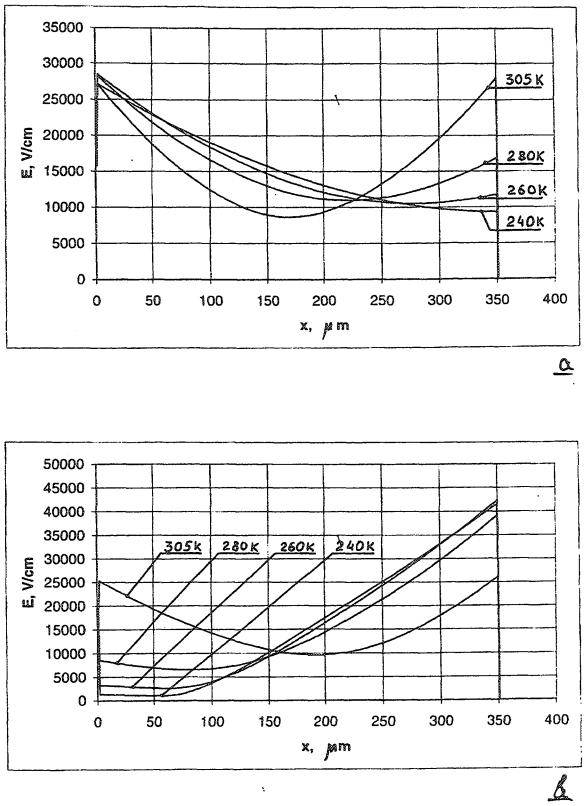

Figure 9: a) The calculated electric field profiles at different temperatures corresponding to the experiment shown in Fig. 3. The parameters of DL are the same as those for Fig. 2. b) The calculated electric field profiles at different temperatures for the detector containing DA4 (E_c-0.525eV, N_{DA} = 1.4x10^{15} cm^{-3}) and DD2 (E_v+0.48eV, N_{DD} = 3.2x10^{15} cm^{-3}).

The proposed model of the DP $E(x)$ is stable with respect to other deep and shallow levels. Calculations show that the DP $E(x)$ distribution is insensitive to the (C_i-O_i) and (V-V)$^-$ defects (Figure 10), even at extremely high concentrations around 10^{17} cm^{-3}. These defects yield some changes in $E(x)$ at T = 305 K only.

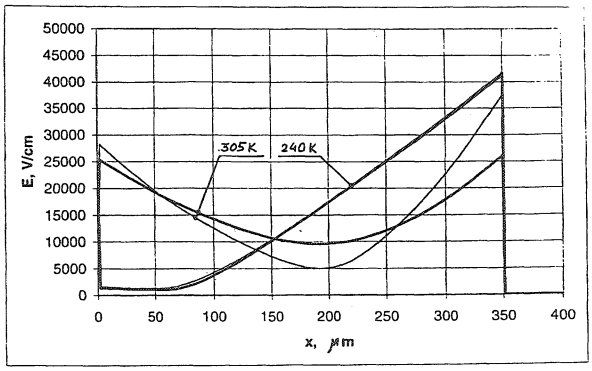

Figure 10: The calculated electric field profiles at T = 305 K and T = 240 K for the detector containing DA4 (E_c-0.525eV, N_{DA} = 1.4x10^{15} cm^{-3}) and DD2 (E_v+0.48eV N_{DD} = 3.2x10^{15} cm^{-3}) (thick lines). The $E(x)$ distributions (thin lines) for the same detector contains additionally the shallow acceptors –Boron (N_{SHA} = 7x10^{11} cm^{-3}) and the DLs which have the highest introduction rates: DA3 (V-V)$^-$ and DD1 (C_i-O_i) with overestimated high concentrations of N_{DA} = N_{DD} = 10^{17} cm^{-3}.

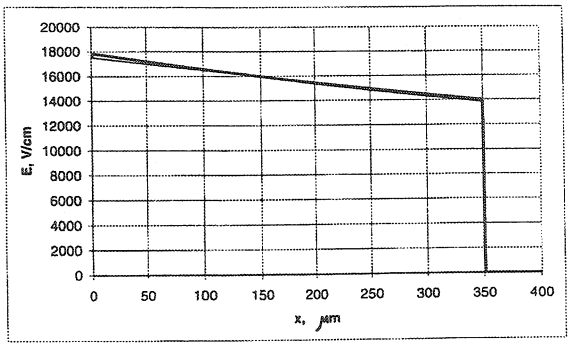

Figure 11: As calculated electric field profiles for the DLs concentrations following the DLTS data (Table 2). The thick line corresponds to $T = 305$ K, the thin line to $T = 240$ K. The parameters of centers are: shallow acceptors –Boron ($N_{SHA} = 7x10^{11}$ cm^{-3}); Deep levels: DA3 (E_c-0.4eV, $N_{DA} = 5x10^{14}$ cm^{-3}); DA4 (E_c-0.52eV, $N_{DA} = 1x10^{13}$ cm^{-3}).

This conclusion is nicely illustrated by the calculation of the electric field distribution (Figure 11) in the detector which contains the deep levels corresponding to their introduction rates obtained from C-DLTS data listed in Table 2 from [8]. The simulation does not show a DP-$E(x)$. Moreover, it does not even predict a space charge sign inversion, and instead the $E(x)$ decays linearly to the n^+ contact. This fact is a strong argument for the questioning of the introduction rates for the DLs, as determined from the DLTS studies.

DL label	DL defect	Type of DL	E_t eV	σ_e cm^{-2}	σ_h cm^{-2}	g cm^{-1}	F^+, F^- (300K)	gF cm^{-1}	Method	Ref
DA1	(V-O)	A	E_c-0.176	$1.4x10^{-14}$	?	1.1	$1.6x10^{-8}$	$1.8x10^{-8}$	I-DLTS, TSC	[3]
DA2	$(V-V)^-$	A	E_c-0.224	$7x10^{-16}$	?	1.5	$1x10^{-7}$	$1.5x10^{-7}$	I-DLTS, TSC	[3]
DA3	$(V-V)^-$	A	E_c-0.424	$2x10^{-15}$	?	1.5	$2.6x10^{-4}$	$3.9x10^{-4}$	I-DLTS, TSC	[3]
		A	E_c-0.4			1.5			TCT	[9]
DA4	?	e-trap	E_c-0.52	?	?	0.03	$2.4x10^{-2}$	$7x10^{-4}$	TCT	[9]
DD1	(C_i-O_i)	D	E_v+0.36	$2.1x10^{-15}$	$2.5x10^{-15}$	1.1	$1.2x10^{-4}$	$1.3x10^{-4}$	I-DLTS, TSC	[3]
		h-trap	E_v+0.36		$1.2x10^{-15}$	2.3			TCT	[9]
DD2	?	h-trap	E_v+0.48	$>6x10^{-16}$	$5.5x10^{-15}$	0.08	$2.8x10^{-1}$	$2.2x10^{-2}$	C-DLTS	[3]
DD3	?	h-trap	E_v+0.53	?	$3x10^{-14}$	0.08	$8.5x10^{-1}$	$6.8x10^{-2}$	I-DLTS, TSC	[3]
		h-trap	E_v+0.51	?	$1x10^{-14}$	0.03	$6x10^{-1}$	$1.8x10^{-2}$	TCT	[5]

Note: in the case of unknown cross sections, their values were assumed as $1x10^{-15}$ cm^{-2}, for (C_i-O_i) defect σ_e corresponds to $T = 180$ K.

Table 2: The parameters of neutron-induced deep levels in silicon.

The model developed for the electric field distribution $E(x)$ in heavily irradiated detectors, based on interaction between the free carriers of the bulk generation current and deep traps in the SCR, shows that:

- The DP and DJ $E(x)$ have a common origin. The DP $E(x)$ at $V > V_{fd}$ transforms to DJ distribution at $V < V_{fd}$;

- The experimental results presented in this study are explained by the model of carrier trapping to deep levels: DA4 (E_c – 0.52 to 0.53 eV) and DD2 (E_v + 0.48 eV) observed in neutron irradiated silicon;
- Even at RT, the (C_i-O_i) and $(V\text{-}V)^-$ defects do not introduce any significant charge to SCR. At low temperatures (T < 300 K) their influence on the $E(x)$ is negligible.

2.3 Temperature dependence of charge collection efficiency in heavily irradiated silicon detectors: the Lazarus effect model

Experimental characteristics of detectors irradiated by an equivalent neutron fluence > 10^{14} cm^{-2}, which were measured in the temperature range of 300 K to 77 K [10], showed that along with the expected reduction of the bulk generation component of the reverse current, the increase of the charge signal with decreasing temperature reached the maximum value at about T_r =130 K (Figure 12 from [11]). This effect was named the Lazarus effect (after the Biblical tale). The value of T_r is only slightly dependent on Φ_n, whereas the maximum of CCE decreases with increasing fluence.

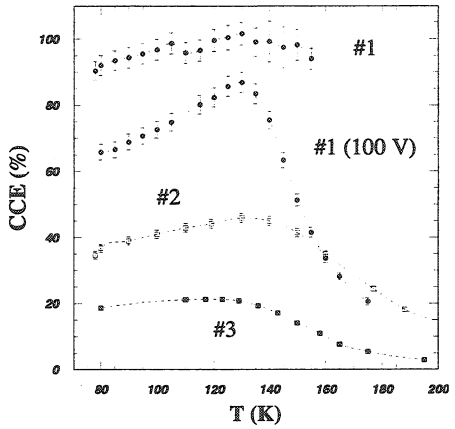

Figure 12: The Lazarus effect in silicon diodes irradiated by neutrons with 1 MeV equivalent fluences of $1 \cdot 10^{14}$ cm^{-2} (sample 1), $5 \cdot 10^{14}$ cm^{-2} (sample 2), and $1 \cdot 10^{15}$ cm^{-2} (sample 3).

The explanation of the Lazarus effect physics follows from two possible reasons for the degradation of the detector signal, due to the radiation damage in the detector:

- charge loss due to trapping of non equilibrium carriers by deep levels (DL) during the charge collection time;
- partial depletion of the detector in the case of high-resistivity bulk, where the non-depleted part of the detector thickness (neutral base region) acts as a capacitive divider.

Contribution of charge loss

The charge collection efficiency related with carrier trapping (CCE_t) (see e.g. [12]) is defined as

$$CCE_t = 1 - K[1 - \exp(-t_{dr}/\tau_t)] = F_t, \quad (6)$$

where t_{dr} is the charge collection (drift) time, τ_t is the trapping time constant and K is a coefficient which depends on the spatial distribution of e-h pairs generated initially by the event.

The temperature dependence of the CCE_t arises mainly from the dependence of τ_t on T, since t_{dr} is nearly constant due to saturation of the drift velocity v_{dr}. Since

$$\tau_t = \frac{1}{\sigma v_{th} N_{tt}}, \tag{7}$$

where σ is the effective carrier capture cross section for trapping centers with a total concentration N_{tt}, the temperature dependence of τ_t is related to all temperature dependencies of the involved parameters. Among these the power-law dependencies are theoretically predicted for σ [2] and v_{th}:

$$\begin{aligned} &\sigma = \sigma_0 (T/T_0)^{-\alpha}, \quad 0 \le \alpha \le 3 \\ &v_{th} \sim T^{1/2}. \end{aligned} \tag{8}$$

The effective concentration of trapping centers N_{tr} is a temperature dependent value. It is defined as the sum of the concentrations of both types of the traps: charged deep donors N^+_{DD} and deep acceptors N^-_{DA}, and neutral deep levels N^0_{DL}:

$$N_{tr} = \left|N^+_{DD}\right| + \left|N^-_{DA}\right| + N^0_{DL} \tag{9}$$

Note here that the capture cross section of charged centers can be a factor of 10 larger than that of neutral centers, implying that the charged centers will play a dominant role in trapping, if both concentrations are of the same order of magnitude. However, the estimations presented below show that the concentrations of charged fractions of deep levels decrease rapidly with decreasing temperature, and the neutral fraction becomes dominating in trapping.

Contribution of the geometrical factor

The second mechanism that controls the CCE, arises from a geometrical factor F_g usually defined as a ratio of the space chare region (SCR) depth w to the detector thickness d:

$$F_g = \frac{w}{d}. \tag{10}$$

For MIP detection the CCE term originating from a geometrical factor (CCE_g) is [13]:

$$\mathrm{CCE_g} = \frac{w^2}{d^2} = F_g^2. \tag{11}$$

According to Eq. (11), the temperature dependence of the $\mathrm{CCE_g}$ comes from the dependence of w^2 on T through:

$$w^2 = \frac{2\varepsilon\varepsilon_o V}{eN_{eff}}, \tag{12}$$

where ε and ε_0 are the permittivities of silicon and vacuum, respectively, e is the elementary charge and N_{eff} is the effective concentration of charged centers in the SCR. Hence, omitting the concentration of shallow levels

$$\left|N_{eff}\right| = \left|N^+_{DD}\right| - \left|N^-_{DA}\right|, \tag{13}$$

where N^+_{DD} and N^-_{DA} are the charged fractions of deep donor and deep acceptor concentrations, respectively.

Eqs. (9) and (13) define the concentrations N_{tt} and N_{eff}, which are responsible for the main factors of the total CCE:

$$CCE = CCE_t \cdot CCE_g. \quad (14)$$

The N_{tr} is the sum of the total concentrations of deep donors and acceptors (including charged fractions), whose values are large, whereas N_{eff} depends on the difference between the charged fraction concentrations only, also with large and close values. Hence, the trapping component CCE_t will be less sensitive than CCE_g to the changes with temperature of the charged deep level concentrations. This is a strong argument in favor of the statement that the Lazarus effect is related to the changes of N_{eff} with temperature.

Thus the physical mechanism of the Lazarus effect arises from the temperature dependence of the net effective concentration N_{eff} in the SCR of irradiated detectors. The absolute value of N_{eff} decreases with cooling and at the temperature T_r of the CCE maximum, the detector becomes fully depleted and keeps this state at any $T < T_r$. Obviously, since $F_g = 1$ when the detector is fully depleted, the second term F_t becomes dominating and therefore any changes of CCE(T) at $T < T_r$ are controlled by the trapping mechanism. In this temperature interval ($T < T_r$) the increase in carrier cross section as defined by Eq. (8) leads to a significant reduction of the trapping time constant and to the corresponding CCE decrease. These considerations are summarized in Table 3.

Temperature interval	Key factor of the CCE	Changes of N_{eff}	Detector status	CCE
$T > T_r$	$F_g < F_t$	Reduction of $(\lvert N_D^+ \rvert - \lvert N_A^- \rvert)_{DL}$	Non-depleted	$CCE \sim F_g(T)$
T_r	$F_g = 1$ $F_t < 1$	$N_{eff} = \frac{2\varepsilon\varepsilon_0 V}{ed^2}$	Fully depleted	$CCE \sim F_t(T)$
$T < T_r$	$F_g = 1$ $F_t < 1$	$\sim(\lvert N_D^+ \rvert - \lvert N_A^- \rvert)_{SL}$	Fully depleted	$CCE \sim F_t(T)$

Table 3: Competition of charge loss mechanisms in the temperature dependence of CCE.

Concentration of charged traps in the SCR of the detector

The key prediction of the proposed model is the decrease of the charged fraction concentrations for the deep levels of radiation-induced defects with decreasing temperature. Figure 13 illustrates the temperature dependence of the occupancy for the main deep traps, calculated according Shockley-Read-Hall (SRH) statistics [1] and using the expected value of the bulk generated current. The parameters for these deep levels of radiation induced defects DD2, DA3 (VV^-) and DA4 are listed in Table 2. The capture cross sections of DD2 and DA4, which are unknown as yet from any previous experimental data, were assumed to be $\sigma_n = \sigma_p = 10^{-15}$ cm^2. The results shown in Figure 13 are obtained for the bulk generation current corresponding to $\Phi_n = 1 \cdot 10^{14}$ cm^{-2}.

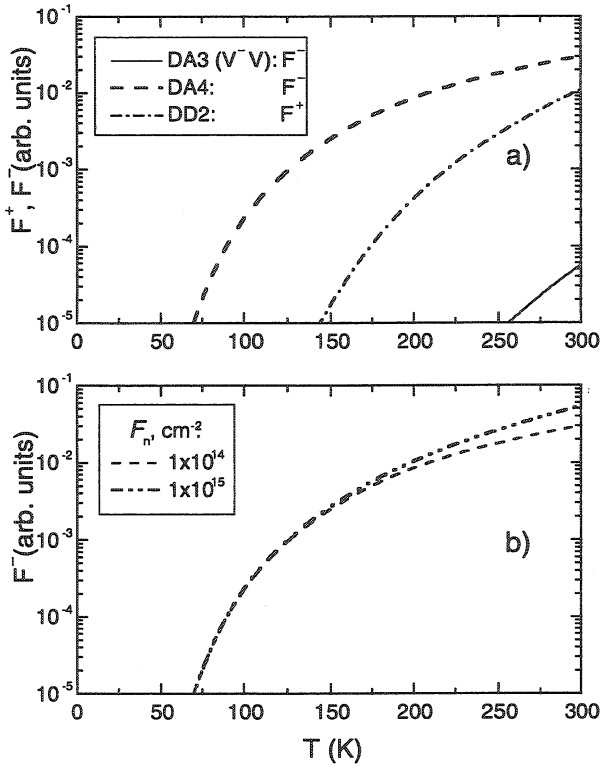

Figure 13: Calculated dependencies on temperature of charged fractions F^+ and F^- for three deep levels of radiation induced defects, DD2, DA3 (VV^-) and DA4 (a), and the temperature dependence of F^- for the deep level DA4 at two different values of 1 MeV neutron fluence (b).

All curves in Figure 13 show gradual decrease of the charged fractions F^+ and F^-. Only for the deep levels located close to the midgap, DD2 and DA4, however, these fractions are appreciable, and the changes of their charged state fractions are significant in the range from 200 down to 130 K. At the same time the deep levels of the VV^- (and also of C_i-O_i complexes) are practically neutral even at room temperature since their charged fractions are lower than 10^{-4}. Therefore their contributions to N_{eff} are $< 10^{10}$ cm^{-3} which is negligible for the total N_{eff}.

Simulation of the Lazarus effect

For the simulation of the Lazarus effect, the temperature dependences of the detector bulk generated current, of the occupancy of deep traps, and of the carrier mobility were used. The corresponding set of equations was solved numerically, assuming that only two of the mid-gap deep levels, i.e. DD2 and DA4, contribute to CCE(T). The concentrations of DD2 and DA4 were used as the main adjustable parameters.

The experimental dependence of the CCE on T for a detector operated at V = 100 V, extracted from [11], and the results of its fit with the parameters listed in Table 4, are presented in Figure 14. The dashed line shows the CCE(T) calculated without the trapping effect, considering only the geometrical factor. The dash-dot line is the result calculated from the full model that includes both geometrical and trapping factors for the charge loss. Quantitative agreement between the experimental data and the fitted curve is observed in the full range of T, with the recovery temperature T_r = 132 K.

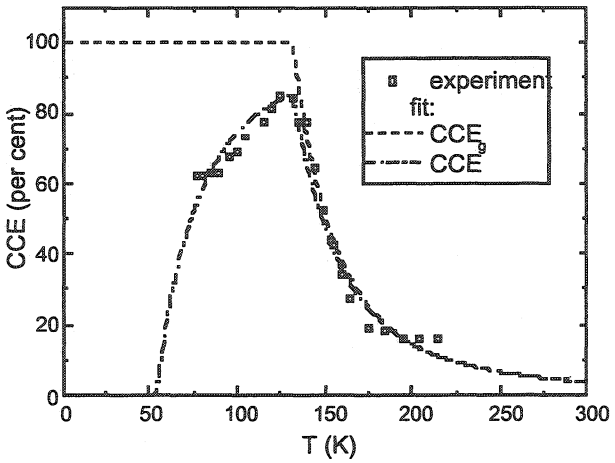

Figure 14: Experimental temperature dependence of the CCE for MIPs in neutron irradiated detector [11], and its fit with the parameters specified in Table 4. $\Phi_n = 1 \cdot 10^{14}$ cm^{-2}, $V = 100$ V.

Note that the energy level of DA4 ($E_c - 0.53$ eV) was only slightly adjusted compared with deep level parameters listed in Table 2 ($E_c - 0.52$ eV).

	DD2		DA4		current		trapping	
	electrons	holes	electrons	holes	electrons	holes	electrons	holes
E_t, eV	$E_v + 0.48$		$E_c - 0.529$		0.65			
σ_e, cm^2	$1 \cdot 10^{-15}$		$1 \cdot 10^{-15}$		$1 \cdot 10^{-13}$		$1 \cdot 10^{-15}$	
σ_h, cm^2		$1 \cdot 10^{-15}$		$1 \cdot 10^{-15}$		$1 \cdot 10^{-13}$		$1 \cdot 10^{-15}$
N, cm^{-3}		$4 \cdot 10^{14}$	$8.0 \cdot 10^{14}$		$2.6 \cdot 10^{14}$		$4 \cdot 10^{14}$	$4 \cdot 10^{14}$

Table 4: Parameters of deep levels derived from the fits of the temperature dependence of CCE. $T_r = 132$ K.

Direct experimental confirmation of the Lazarus effect model

The key point of the model developed here is, that the basic mechanism of the CCE recovery is related with the reduction of N_{eff} due to the cooling of the detector, entailing $F_g = 1$ and $w = d$ at $T = T_r$. To confirm this concept, transient current measurements of the detector irradiated by neutrons were performed. The transient current pulses were measured after nonequilibrium carrier injection by laser light pulses through the n^+-contact, at different temperatures. The transient current pulse shapes are shown in Figure 15. According to the relationship between the shape of the current pulse response and the electric field profile in the detector SCR [14], at $T = 297$ K the decay of the current pulse response corresponds to the maximum electric field at the n^+-contact. This fact indicates that N_{eff} has negative sign. As the detector is cooled down to 200 K, the current pulse decay reveals the same negative sign, but its shape is close to what is characteristic of a detector close to full depletion, which is due to the reduction of $|N_{eff}|$. At $T \approx 140$ K, which is close to T_r, the current pulse top becomes flat, indicating that $|N_{eff}| \approx 0$. This fact is a direct verification of the model developed above.

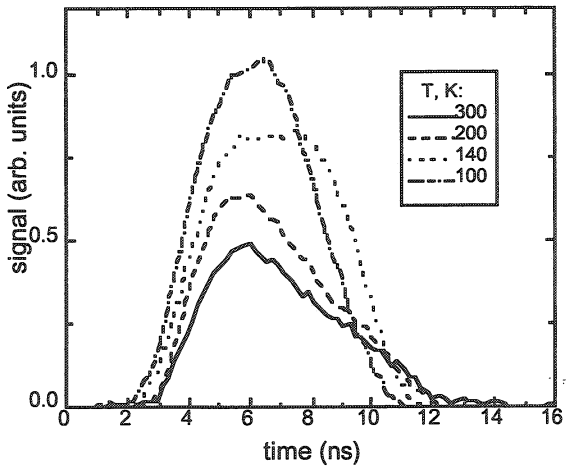

Figure 15: Transient current pulse response of neutron irradiated detector at different temperatures. $\Phi_n = 1.1 \cdot 10^{14}$ cm^{-2}; V = 100 V.

The model and its direct proof by the TCT data above lead to the following conclusions, which have been discussed in greater detail in a forthcoming publication [15]:

- The main physical reason for the Lazarus effect is the reduction of $|N_{eff}|$ with decreasing temperature.
- The detector stays partially depleted at $T > T_r$, and becomes fully depleted at $T \leq T_r$. For the investigated detector irradiated by $\Phi_n = 1 \cdot 10^{14}$ cm^{-2} and operated at 100 V this transformation occurs at $T_r = 132$ K.
- The peak in the non-monotonic temperature dependence of CCE originates from the competition of the reduction of $|N_{eff}|$ when decreasing the temperature, with the charge loss increase due to carrier trapping, which dominates below T_r.
- The deep midgap energy levels, which are responsible for the Lazarus effect, are an acceptor type trap $E_c - 0.52$ eV and a donor type trap $E_v + 0.48$ eV.
- The V-V$^-$ and C_i-O_i complexes, which are usually considered as the main radiation-induced defects with deep levels in irradiated silicon, are not responsible for changes in N_{eff} below room temperature.

2.4 Polarization of Silicon Detectors by Minimum Ionizing Particles

The degradation of Si detectors under irradiation is mainly due to the creation of high concentration of defects in the detector material. This leads to the increase of the reverse current and of the full depletion voltage V_{fd}, and to the reduction of the charge collection efficiency CCE. In these cases the values are steady state parameters determined by the thermal equilibrium conditions in the detector bulk, regarding the value of the bulk generation current and occupancy of deep levels.

Another aspect in the operation of an irradiated detector is the transient of the abovementioned parameters, when increasing the intensity of the ionizing particles suddenly. This can lead to changes in the deep level occupancy and to the corresponding changes in the electric field distribution and CCE. The effect can be magnified by the detector cooling, due to the increase of trapping probability for DL.

The physical model of the detector signal degradation at low temperatures due to radiation-caused changes in the electric field distribution, also referred to as the "detector polarization", was proposed in [16] for germanium detectors and was later experimentally observed in Si detectors [7], [17]. The detector polarization results from the detector passing from the full depletion to the partial depletion mode, accompanied by the formation of high-resistivity electrically neutral base region, and by drastic reduction of the CCE.

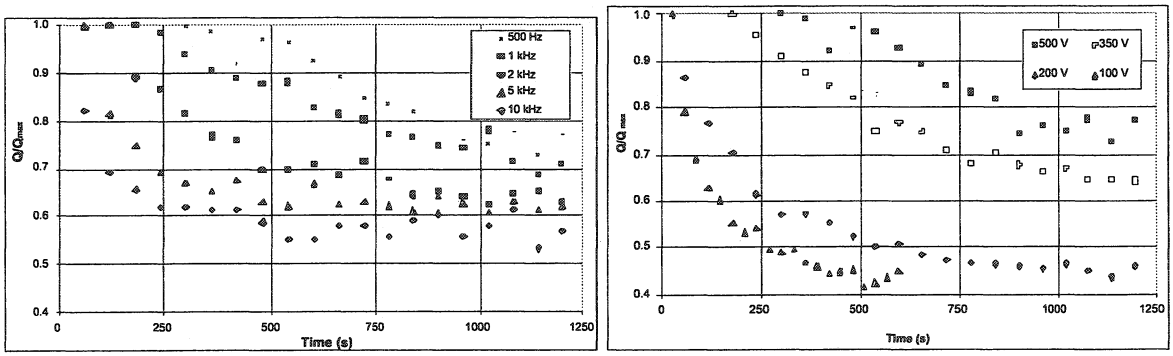

Figure 16: Left: The normalized collected charge versus time measured at 87 K, and at different repetition rates of the 1030 nm laser light pulses incident on the p^+ contact of the detector, while applying 500 V reverse bias. Right: The normalized collected charge versus time measured at 87 K and different voltages with the 1030 nm laser light (pulse repetition rate = 500 Hz) on the detector.

Figure 16 (left) presents a set of charge collected at a constant bias voltage and temperature normalized to their maximum value (Q/Q_{max}) versus time for different *IR*-laser pulse frequencies. The curves measured at low repetition rates contain a flat part in the beginning. This delay before the CCE drop is called "operational time" t_{op}. A similar set of time evolution measurements of Q/Q_{max} were performed at a constant frequency, with different values of reverse bias V (see Figure 16 right). There is a similar flat region of Q/Q_{max} in the beginning, showing that the operational time t_{op} increases with the bias.

The experimental data were explained in the framework of a model involving a high concentration of deep levels, acting as trapping centers for free carriers. Initially, just after applying the bias ($t = 0^+$), N_{eff} (0^+) is small and $E(x)$ is uniformly distributed in the detector bulk. Under these conditions, the current injected by *IR*-laser light is significantly higher than the bulk generation current, and can provide free carriers for filling the deep level traps. The concentration of trapped carriers n_t at time t is determined by the rate equation:

$$\frac{dn_t}{dt} = \sigma v_{th} n(N_t - n_t) - \frac{n_t}{\tau_d}, \qquad (15)$$

where σ is the capture cross section, N_t is the total concentration of the traps, n is the average concentration of free carriers (either electrons or holes) in the detector space charge region, v_{th} is the thermal velocity, and τ_t, and τ_d are the trapping and de-trapping time constants.

The analytical solution of Eq. (15) is:

$$n_t(t) = \frac{n\sigma v_{th} N_t}{n\sigma v_{th} + \frac{1}{\tau_d}}\left(1 - e^{-\frac{t}{\tau_p}}\right) = n\frac{\tau_p}{\tau_t}(1 - e^{-\frac{t}{\tau_p}})$$
$$\tau_p = \frac{1}{n\sigma v_{th} + \frac{1}{\tau_d}}, \tag{16}$$

where τ_p is defined as the polarization time constant.

Consequently:

$$N_{eff}(t) = N_{eff}(0) \pm n_t(t) \quad , \tag{17}$$

with the + sign for hole trapping and – sign for electron trapping. The trapping causes the time evolution of the electric field distribution as shown in Figure 17 for electron trapping. At a given bias V, the collected charge stays constant as long as the absolute value of N_{eff} is small enough to keep up the electric field in the entire volume. $N_{eff} = |N_{eff}^*|$ corresponds to the detector depletion point. When $|N_{eff}| > |N_{eff}^*|$, W becomes smaller than d and the electrical neutral base appears. In this case the collected charge will decrease since it is proportional to the square of geometrical factor $(W/d)^2$ [13]. Hence, the condition for collected charge degradation is:

$$|N_{eff}(t)| > \frac{2\varepsilon\varepsilon_0 V}{ed^2} \equiv |N_{eff}^*|. \tag{18}$$

Consequently, the period during which the detector will operate in fully depleted mode can be defined as the period from $t = 0$ when $N_{eff} = N_{eff}(0)$, to the time when $|N_{eff}| = |N_{eff}^*|$.

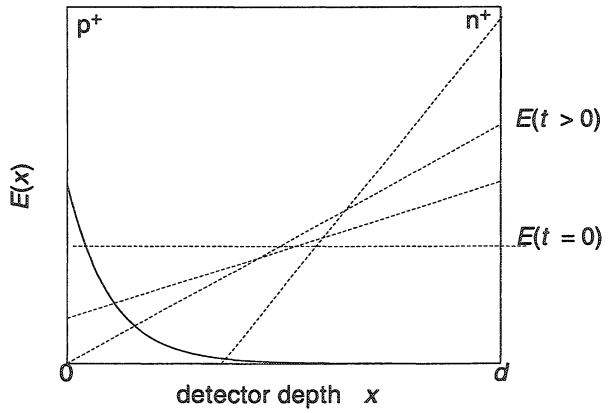

Figure 17: Potential distribution schematic (dashed lines) in the non-depleted detector and light-injected e–h pair distribution for light illumination on the p^+ and n^+ contacts (solid lines) at RT.

Eqs. (16), (17) together with Eq. (18) define the detector operation time limit t_{op} in terms of detector operation and trapping parameters:

$$t_{op} = -\tau_p \ln\left[1 - \frac{\tau_t}{\tau_p}\frac{|N_{eff}^* - N_{eff}(0)|}{n}\right]. \tag{19}$$

The value $|N_{eff}^* - N_{eff}(0)|$ is the range of the variation of N_{eff} due to trapping, and both $N_{eff}(0)$ and N_{eff}^* can assume signs.

The above model is based on the assumptions that 1) only one type of free carriers, due to the injected current, is trapped; and 2) the free carriers are uniformly distributed in the SCR. In practice the MIP particles and *IR*-laser create a non-uniform carrier distribution

$$\begin{cases} n = \dfrac{G_n(x)}{v_n} & \text{for electrons} \\ n = \dfrac{G_p(d-x)}{v_p} & \text{for holes} \end{cases} \tag{20}$$

where $v_{n,p}$ are the carrier drift velocities, and $G_{n,p}$ are the free carrier generation rates, for electrons and holes, respectively.

To determine whether only one carrier type is responsible for the detector polarization under MIPs, or whether both of them contribute to the trapped charge, the electric field distribution in the detectors after their polarization was investigated by the transient current technique using red laser light with 15 μm penetration depth.

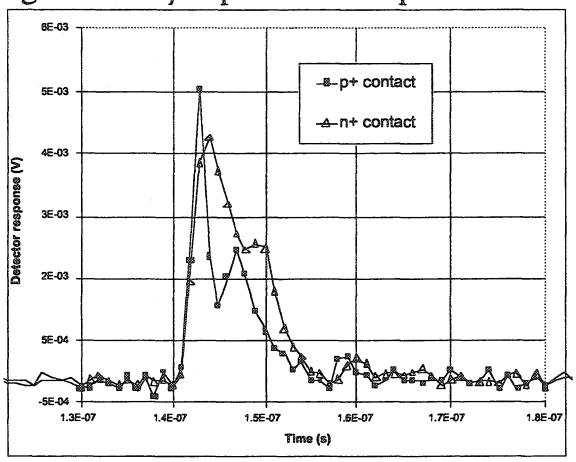

Figure 18: Current responses for the 670 nm laser, measured after polarization, for the laser light illuminating the p^+ and n^+ contacts.

Figure 18 shows the current responses for the red laser, measured after polarization, for the laser light illumination on the p^+ and n^+ contacts. In both cases the response has two peaks, which indicates the double-peak electric field distribution. The amplitude of the first peak is higher, while the second peak is smoother and has a tail. This feature indicates that between the two regions with higher electric field, a layer with significantly lower field exists, as illustrated in Figure 19.

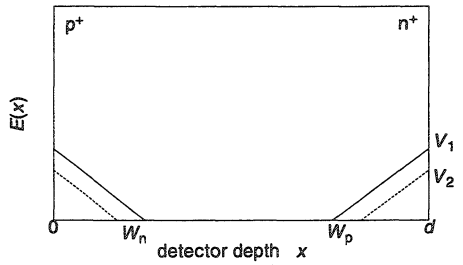

Figure 19: The electric field distribution schematic for a) a permanently biased (V_1) detector after polarization and freezing (solid line) and b) the changes due to sharp bias reduction from V_1 to V_2 (dashed line).

Hence the above model of polarization, with the trapping of a single type of carrier, does not represent the reality, and the quantitative model should consider the true trapping of both types of carriers. The double-peak field distribution indicates that the collected charge degradation happens at lower voltages and disappears. In this case the criteria for detector polarization is a pinch-off elimination between the SCR's propagating from the two contacts. For symmetrical electric field distribution $W_p = W_n = \frac{d}{2}$, and the critical N^*_{eff} can be calculated from

$$\left|N^{*\odot}_{eff}\right| = \frac{2\varepsilon\varepsilon_0 \frac{V}{2}}{e\left(\frac{d}{2}\right)^2} = \frac{4\varepsilon\varepsilon_0 V}{ed^2} \tag{21}$$

where $V/2$ is the potential applied to each field region of the detector, and the operational time limit t_{op} defined from Eq. (19) can now be modified by using the new value of N^*_{eff} of $\frac{4\varepsilon\varepsilon_0 V}{ed^2}$.

To fit the experimental data for t_{op} (see Figure 16 left) the same concentration and capture cross section of trapping centers have been chosen for electrons and holes. The activation energy for the electron trap at E_c – 0.45 eV (corresponding to the VV^- related defects) and for the hole traps E_v + 0.35 eV (C_i-O_i center), and the identical capture cross sections $\sigma_n = \sigma_p$ = $2\text{x}10^{-15}$ cm^2 were considered.

The fitting results on t_{op} are shown in Figure 20. The experimental data are fitted well in the range of more than one order of magnitude of t_{op}. The N_t obtained from this fit is $2\cdot10^{15}$ cm^{-3}.

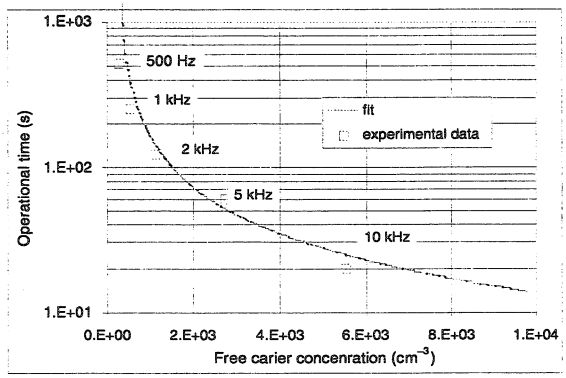

Figure 20: Operational time as a function of free carrier concentration in the space charge region calculated using N^*_{eff} from Eq. (21). The solid line is the corresponding fit.

These results show that the operation of irradiated Si detectors at cryogenic temperatures can be affected by the polarization of the detector. A current density of $5\cdot10^{-10}$ A/cm^2 is sufficient to cause this polarization effect. This current corresponds to the MIP counting rate of about 10^5 MIP/s/cm^2 (each MIP generates $2\cdot10^4$ e-h pairs), which is close to the prediction of the particle flux in the trackers of future high-luminosity colliders.

There are two obvious ways to eliminate the polarization effect: by optimizing the operating temperature to keep the value of the detector bulk generation current at a value equal to or higher than that generated by the incident radiation, or by injecting free carriers to the detector bulk using light or through p-n junctions. The current will flatten and stabilize the electric field

distribution, as will be discussed in the next subsection. The current injection techniques are proposed to be developed in the future RD39 program.

2.5 Approach for Electric Field Manipulation by Free Carrier Injection

After irradiation of Si detectors by neutrons beyond a fluence Φ_i, corresponding to space charge sign inversion (SCSI), the initial space charge concentration N_{eff0} is negative, and therefore the maximum electric field E_m is near the n^+-contact. The method of electric field manipulation, which allows to reduce the N_{eff} in irradiated detectors, is based on the reduction of the negative N_{eff} by holes injected via the n^+-contact. At low temperatures the injected holes will be captured by radiation-induced defects in the SCR, leading to an accumulation of positive space charge and to a corresponding reduction of the absolute value $|N_{eff}|$ of N_{eff} from its initial value $|N_{eff0}|$. Clearly, the electric field profile will change accordingly. At some specific level of carrier injection it becomes almost uniform, as $|N_{eff}|$ decreases from $|N_{eff0}|$ to zero, resulting in a corresponding reduction of V_{fd}. Consequently the CCE will reach its maximal value at lower voltage at which the detector will be fully depleted.

This idea, experimentally proved earlier in [13], was analytically studied to determine the optimal conditions for its practical realization. For that the rate equation

$$\frac{dp_t}{dt} = -\frac{p}{\tau_t} + \frac{p_t}{\tau_d}, \tag{22}$$

together with the Poisson equation

$$\frac{dE}{dx} = \frac{q_o}{\varepsilon\varepsilon_o}\left(p_t + N_{eff0}\right) \tag{23}$$

were solved. In Eqs. (22) and (23) p is the concentration of the injected free holes, p_t is the concentration of holes captured by deep energy levels with a concentration N_t, q_0 is the value of the elementary charge and ε and ε_0 are the permittivities of silicon and vacuum, respectively. For simplicity it was assumed that the occupation of deep levels is controlled by hole transitions between a deep level and the valence band.

The calculations of the electric field distribution were carried out for detectors irradiated by a neutron fluence Φ_n in the range $1\cdot10^{14}$ cm^{-2} to $5\cdot10^{15}$ cm^{-2}. For a comparison with the experimental data, most results were obtained for the conditions corresponding to those in the CCE measurements in [13]: $\Phi_n = 1.4\cdot10^{14}$ cm^{-2} and an operational bias of V = 210 V. The injected hole current density was in the range of 100 pA/cm^2 to 20 nA/cm^2. It was assumed that the injected holes were captured by radiation-induced C_i-O_i defect complexes, which act as hole traps with the parameters $E_t = E_v + 0.37$ eV; $\sigma_h = 3\cdot10^{-15}$ cm^2 [18], [5]. The concentration of the C_i-O_i deep levels is $N_t = \beta\Phi_n$, with the introduction rate β = 1.05 cm^{-1} [18] for neutron irradiation. The space charge concentration after irradiation was evaluated from the values of Φ_n according to Eq. (12) in [11], and was $N_{eff0} = -1.05\cdot10^{13}$ cm^{-3} at $\Phi_n = 1.4\cdot10^{14}$ cm^{-2}.

The calculated dependence of the electric field distribution on the injected hole current density at T = 140 K, in a detector irradiated by $\Phi_n = 1.4\cdot10^{14}$ cm^{-2}, is presented in Figure 21. The initial $E(x)$ at $j = 0$ and T = 140 K is a standard linear dependence on x, with a maximum value of $E_o \approx 26$ kV/cm at the n^+-contact due to the negative value of N_{eff0}. The depth W of the SCR under these conditions is about 162 μm, smaller than the geometrical detector thickness d

= 280 μm. Thus the detector biased at V = 210 V is not fully depleted. Injection of a hole current of j = 1 nA/cm^2 modifies the electric field only slightly. At j = 8 nA/cm^2, however, the SCR extends up to the detector p$^+$-contact, i.e. the detector becomes fully depleted. Nevertheless, two regions with a different $E(x)$ profile are evident at this current: a region with a linearly decreasing $E(x)$ starting from the n$^+$-contact, and leveling in a region with a low, practically constant electric field adjacent to the p$^+$-contact. At $j = j_{opt}$ (~16 nA/cm^2) the electric field distribution is close to uniform. We define the criterion for the optimal electric field distribution as $|(E_0 - E(d))/E_0| \leq 10\%$. The calculation for $j > j_{opt}$ shows that excess hole trapping results in an essential modification of the $E(x)$ profile, in which the maximum electric field is shifted to the p$^+$-contact due to the dominating positive space charge.

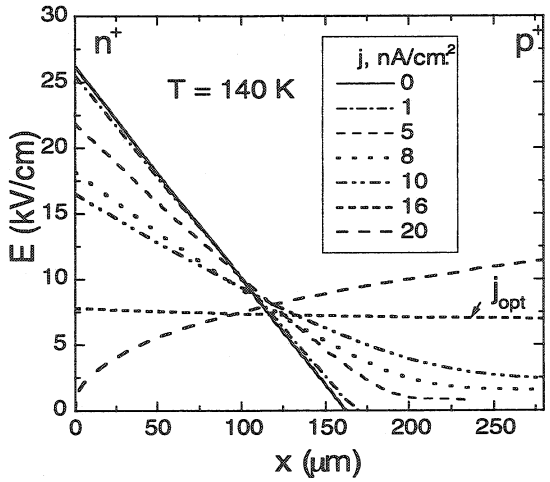

Figure 21: Dependence of the electric field distribution on the hole injection current density in a Si detector irradiated by neutrons. $\Phi_n = 1.4 \cdot 10^{14}$ cm^{-2}; V = 210 V.

The full range of the appropriate injection current (operational range) covers the currents corresponding to the full depletion of the detector. For instance, for the detector considered here (irradiated by $\Phi_n = 1.4 \cdot 10^{14}$ cm^{-2} and operating at T = 140 K), this range is between $j \approx 8$ nA/cm^2, which reduces N_{eff} sufficiently to achieve full depletion under the given bias (210 V), and $j \approx 20$ nA/cm^2, at which the electric field at the n$^+$-contact is close to zero. Significant non-linearity of $E(x)$ is predicted only at the limits of the injected current range. Thus, for a detector irradiated by a fluence of $1.4 \cdot 10^{14}$ cm^{-2}, the range of j from 8 to 16 nA/cm^2 can be considered as optimal for full depletion of a detector operating at T = 140 K.

A similar transformation of the electric field distribution is expected with reduction of the temperature at a constant j within the operational range (Figure 22). It can be seen that, at a constant hole injection current density j = 10 nA/cm^2, the changes of the electric field inside the detector bulk are negligible in the temperature range from 293 K to 150 K. Significant changes of the electric field appear only at T < 145 K. At T = 140 K the electric field region reaches the p$^+$-contact. Finally, the electric field becomes almost uniform at the optimal temperature T_{opt} = 137.8 K for j = 10 nA/cm^2.

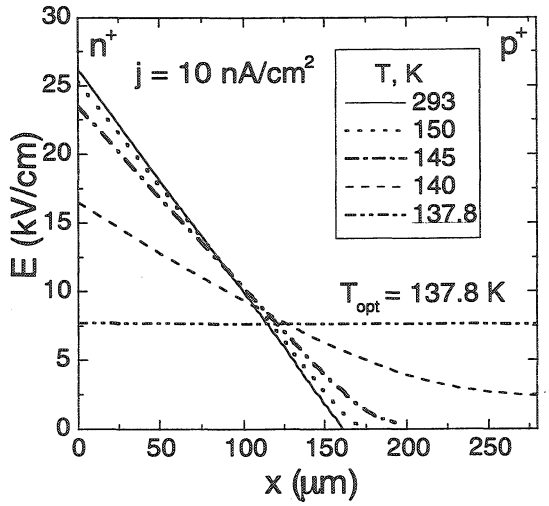

Figure 22: Dependence of the electric field distribution on temperature in a Si detector irradiated by neutrons. $\Phi_n = 1.4 \cdot 10^{14}$ cm^{-2}; $V = 210$ V.

The calculated dependence of the depth W of the space charge region on temperature T ranging from 200 K down to 100 K are presented in Figure 23, with the injected hole current density varying in the interval from 100 pA/cm^2 to 20 nA/cm^2. The SCR depth stays nearly constant (162-165 μm) in the temperature interval from 300 K to 160 K (for j = 20 nA/ cm^2) and to 130 K (j = 0.1 nA/cm^2), depending on the injected current density. A sharp increase of W up to the detector thickness then occurs near T_{fd}, the temperature corresponding to the full depletion of the detector. The range of T_{fd} for different injected hole current densities is shown in Figure 23 above the curves of $W(T)$. Note that T_{fd} is just below T_{opt}. At the same time T_{opt} increases from 120 K to 137 K in the range of j from 0.1 to 5 nA/cm^2 and it tends towards a limiting value, with further increase of injected current density (Figure 24).

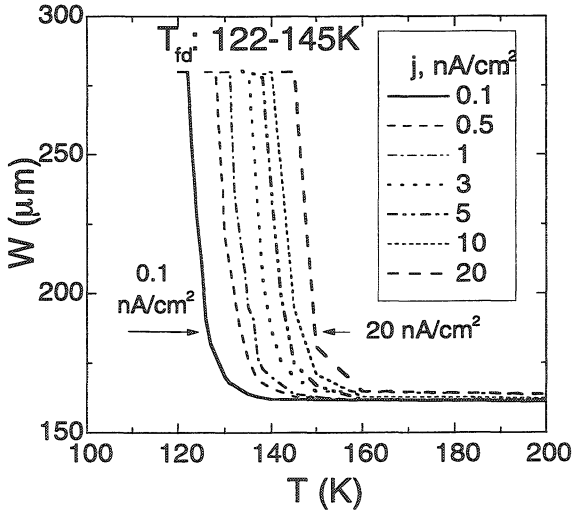

Figure 23: Dependence of space charge region depth on temperature illustrating achievement of detector full depletion at T_{fd} in the temperature interval specified above the curves. W does not vary in the range from 300 K down to 200 K. $\Phi_n = 1.4 \cdot 10^{14}$ cm^{-2}; $V = 210$ V.

The distributions of electric field in detectors irradiated by higher neutron fluences (up to $5 \cdot 10^{15}$ cm^{-2}) operating at low temperatures under hole injection show similar features to that for a detector irradiated by $\Phi_n = 1.4 \cdot 10^{14}$ cm^{-2}. The only difference is that the value of E_o increases

with accumulated neutron fluence up to 10^5 V/cm. Nevertheless, it is worth emphasizing that a uniform electric field can also be achieved by hole injection with practically the same operating conditions ($j_{opt} \leq 20$ nA/cm^2, $T_{opt} \approx 140$ K). The calculated values of N_t, N_{eff0} and T_{opt} versus Φ_n are listed in Table 5. For practical applications, it is important to note that the values T_{opt} and j_{op} have a weak dependence on Φ_n.

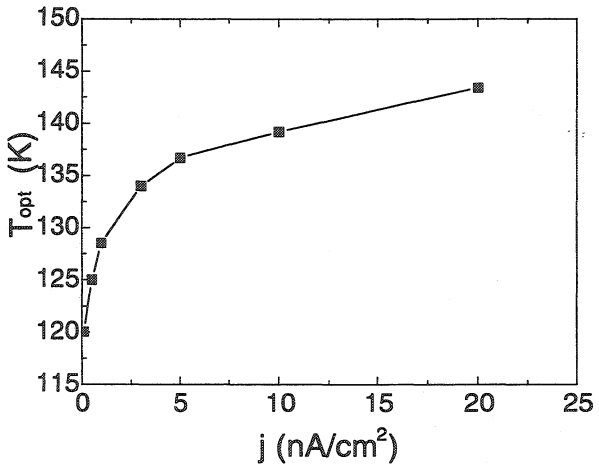

Figure 24: Dependence of T_{opt}, corresponding to a uniform electric field, on the injected hole current density. $\Phi_n = 1.4 \cdot 10^{14}$ cm^{-2}; $V = 210$ V.

These fundamental features show that the approach discussed here, for increasing the operational fluence range of Si detectors, does not require a high stability or precision of either the injected current density or of the detector temperature. Moreover, as the value of the injected current density is not highly critical, the light source covering a large number of sizable silicon detectors can be an array of light emitting diodes. Such simple light sources were already used in [11], and the technique is being considered for the Roman pot microstrip tracker of the TOTEM experiment in the LHC. Larger arrays of detector modules, especially with sensors mounted back-to-back, would clearly require the light sources to be taken into account in the engineering of the support structures and of the front-end readout electronics.

Φ_n (cm^{-2})	N_t (cm^{-3})	N_{eff0} (cm^{-3})	T_{opt} (K)
$1.4 \cdot 10^{14}$	$1.5 \cdot 10^{14}$	$-1.05 \cdot 10^{13}$	143.4
$5 \cdot 10^{14}$	$5.25 \cdot 10^{14}$	$-3.46 \cdot 10^{13}$	141.7
$1 \cdot 10^{15}$	$1.05 \cdot 10^{15}$	$-6.7 \cdot 10^{13}$	141.2
$5 \cdot 10^{15}$	$5.25 \cdot 10^{15}$	$-3.46 \cdot 10^{14}$	140.4

Table 5: Dependence on the neutron fluence, for the concentration N_t of the hole trap C_i-O_i, for N_{eff0}, and for T_{opt}, corresponding to the injected hole current density of 20 nA/cm^2.

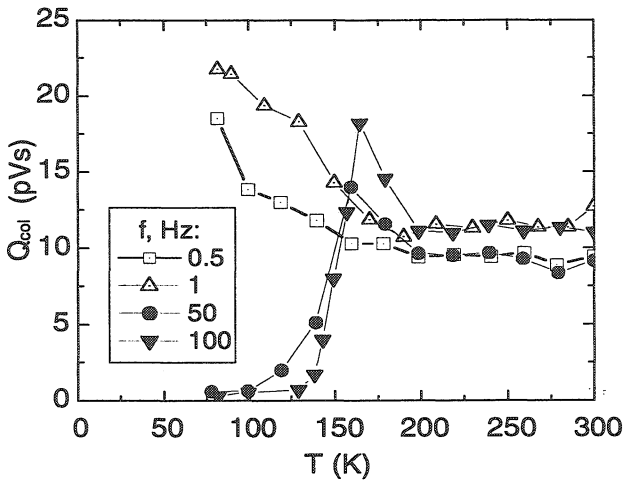

Figure 25: Experimental dependence of CCE on T in a Si detector irradiated by neutrons [13]. Φ_n = $1.4 \cdot 10^{14}$ cm^{-2}; V = 210 V.

Comparison with Experimental Results

The data in Figure 25 represent the dependence of the collected charge on temperature. In that experiment, the hole injection was achieved by illumination of the n$^+$-contact with a pulsed red laser. Variation of the pulse frequency f from 0.5 to 100 Hz enables one to change the injected current density

$$j = q_o n_o f / S_o \tag{24}$$

where n_o is the number of electron-hole pairs generated by a single laser pulse and S_o is the area of the light pulse spot. This variation of f is equivalent to the changes of j in the range 0.1 to 20 nA/cm^2 considered in our calculations.

At high T the injected current is not high enough to affect the filling of deep levels. The geometrical factor W/d which determines the CCE therefore stays constant, resulting in a CCE which is independent of T. A reduction of temperature at a constant j leads to an increase of the CCE, namely at f = 50 Hz and 100 Hz (i.e. j = 10 nA/cm^2 and 20 nA/cm^2, respectively), the maximum CCE (CCE$_{max}$) is achieved at T_m = 155 K and 160 K, respectively, (where T_m corresponds to CCE$_{max}$). This implies that at this temperature N_{eff} has decreased down to the value which allows full depletion of the detector at V = 210 V, i.e. W/d = 1. From the calculated data presented in Figure 23 it follows that at j = 10 — 20 nA/cm^2 the detector becomes fully depleted at temperatures ranging from 145 to 140 K, which agrees within 15 K with the experimental data in Figure 25.

It is important to point out that at the largest values of f, 50 and 100 Hz, the CCE$_{max}$ is observed only in a narrow temperature range around T_m. The reduction of the CCE for $T < T_m$ in the experimental data is correlated with the calculated reduction of the electric field at the n$^+$-contact for $T < T_{opt}$. The drop of E_o to zero near the n$^+$-contact, from which the injection is performed, leads to the loss of the charge carriers that are generated in the region adjacent to this contact. With further temperature reduction, the accumulation of positive charge near the n$^+$-contact results in the expansion of the zero electric field region inside the detector bulk. This effect causes the decrease of CCE down to values close to zero, for carriers generated by red

laser. For MIP radiation, however, in which electron-hole pairs are generated throughout the detector thickness, this sudden decrease of CCE should not occur.

Simulation of the electric field redistribution in the detector bulk leads to the following conclusions:

- The approach of electric field manipulation by nonequilibrium carrier injection is applicable in the neutron fluence range which is important for the applications of Si detectors in experiments at high-luminosity colliders.
- At temperatures in the range of 140 to 145 K, the optimal injection current density for the electric field distribution is 15-20 nA/cm^2. This is much larger than the reverse current and the current corresponding to the standard MIP counting rates (< 10^6 MIP/cm^{2}s). Therefore the electric field and space charge distributions, controlled by carrier injection, will be stable and independent of polarization [11], even at highest MIP counting rates.
- The dependence of the optimal temperature for the electric field distribution in highly irradiated Si detectors shows a tendency to saturate with the injected current. This eliminates the technical problem which could follow from the requirement of a high stability for the current density and for the temperature.
- The predicted weak dependence of the optimal density of the injected current on fluence is beneficial for long-term experiments in high radiation environments, and may eliminate any need for the adjustment of the injected current with time.

References of Section 2

[1] W. Shockley and W. T. Read, Phys. Rev. **87** (1952) 835.

[2] V.N. Abakumov, et al., Sov. Phys. Semicond. **12** (1978), 1.

[3] M. Moll, Ph.D. thesis, University of Hamburg, 1999, DESY-THESIS-1999-040.

[4] V. Eremin et al., Nucl. Instr. and Meth. **A426** (1999) 120.

[5] Z. Li, C. J. Li, V. Eremin and E. Verbitskaya, Nucl. Instr. and Meth. **A388** (1997) 297.

[6] Z. Li and H. W. Kraner, J. Electronic Materials, V.**1**, No.7 (1992) 701.

[7] V. Eremin, Z. Li, I. Iliachenko, Nucl. Instr. Meth., **A360** (1995) 458.

[8] V. Eremin, E. Verbitskaya and Z. Li, Nucl. Instr. and Meth., in press.

[9] E. Fretwurst, V. Eremin, H. Feick, J. Gerhardt, Z. Li and G. Lindström, Nucl. Instr. And Meth. **A 388** (1997) 356.

[10] V. Palmieri, K. Borer, S. Janos, C. Da Viá and L. Casagrande, Nucl. Instr. and Meth. **A413** (1998) 475-478.

[11] K. Borer, S. Janos, V. G. Palmieri, B. Dezillie, Z. Li, P. Collins et al., Nucl. Instr. and Meth. **A440** (2000) 5-16.

[12] H. W. Kraner, Z. Li and E. Fretwurst, Nucl. Instr. and Meth. **A326** (1993) 350-356.

[13] B. Dezillie, Z. Li, V. Eremin, M. Bruzzi, S. Pirollo, S.U. Pandey, and C.J. Li, IEEE Trans. Nucl. Sci., Vol. **46**, No. 3 (1999) 221-227.

[14] V. Eremin, N. Strokan, E. Verbitskaya and Z. Li, Nucl. Instr. and Meth. **A373** (1996) 388-398.

[15] V. Eremin et al., "Temperature dependence of charge collection efficiency in heavily irradiated silicon detectors: the Lazarus effect model", to be submitted to Nucl. Instr. and Meth. A.

[16] V.K. Eremin, N.B. Strokan, and N.I. Tisnek, Sov. Phys. Semicond. **8** (1974) 751.

[17] B. Dezillie, Z. Li, V. Eremin, E. Verbitskaya, Nucl. Instr. and Meth. **A452** (2000) 440.

[18] *3rd RD48 Status Report*, CERN LHCC 2000-009; *LEB Status Report/RD48*, 31 December 1999; *RD39 Status Report* CERN/LHCC 2000-010, 06-Jan-2000.

3 BASIC RESEARCH OF SILICON DETECTORS AT LOW TEMPERATURES

3.1 CCE measurements

The aim of the basic studies is to understand defect formation and macroscopic effects after irradiation at different temperatures, using Charge Collection Efficiency (CCE) and spectroscopic methods such as on-line Electron Paramagnetic Resonance (EPR) and Deep Level Transient Spectroscopy (DLTS).

The precise understanding of the detector behaviour, when operated at different conditions, is mandatory if proper recommendations are to be given to low temperature detector users. The main methods of characterization used are CCE and spectroscopic measurements *in situ*. The latter are presently under evaluation.

The formation of vacancies, V, interstitials, I, and impurity-related defects in silicon after irradiation is temperature and particle dependent. The literature [1] reports that after electron irradiation:

1- V^+ and V^- are observed already at 4.2K
3- V is present in 5 charge states V^{2+}, V^+, V^0, V^-, V^{2-}.
4- the V spectra disappear at:
   ~70 K in n-type low resistivity material,
   ~150 K in p-type material,
   ~200 K in high resistivity material

Moreover, it was observed that at 200 K the divacancy (V_2) and vacancy-oxygen (VO) spectra appear, implying that the vacancy migrates. Migration of V is also possible by ionisation through a so-called *athermal process*.

The single interstitial I has been observed to be mobile already at 4.2K in p-type and at ~140—175 K in n-type silicon.

The detector behaviour at cryogenic temperatures, particularly the CCE, can be explained by the defect behaviour as discussed above. Figure 26 shows the CCE at 80 K of detectors irradiated by the CERN SPS 450 GeV/c proton beam to different fluences at 80 K. All detectors are processed on 4 kΩcm n-type silicon, with the $p^+/n/n^+$ configuration.

On two occasions, after $6 \cdot 10^{14}$ and $1.4 \cdot 10^{15}$ p/cm^2 exposure (equivalent to $3 \cdot 10^{14}$ and $7 \cdot 10^{14}$ n/cm^2 at 1 MeV, respectively), the CCE at different bias voltages was measured after the sample was annealed for a few hours above 200K. The results of the second series of measurements after annealing, performed again at 80 K, are indicated by the pointing arrows.

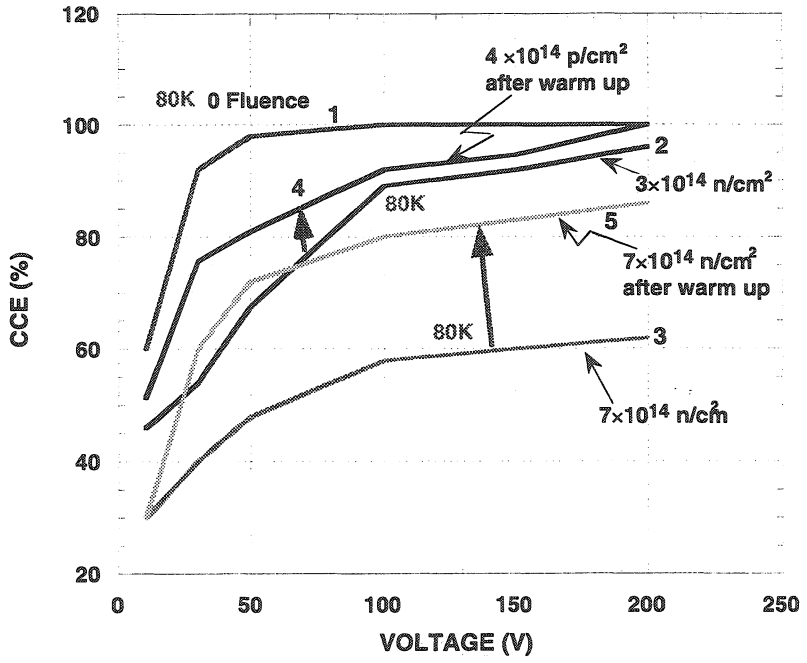

Figure 26: Charge Collection Efficiency at different bias voltages measured after high energy proton exposure at 80 K. The red arrow indicates the difference in charge collection after an equivalent fluence of $6 \cdot 10^{14}$ and $1.4 \cdot 10^{15}$ p/cm^2 after annealing at 200 K. The fluences shown in the figure are normalised to 1 MeV neutrons.

The CCE versus voltage at 80 K is plotted in Figure 26 as curve "1" for reference. Irradiation at 80K leads to a decrease in the CCE and an increase of depletion voltage prior to annealing, as shown in curve "2" for $6 \cdot 10^{14}$ p/cm^2 and curve "3" for $1.4 \cdot 10^{15}$ p/cm^2. Both the CCE and depletion voltage recover partially after annealing at 200K, as shown by curve "4" for $6 \cdot 10^{14}$ and "5" for $1.4 \cdot 10^{15}$ p/cm^2.

This data is consistent with vacancies being immobile at low temperature since they create several defect levels in the forbidden gap. During annealing at 200 K vacancies and interstitials recombine and also divacancies are formed. These effects substantially reduce the number of defects in the bandgap and therefore the CCE and depletion voltage recover.

The Faro group has obtained a substantial amount of data on IV characteristic, CCE and space charge polarisation effects at different temperatures. Preliminary results analysed at Brunel, show that the CCE decreases with two time constants at a fixed bias voltage. An analysis of the fast component shows a linear decrease with irradiation fluence, as shown in Figure 27. This decay in CCE shows very weak temperature dependence in the range between 90 and 180K (Figure 28). These results suggest that polarisation effect is due to trapping of charge created by the radiation of the ^{90}Sr source. Experimental measurements show that the present source, of 10 μCi nominal activity, deposited ~15000 e$^-$/s on the 0.25 cm^2 detector surface. Taking into account X-rays and scattered electrons, the averaged current density should be $> 2 \cdot 10^{-10}$ A/cm^2, which is sufficient to cause a substantial change in N_{eff} during some tens of minutes, if $N_{eff0} \approx 10^{13}$ cm^{-3}. More systematic studies with different source activities are planned to fully understand the nature of the effect, and the analysis of the present data is still underway.

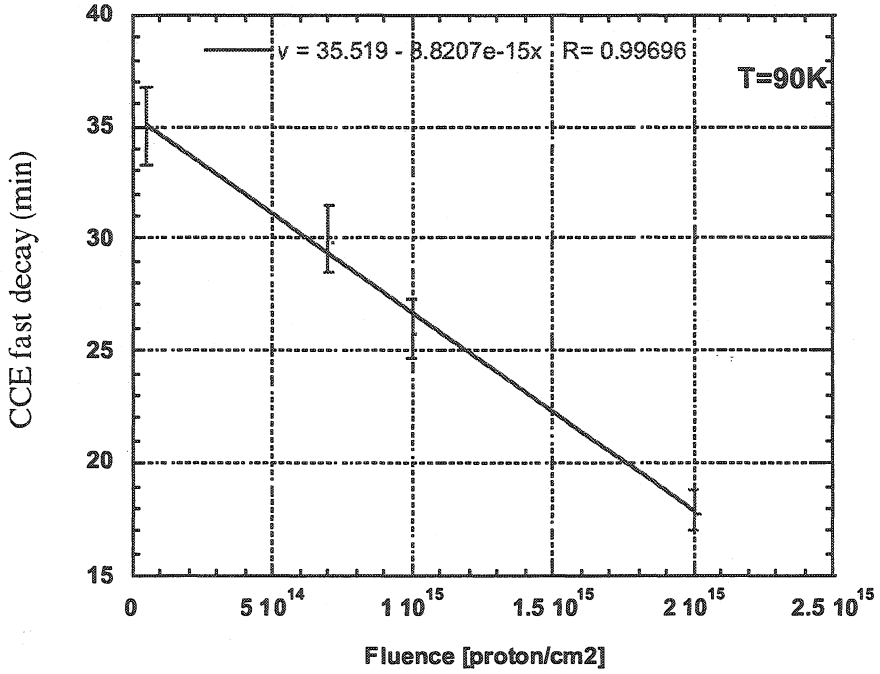

Figure 27: Polarisation fast decay time versus fluence

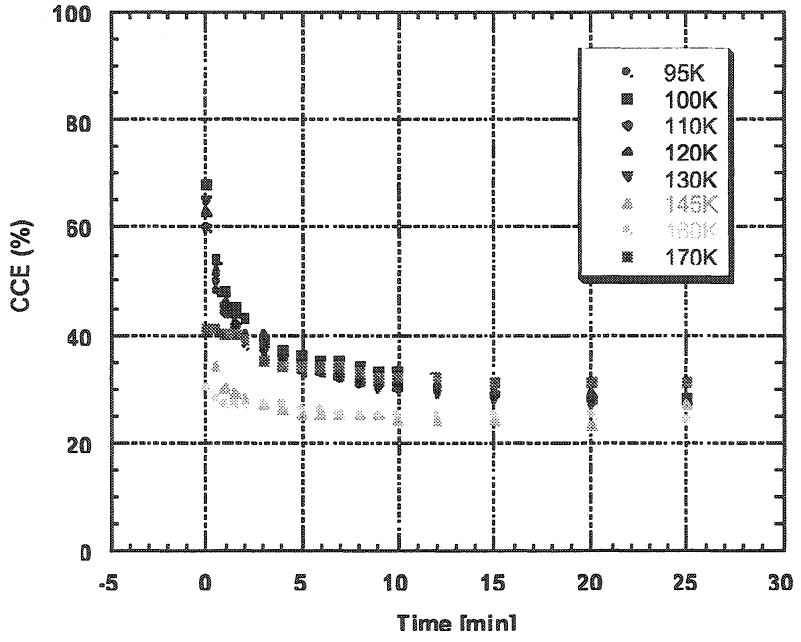

Figure 28: Space Charge polarisation effect versus temperature.

3.2 Lorenz angle measurements in silicon detectors

Future experiments are using silicon detectors in magnetic fields as high as 4 T, the value specified by CMS. In the high radiation environment of the high-luminosity colliders, radiation tolerance of silicon can be improved by cooling to temperatures below 180K, and therefore it is important to understand the influence of the magnetic field on the charge drift under these

conditions. The Lorentz angle θ_L for a magnetic field perpendicular to the electric field is given by

$$\tan\theta_L = \mu_H B = \frac{\Delta x}{d}, \quad (1)$$

where μ_H is the Hall mobility which is independent of the electric field, and the drift length corresponds to the detector thickness d and the shift of the centre of charge is Δx. The Hall mobility is related with the conduction mobility μ by

$$\mu_H = r_H \mu, \quad (2)$$

where the scattering factor of the Hall coefficient r_H describes the influence of the magnetic field on the mean scattering time of carriers of different energy and velocity [2]. As the mobility μ increases with temperature proportional to $T^{-2.42}$ for electrons and $T^{-2.2}$ for holes [3], at low temperatures the deflections of the charge carriers by the Lorentz force increase. Therefore it is important to study the temperature dependence of the Lorentz angle of radiation damaged silicon in high magnetic fields.

The experimental set-up is described in Refs. [4],[5]. Charge carriers are excited on the surface of a double-sided microstrip detector using a short pulse of red laser light. The shift Δx of the charge collected on the opposite side is determined from the signals induced on the strips of that side, as a function of magnetic field. The thickness of the detector is 300 μm. The shift in 4 T field is plotted in Figure 29 as a function of temperature for both charge carriers, for irradiated and unirradiated detectors. The voltage dependence at 4 T field and 77 K temperature is shown in Figure 30. Both behave qualitatively as expected from the Eqs. (1) and (2) at temperatures higher than 160 K, but the Hall scattering factor r_H appears to grow below this temperature.

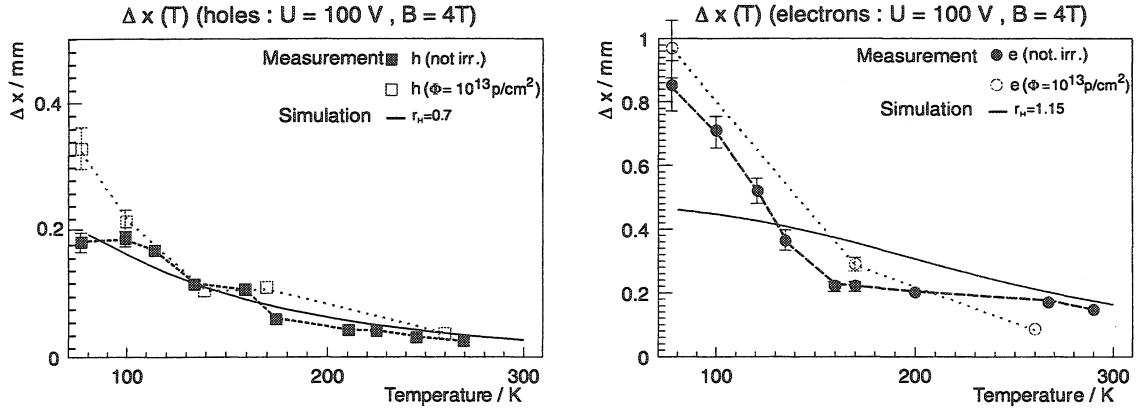

Figure 29: Lorentz shift for electrons (top) and holes (bottom) for 300 μm detector in a 4 T magnetic field as a function of temperature, for an unirradiated detector and a detector irradiated with 21 MeV protons to a fluence of $1.0 \cdot 10^{13}$ p/cm^2. For comparison, the temperature dependence from the Davinci simulation program with a constant Hall scattering factor of 1.15 (0.7) for electrons (holes) is shown by the full lines.

Equations (1) and (2) hold in the region where the drift velocity grows linearly proportional to the electric field. Small deviations may be expected in the high-field region where the drift velocity begins to saturate, and the Hall scattering factor requires detailed calculation. In order to better understand the drift in the detector simulations were performed with the Davinci software package by TMA [7]. The inhomogeneous electric field in the sensor was taken into

account by following the charge in small steps, calculating the mobility at each position and integrating the Lorentz shift using Eq. (1) with a Hall scattering factor of 1.15 and 0.7 for electrons and holes, respectively. These are the values expected for sensors at room temperature, when the scattering by phonons dominates over the scattering by impurities [2]. With the simulated Lorentz shift and its assumed Hall scattering factor $r_{Hall,sim}$ the average Hall scattering factor can then be calculated using the formula:

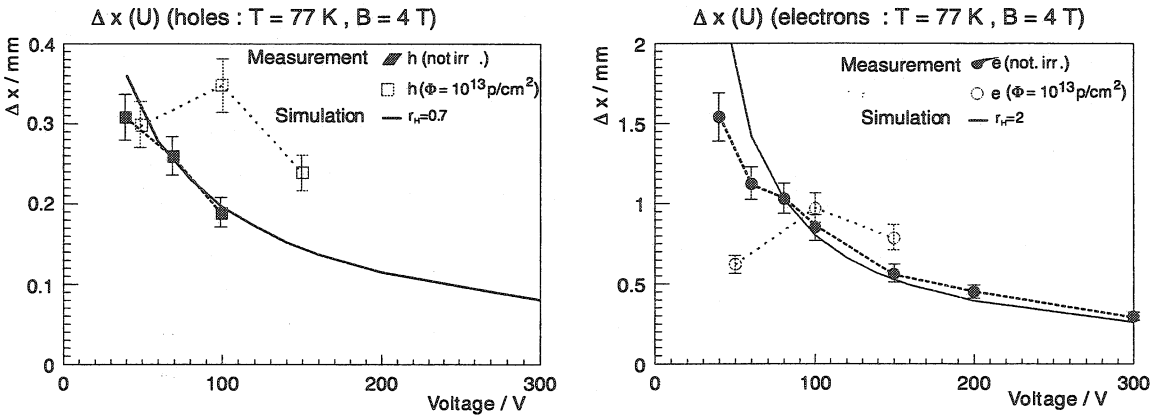

Figure 30: Lorentz shift for a 300 μm detector in a 4 T magnetic field for electrons (top) and holes (bottom) versus bias voltage at a temperature of 77 K, for an unirradiated detector and a detector irradiated with 21 MeV protons to a fluence of of $1.0 \cdot 10^{13}$ p/cm^2. For the latter the full depletion voltage has increased from 40 to 100V. For comparison, the temperature dependence from the Davinci simulation program, with a constant Hall scattering factor of 2.0 (0.7) for electrons (holes), is shown by the full lines.

$$r_{Hall} = \frac{\Delta x_{data}}{\Delta x_{Davinci}} r_{Hall,sim} \tag{3}$$

The shift obtained by using the above simulated scattering factor in a 300 μm thick detector is plotted for a 4 T magnetic field, as a function of temperature and bias voltage, in Figures 29 and 30 together with the data. The scattering factor for the electron Hall coefficient is plotted as a function of temperature in Figure 31.

Figure 31: Preliminary results on the Hall scattering factor of electrons versus temperature calculated from Eq. 2. A rise in r_{Hall} at lower temperatures is expected from Coulomb scattering on t he space charge in depleted detectors [8].

For holes the temperature dependence is well described, but for electrons the Lorentz angle first falls below the simulation for decreasing temperature, as expected for a decreasing value of the Hall scattering factor r_H at lower temperatures [6]. However, below T = 160 K the Lorentz angle for electrons rapidly increases and is a factor two *above* the simulation at liquid nitrogen temperature. The simulation was done with a temperature independent Hall factor of 1.15 (0.7) for electrons (holes), which is certainly wrong [6]. Therefore, the most likely interpretation of the deviation between simulation and data would be the temperature dependence of the Hall scattering factor, since the drift mobility at low temperatures is well known [6] and the electric field dependence is well described by the simulation, as shown in Figure 30. However, then a Hall scattering factor around two is needed. Such a large r_H is expected for Coulomb scattering on impurities [2], [8] like the space charge in a fully depleted detector. This has to be verified with numerical simulations.

Before irradiation the detector depletes fully at room temperature with a bias voltage of 40 V, while after radiation with $1.0 \cdot 10^{13}$ p/cm^2 21 MeV protons per cm^2 the depletion voltage has increased to 100 V. This implies that the bulk is inverted from n-type to p-type material, as expected [9]. The bulk damage of 21 MeV protons is about 2.8 times the damage by 1 MeV neutrons. The decrease of the Lorentz shift for the irradiated sample below 100 V in Figure 30 is due to the reduced effective thickness of the partially depleted detector. When reducing the temperature at 100 V bias, the irradiated detector is likely to run in an overdepleted mode.

In summary, the Lorentz angle was measured for electrons and holes separately in magnetic fields up to 8 Tesla. At the 4 T magnetic field of CMS, the Lorentz angle in a 300 μm thick detector, at 130 K temperature and 100 V bias, is typically 56° for electrons and 27° for holes. Stronger overdepletion leads to a reduced Lorentz angle for both carriers.

After irradiation with protons to a fluence of 10^{13} cm^{-2}, which equals $2.8 \cdot 10^{13}$ cm^{-2} neutron fluence, the Lorentz angle for holes is hardly changed at 130 K temperature if the bias is kept at 100 V. However, for electrons the angle increases to 63°. When increasing the bias voltage, the Lorentz angle is reduced under these conditions, both for holes and for electrons.

3.3 Photo Induced Current Transient Spectroscopy of Extended Defects

It is well known that during irradiation in the LHC environment, a large fraction of the damage will come from fast neutrons, which produce large displacement cascades across extended regions of the semiconductor: the thermally activated rearrangement of the lattice defects should result in both isolated point defects as well as defects clusters. Defect clusters are a major cause in the degradation of the electrical performance of silicon detectors. For this reason, our collaboration has started in this year a detailed study of the contribution of defect clusters on the radiation damage of silicon detectors. In particular, we are interested in understanding the contribution of defect clusters to trapping and recombination processes which can affect the charge collection efficiency at cryogenic temperatures. To study the presence of defect clusters in irradiated Si the PICTS (Photo Induced Current Transient Spectroscopy) technique [11], also called I-DLTS (Current-Deep Level Transient Spectroscopy) [12] has been used by us. Our experimental procedure has followed a method to identify cluster emission in DLTS spectra which has been recently assessed [13]. This method prescribes to acquire several DLTS spectra while changing the duration of the filling pulse, and

to check for spectral shape modifications, which may be related to coulomb barrier formation at clusters. An abnormal broadening of PICTS peaks, which cannot be fitted by means of few point defects, should be interpreted in this procedure as the signature of a defect cluster.

In order to investigate cluster formation after neutron irradiation, we studied by PICTS a set of $p^+/n/n^+$ diodes (with a nominal resistivity ρ = 400–500 Ωcm) irradiated with fast neutrons in the fluence range $\Phi = 2 \cdot 10^{13}$ - $2.3 \cdot 10^{15}$ n/cm^2 (1 MeV equivalent). The measurements were carried out after two years of annealing at room temperature, in the temperature range 30-350K. The sample excitation is provided by a Light Emitting Diode (LED) with wavelength λ=940 nm. The LED is driven by a pulse generator, which allows one to vary the excitation pulse duration t_p [14]. The sampling times are t_1=100 μs and t_2=450 μs. The general shapes of the measured spectra are shown in Figure 32.

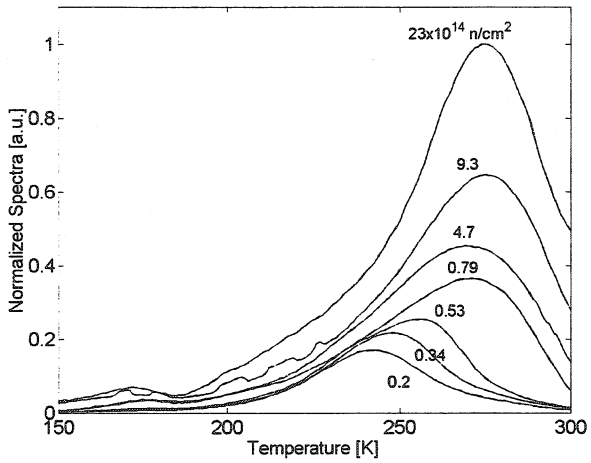

Figure 32: Normalized PICTS spectra obtained with various samples. The irradiation fluence (expressed as $\Phi/10^{14}$ n/cm^2), is reported close to each curve. The filling time is t_p=50 μs.

A very distorted peak, which broadens as the irradiation becomes stronger, can be observed between 200 K and 300 K. This peak is commonly observed in neutron-irradiated silicon, and cannot be fitted using few isolated deep levels: a quasi-continuous distribution of deep levels may be suitable to explain it [14], [15]. Apart from energy spreading, these peak can be related to divacancy related defects (perhaps V_2O, V_3). The level spreading may be due to the energy splitting of identical close defects, interacting inside clusters. The correlation of this broad peak with defect clusters is also suggested by the strong change of the spectral shape observed by varying the filling pulse duration and by increasing the neutron fluence.

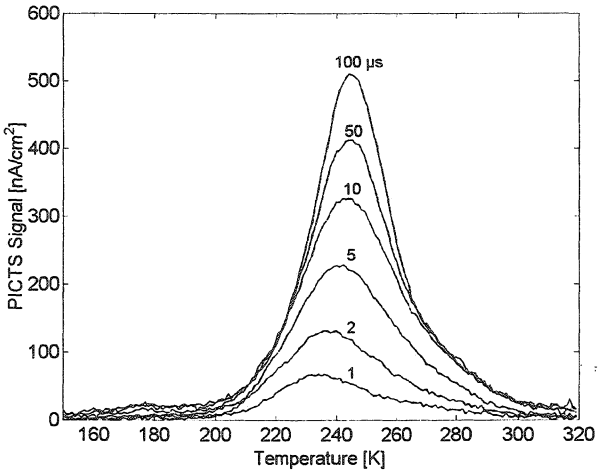

Figure 33: PICTS spectra of the sample irradiated up to $\Phi = 2 \cdot 10^{13}$ n/cm^2. The filling times, expressed in µs, are reported close to each curve.

As an example, Figure 33 shows the PICTS spectra measured with a sample irradiated up to $\Phi = 2 \cdot 10^{13}$ n/cm^2. The line shape is strongly asymmetric, and presents a high temperature shoulder between 260 K and 300 K. The amplitude of the shoulder saturates if $t_p > 10$ µs, while the main component saturates when $t_p > 100$ µs. The peak position shifts slightly toward higher temperatures as the t_p is increased. Conversely, the sample irradiated up to $\Phi = 7.9 \cdot 10^{13}$ n/cm^2 exhibits very different line-shape modifications, as shown in Figure 34. The peak broadens toward lower temperatures as t_p is increased, while the low-temperature sides of the peaks remain almost parallel. All these features cannot be accounted for by means of the contribution of point defects alone, they should indicate the formation and evolution of extended defect regions in the silicon lattice.

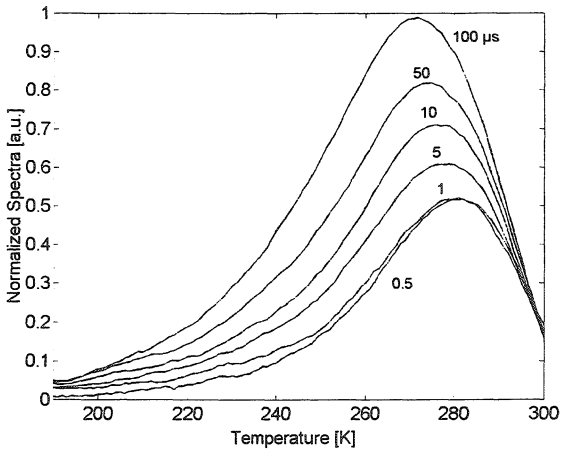

Figure 34: Normalized PICTS spectra of the sample irradiated up to $\Phi = 7.9 \cdot 10^{13}$ n/cm^2. The filling times, expressed in µs, are reported close to each curve. The signals have been normalized by multiplying each one by an arbitrary constant, to put in evidence spectra shape modifications.

The PICTS analysis allowed us to detect which spectral components could be related to defect clusters in irradiated silicon. It appears from our work that the contribution of defect clusters to trapping and recombination processes should be relevant mostly at 150 – 300 K, a temperature range higher than the working temperatures of cryogenic tracking detectors. Nonetheless, more PICTS studies are needed to confirm these results.

References for Section 3

[1] Mat. Sci. in Sem. Proc. 3 (2000) 227

[2] R.A. Smith, *Semiconductors*, Cambridge Univ. Press, 1968

[3] S. Sze, *Physics of Semiconductor devices*, John Wiley and Sons, 1981.

[4] W. de Boer et al., to be publ. in Proc. of ICHEP2000, Osaka, Aug. 2000, arXive:physics/0007059.

[5] F. Röderer, Diplomarbeit, Univ. of Karlsruhe, IEKP--KA/98--24; S. Heising, Ph. D. thesis. Univ. of Karlsruhe, IEKP--KA/99--26; F. Hauler, Ph. D. thesis. Univ. of Karlsruhe, IEKP--KA/99--26.

[6] Landolt-Börnstein, *Numerical Data and Functional Relationships in Science and Technology*, Group III, Band 17a, Springer Verlag, Berlin, 1982.

[7] Technology Modelling Associates, Inc.: Davinci, Version 4.1, July 1998.

[8] E. Ohta and M. Sakata, Jap. Journal of Appl. Phys. **17-10** (1978) 1795.

[9] RD48 Collaboration, http://rd48.web.cern.ch, ROSE/TN/2000-03.

[10] RD39 Collaboration, Nucl. Instr. and Meth. in Phys. Res. A **440** (2000) 5-16 and http://rd39.web.cern.ch, RD39 Status Report CERN/LHCC 2000-010, 06-Jan-2000.

[11] P.Blood and J.W.Orton, *The electrical characterization of semiconductor: majority carriers and electron states*, N.H.March, *Ed. Academic Press*, London, 1992.

[12] V. Eremin et al., Nucl. Instrum. and Meth. **A 426** (1999) 120.

[13] W. Schröter, J. Kronewitz, U. Gnauert, M. Seibt, Phys. Rev. **B 52** (1995) 13726.

[14] D. Menichelli, S. Pirollo, Z. Li, IEEE Trans. Nucl. Sci. **47** (2000) 446

[15] D. Menichelli and M.Bruzzi, Nucl. Instr. and Meth. **A**, in press.

4 BEAMSCOPES FOR NA60

The NA60 Experiment [1] will study dimuon and charm production in proton and heavy ion induced collisions at the CERN-SPS. During the feasibility study of the charm measurement, it became clear that a detector was needed to be placed in the beam axis, before the target, to directly measure the transverse coordinate of the projectiles. The requirements on this detector were quite demanding:

- position resolution of the order of 20 μm;
- high-rate capability, in order to cope with high beam intensities ($10^7 \div 10^9$ particles/s);
- high radiation hardness.

Since no beam detector existed which would fulfill all the above listed requirements, we started a common project between RD39 and NA60 to develop a novel beam hodoscope, hereafter named "beamscope", based on silicon microstrip detectors operated at 130 K.

As a first step, we developed a prototype beamscope for heavy ions. In this case, the combination of the detector hardness provided by the Lazarus effect and the large signals available from the highly ionizing ions ensured a reasonable signal to noise ratio even after high doses. The detector concept was demonstrated in a short run in 1999 with Pb ions, and the preliminary results were presented in the previous RD39 status report [2]. In the next section, we will give a brief description of the detector and present results collected in a longer test performed in November 2000, again with high-intensity Pb beam. The results clearly show that the detector can be reliably operated up to a fluence of ~5×10^{14} ions/cm^2.

After the encouraging results obtained with heavy ions, we started the development of a beamscope for protons, which became possible thanks to the development of a new readout chip carried out in the CERN-Microelectronics group. This chip, manufactured in 0.25 μm CMOS technology, has been designed to profit of operation at 130 K. Placed very close to the detector, it provides a fast amplification stage which allows detecting with good efficiency the proton signal down to 10% charge collection efficiency. In Section 4.3 we describe the main differences between the proton and the heavy ion versions of the beamscope, and present preliminary results obtained during the NA60 commissioning run of fall 2001 with proton beam.

4.1 Beamscope for heavy ions

Figure 35 shows the prototype beamscope as installed in the NA60 beam line. Inside the vacuum chamber, there are two tracking stations (see Figure 36), each consisting of a printed circuit board with two silicon microstrip detectors mounted back to back, with the strips perpendicular to each other. The chamber is closed by a top flange, which contains apertures for the detector modules, the liquid nitrogen transfer line, and instrumentation connections.

Liquid nitrogen flows from a transport dewar vessel through a low-loss transfer line, and feeds capillary pipes soldered on the detector module. The temperature of the detectors can be adjusted between 80 K and 300 K by varying the nitrogen flow in the pipes and the power dissipated through a heater placed on the PCB. The 400 μm thick Al/p+/n/n+/Al silicon detector (produced at BNL) has 24 "narrow" strips of 50 μm pitch, plus 4 "wide" strips of 500 μm pitch on each side, surrounded by a single guard-ring. Simple DC coupling design

could be used, requiring only 3 production masks, thus leading to a significant reduction of the detector processing cost.

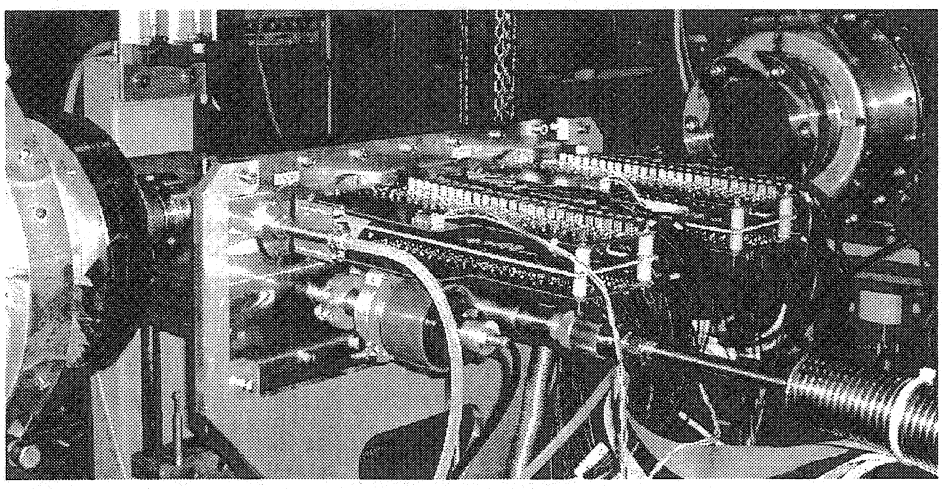

Figure 35: The prototype heavy ion beamscope as installed in the NA60 beam line.

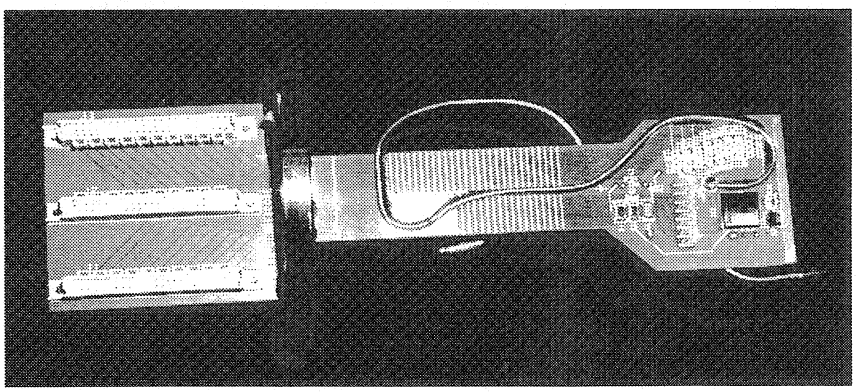

Figure 36: Photograph of the heavy ion beamscope module. The Cu-Ni capillary cooling pipe has an inner diameter of 1 mm.

The wide strips are connected to current-to-frequency converters located outside of the cryostat. The signals integrated over the entire beam spill give a measurement proportional to the number of ions that traversed each strip. With this information, fast beam steering was possible over an area larger than the one covered by the narrow strips, by using a much simpler readout scheme.

The narrow strips are connected to fast amplifiers, placed on boards attached to the detector modules just outside the cryostat. The amplified signals were discriminated and fed into a "multi-hit time recorder" (MHTR) system developed at LHEP-Bern, which sampled the signals at an effective rate of 600 MS/s. Readout logic calculated the time difference between each hit in the strips and the externally provided trigger. The discriminated strip signals were also counted by scalers to monitor on-line the beam profile.

The analog signals from the detector backplanes were read out by amplifiers placed on the same PCB of the strip front-end electronics, and they were recorded by a LeCroy 584 1 GHz oscilloscope. Special runs with non-amplified pulses were also taken to observe the unshaped Pb ion signals.

4.2 Results from Pb ion test runs

The Beamscope was exposed for 42 days to the CERN-SPS high intensity Pb beam. The average beam intensity was ~7×10^7 ions per burst of 4.5 s duration. The fluence was estimated by measuring the beam intensity and normalizing to the fraction of the beam passing through the beamscope planes. The total fluence was about $(5 \pm 2) \times 10^{14}$ Pb ions/cm^2, which, assuming a scaling with the ionization, corresponds to an energy deposit of 90 ± 40 Grad.

The unshaped Pb ion signal from the back-plane of a fresh detector is shown in Figure 37-left (solid dots). The oscilloscope was set to 8 GS/s. We can clearly distinguish a very fast signal rise-time (< 500 ps) dominated by the readout bandwidth, and a long tail. An appropriate shaping was introduced in the amplification stage in order to suppress the tail and reduce the full signal width to 2 ns to improve the double pulse resolution. The open squares in Figure 37-left shows the Pb ion signal after 40 ± 20 Grad, acquired with a sampling rate of 2 GS/s. The signal is broader and its amplitude is reduced by a factor ~20.

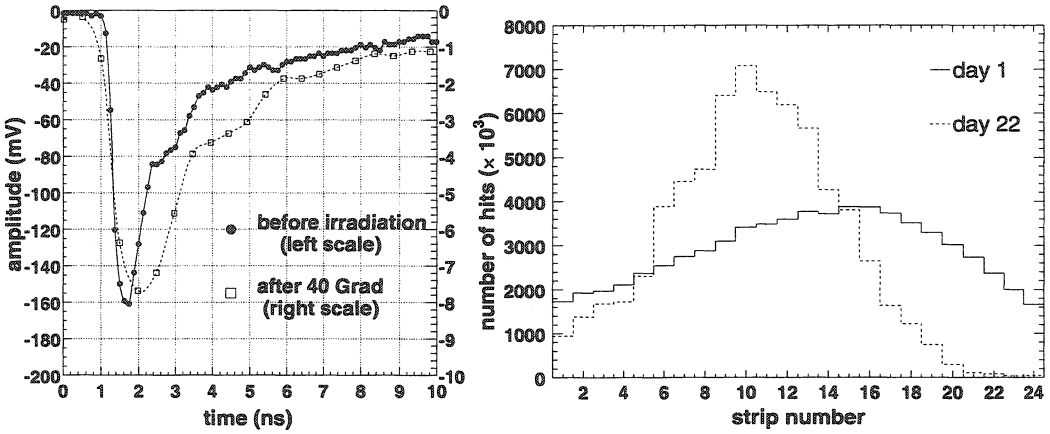

Figure 37: Left: unshaped Pb ion signal before irradiation and after 40 Grad. The bias voltage was 200 V. Right: beam profile in the beginning of the run (solid line) and after 40 Grad (dashed).

Figure 37-right shows the beam profile as measured on-line by the scalers with an cut on the time of arrival. A gaussian fit of the distribution gives $\sigma = 1.0 \pm 0.1$ ns, which was unprecedented 50 μm resolution, larger on day 1 (solid line) than on day 22 (dashed) of the run. Similar profiles have been obtained in the other planes, showing a slightly larger size of the beam in the horizontal direction.

Figure 38-left shows the distribution of the time of arrival with respect to the trigger of all the hits in the strips, as measured by the MHTR on the last day of the run, after normalising the strip distributions to the same mean value. The entries on the sides of the peak correspond to ions passing before or after the trigger, which can be rejected off-line applying an appropriate verified not to change with the bias voltages and the dose.

Figure 38-right shows the correlation between the clusters in the planes 2 and 4 after 40 ± 20 Grad, selecting only hits within 3 σ from the trigger.

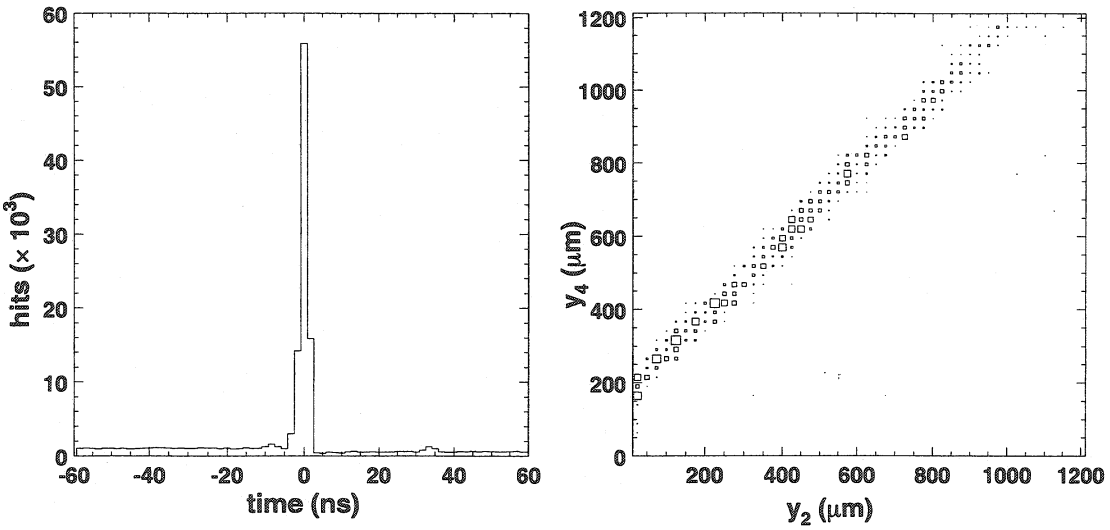

Figure 38: Left: distribution of the time of arrival of the hits in all strips from the MHTR system (normalized to the same mean). Right: correlation between the hits in the strips of plane 2 and 4, showing a misalignment of ~200μm.

The average cluster size as a function of the discriminator threshold is shown in Figure 39-left. Contrary to what is expected in segmented silicon detectors [ref-IR], the cluster size increases with the bias. Indeed, the fraction of clusters of size 1 goes from 94% at 40 V to 75% at 100 V, while the fraction of clusters of size 2 increase from 5.6% to 18%. We believe that this is due to the fact that the Pb ions produce along their trajectory in the silicon bulk a big cloud of electron-hole pairs, which screens the electric field for the carriers which are in the middle of the cloud. By increasing the bias voltage, a bigger amount of charge moves toward the electrodes contributing to the signal, and increasing the probability of creating larger size clusters.

Figure 39-right shows the average pulse height measured on the detector back-plane as a function of the applied bias voltage at different doses. After 20 days we had to increase the amplifier gain on the back-planes by a factor 3 to obtain measurable signals. The data seem to indicate that after a certain dose the signal amplitude does not depend on the bias voltage, at least in the accessible range.

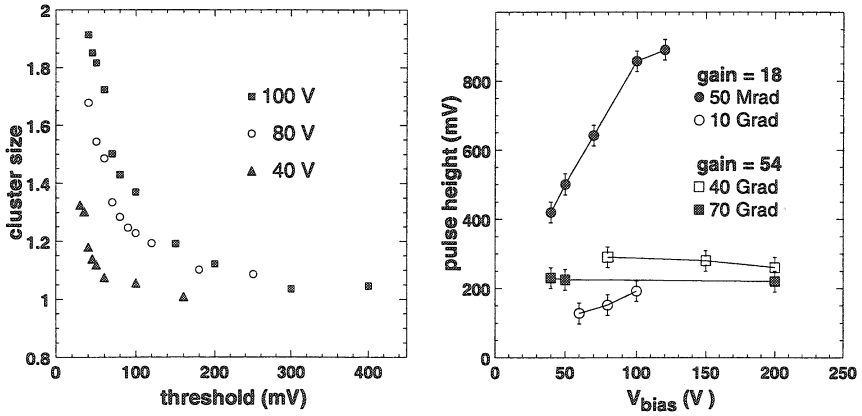

Figure 39: Left: average cluster size as a function of the discriminator threshold for different bias voltages. Right: evolution of the pulse height with the dose. Note that after 40 Grad the amplifier gain was increased by a factor 3.

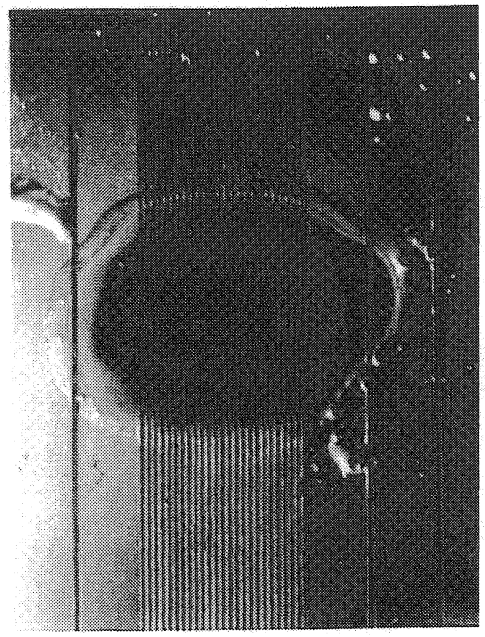

Figure 40: Microscope photograph of one beamscope plane after the 42-day Pb beam exposure. The beam profile center on the narrow strips can be clearly seen.

A photograph of one of the beamscope planes after the 42-day run is shown in Figure 40. The vertical pattern is the Al layer of the narrow strips in the center and of the wide strips on the sides. The region irradiated by the beam can be clearly seen. The same "image" is observed on the other three planes. It seems like the radiation introduced chemical modifications of the silicon bulk and surface, which are not fully understood. On the other hand, it is impressive that such a sensor can still detect signals, and this is only possible when it is operated at 130 K.

4.3 The proton Beamscope

The main difference between the proton and the heavy ion beamscopes is the front-end readout chip placed on the proton detector module, one per plane, close to the microstrip sensor. The chip, developed by the CERN Microelectronics group, provides fast amplification of the signals generated by the protons in the beamscope sensor. The analog output of the chip is fed into the amplifier-shaping stage of the heavy ions, placed outside of the cryostat. In this way, all the readout chain external to the cryostat remains the same in the two versions of the beamscope.

The front-end chip, manufactured in 0.25 μm CMOS technology, has 32 channels and a size of 2×4 mm^2. Each channel has an active feedback amplifier, whose performance is controlled by seven externally adjustable bias currents and voltages. The design was optimized for operation at 130 K to achieve a fast shaping time and low input noise figure.

Figure 41 shows the new module design, including the front-end chip and the new biasing circuitry. Also, a longer sensor is used to provide alignment of the beamscope with respect to the other NA60 vertex detectors by using common tracks. The geometry of the module, as well as the design of the vacuum chamber, were modified in order to fit into the vertex magnet of NA60, shown in the photograph of the installation in Figure 42. The two tracking stations of the beamscope are at 45° with respect to each other in order to solve hit ambiguities.

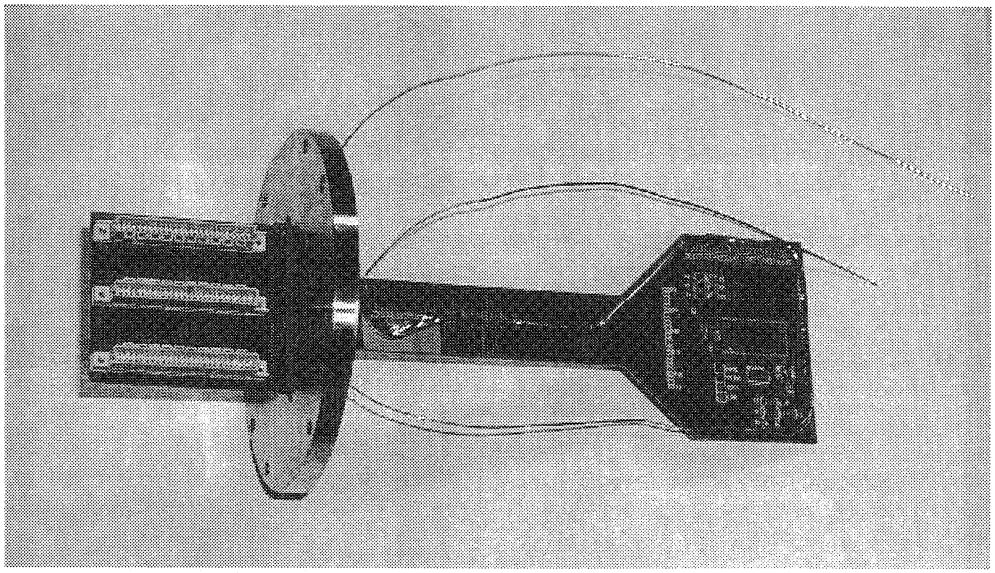

Figure 41: Detector module for the proton beamscope.

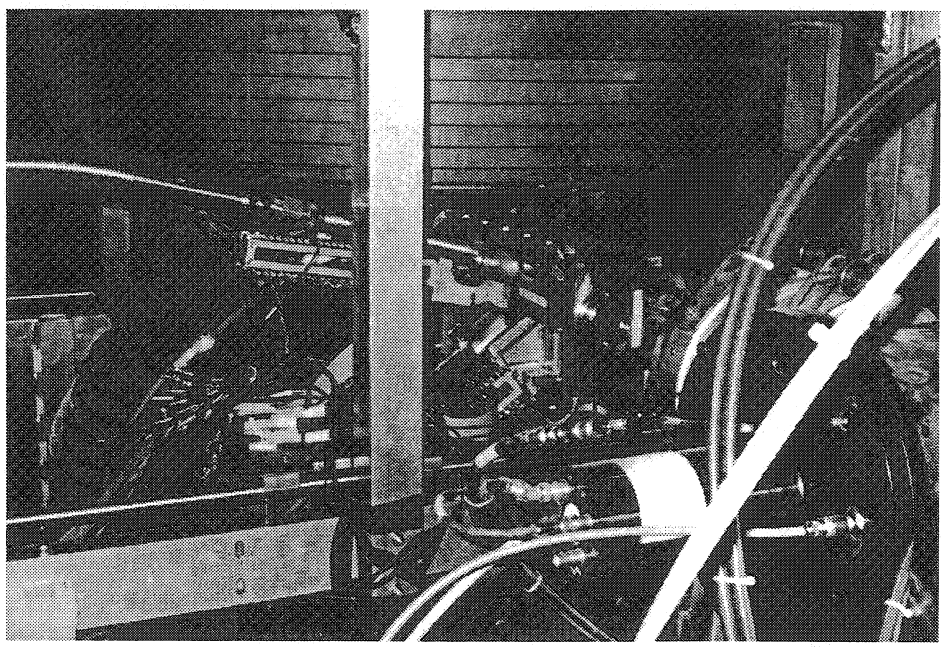

Figure 42: Proton beamscope installed in the NA60 vertex dipole magnet for the commissioning run of fall 2001.

The detector was exposed for ~10 days to the CERN-SPS primary proton beam. The average beam intensity was around 10^6 protons/spill, except for a few hours of irradiation period at 10^9 protons/spill. The beam had a special 25 ns bunch structure for tests in view of LHC.

Figure 43 shows the strip signal at low (left) and high (right) beam intensities. The signal was recorded by an oscilloscope after the front-end chip, the shaping and ~50 m of cable, which brought the signal from the beam area to the counting room. The full width signal is about 5 ns allowing a good double-pulse resolution even at high rate. The shaping time of the chip was measured independently in the laboratory to be ~3.5 ns at 130 K.

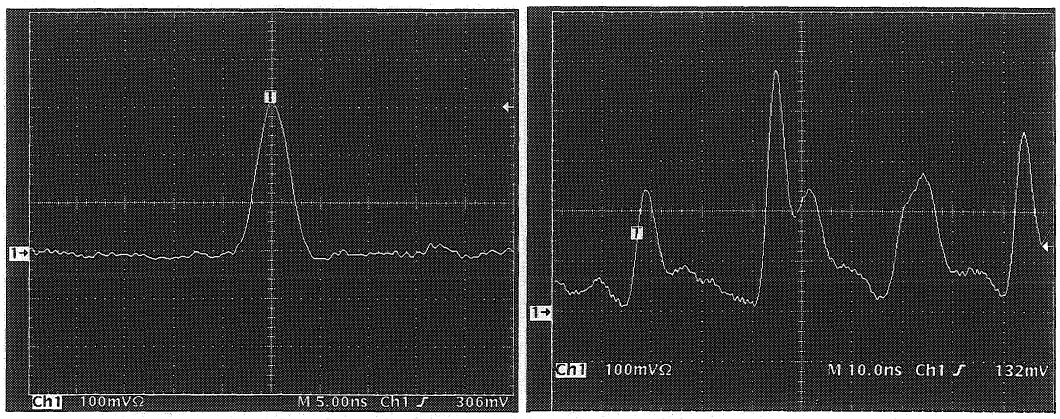

Figure 43: strip signal as seen on the oscilloscope after the front-end chip, the shaping and 50 m of cable. Left: low-intensity beam. Right: high-intensity beam.

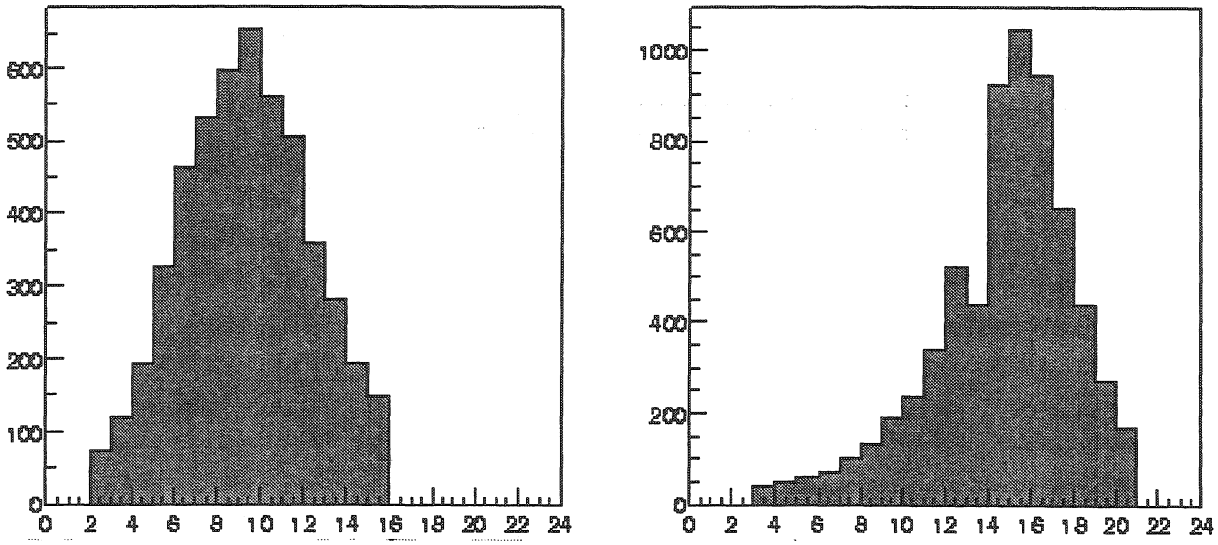

Figure 44: Proton beam profiles in the vertical (left) and horizontal (right) direction as measured on-line by the beamscope.

The beam profile as recorded on-line in the four beamscope planes is shown in Figure 44. Figure 45 shows the MHTR distribution for one strip integrated over several spills. The readout window was ~200 ns in order to observe the 25 ns beam structure. The central higher peak corresponds to the event which are in time with the trigger and which will therefore be selected for the analysis. The broader distribution compared to the heavy ions (see Figure 38 left) is due to a larger jitter in the trigger used for the commissioning run.

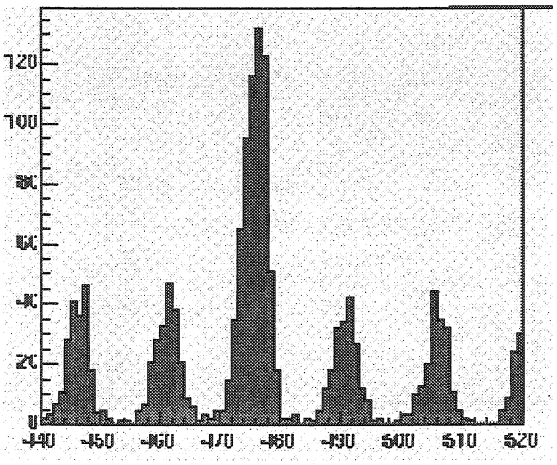

Figure 45: MHTR distribution for one strip integrated over several spills. The 25 ns beam structure is clearly visible.

References of Section 4

[1] NA60 Proposal: SPSC / P316, CERN / SPSC 2000-010, 7 March 2000

[2] K. Borer et al., *RD39 Status Report*, CERN/LHCC 2000-010, 6 January 2000

5 NOVEL HIGH-INTENSITY BEAM MONITOR

Silicon at very low temperatures can be used to monitor ionizing beam particles by measuring the excess current generated in the device. The steady state current will remain negligible even after the device is exposed to high radiation doses provided that the detector is operated at cryogenic temperatures. In this condition exposing the device to an incoming particle beam results in a continuos drift of excited electron-hole pairs due to the applied electric potential. This in turn corresponds to an electrical current proportional to the number of incoming particles.

It is therefore possible to use such a device for on-line measurement of beam intensity and position, and also for dose monitoring. Indeed, segmenting one of the two metal contacts and providing each of the segments with its own current sink, it is possible to monitor the position of the incoming beam. Moreover since there is no increase in the leakage current that could affect the signal to noise ratio, it is possible to calibrate the device and use the integrated current to give a precise estimation of the accumulated number of ionizing particles or overall dose.

As proof of concept, we have fabricated silicon pad detectors consisting of an array of 9 square pads covering an area of 5×5 mm^2. The structure consisted of a high-resistivity n-type silicon substrate, with a 3 by 3 matrix of p-type implant on the front side, while the back side was homogeneously n-type implanted and covered with a thin metal layer. The back side of the detector is connected to a DC bias voltage while the 9 segments on the opposite side are connected to 9 current sensitive devices.

It is worth mentioning that most of the semiconductor detectors come in the form of diodes since, in order to decrease the leakage current at room temperature, a current-blocking contact is needed. However, the resistivity of a silicon detector being dramatically increased at cryogenic temperatures, a simpler configuration can be used. For instance, a low-cost device can be obtained by a simple metal deposition on the two sides of the device.

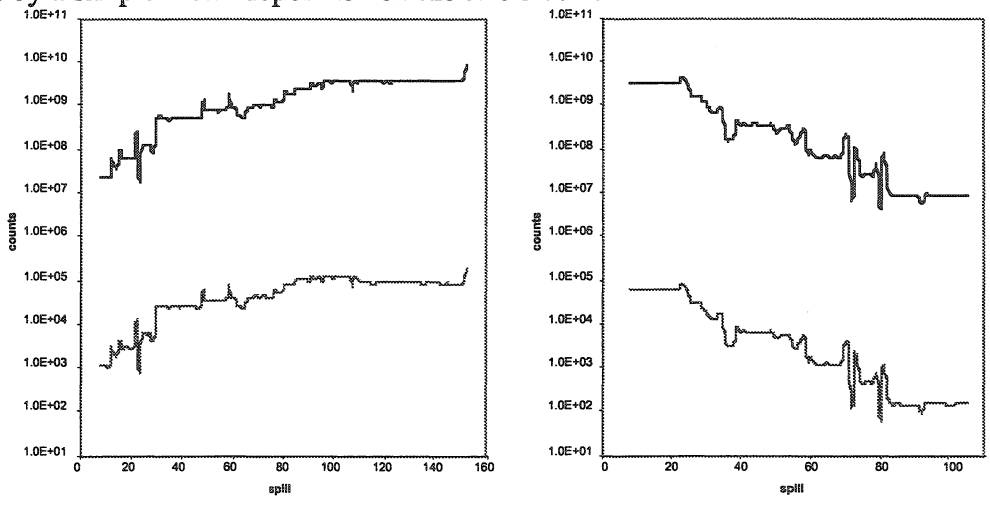

Figure 46: calibrated number of protons per spill as measured by the NA50 proportional chamber (top curves) and counts in the novel cryogenic silicon counter (bottom curves) as a function of the spill number, before (left) and after (right) 50 Mrad.

The silicon pad detector was placed inside a beam cryostat and exposed to the high-intensity CERN-SPS proton and Pb ion beams. The operating temperature was kept around

80 K. Here we report only on the data collected with the proton beam, but similar results have been obtained with Pb ions.

Figure 46 shows the comparison between the counts integrated over one spill of novel silicon pad counter (bottom curves) and the calibrated reading of a proportional chamber (top curves). As shown in the left plot, the beam intensity was slowly increased from ~4×10^7 to ~1×10^{10} protons/spill. Afterward an irradiation period at the maximum intensity, during which an almost uniform dose of ~50 Mrad was integrated over the pad, the intensity was again lowered down to ~1×10^7 protons/spill, as illustrated in the right plot. It is clear that the beam intensity measured by the silicon detector perfectly mimics the one measured by the proportional counter, even after irradiation.

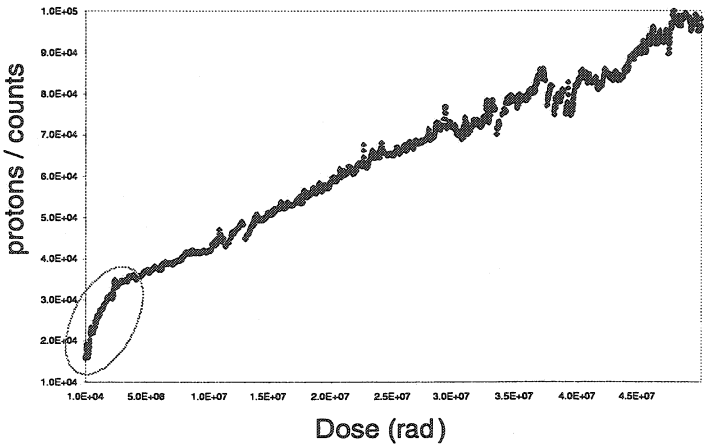

Figure 47: calibration evolution as a function of the integrated dose. Protons / counts = (32 + 1.4 × Dose) × 10^3

Figure 47 shows the ratio between the counts in the silicon pad detector and the proportional chamber. From the plot it is clear that the calibration of the silicon device evolves with the dose. Apart from a stronger dependence at low doses, the calibration varies linearly with the dose. Once the device is calibrated, it can be used to give an unprecedented precise estimation of the accumulated dose even at dose rates, which preclude the counting of individual pulses.

This new low-cost radiation-hard detector can not only be use for beam monitoring, but also for beam loss monitoring in accelerators, luminosity measurements in collider experiments, or for monitoring of X-ray or hadron beams for radiotherapy.

6 ROMAN POT MICROSTRIP DETECTORS FOR TOTEM

RD39 is developing low-temperature silicon microstrip tracker modules in collaboration with the TOTEM [1] experiment. These detectors will be mounted in the Roman pots and will be used for tracking the protons of forward elastic scattering at LHC. The lowest momentum transfer requires tracking at a distance of a few millimeters from the LHC beam. This calls for an "edgeless" detector, which has no dead material on its edge facing the beam, apart from a thin metallic window providing vacuum and RF isolation between the machine and the detector. First tests at BNL, described in subsection 6.1, prove that their edge treatment is appropriate, and that operation at 130 K lowers the sensor current to a reasonable level.

The TOTEM experiment runs at low luminosity, which is obtained by reducing the number of bunches in the machine, and by increasing the beta function of the machine optics at the intersection point. Although the elastic and background event rates required by the experiment are such that no substantial damage can be expected during the few months of data taking of TOTEM, the background radiation in the Roman pot areas during high-luminosity operation can be so high that the sensors and readout electronics need to be radiation hardened, in particular if new luminosity measurement or calibration is required after several years of operation at a high luminosity. Moreover, the Roman pot detectors have other possible applications at high luminosity, requiring extremely high radiation resistance.

In the year 2000 RD39 started the development of efficient thermal designs and module microassembly techniques, in view of the application of the low-temperature detectors in TOTEM high-radiation areas with limited access. This is described in Subsection 6.2.

A test bench was built for measuring the basic engineering parametrs in two-phase flow of suitable coolants such as Ar, CH_4 and N_2. These activities are now also integrated in the RD39/TOTEM project, and are described in Subsection 6.3.

The module design, cooling and microassembly techniques developed in this project would be appropriate in large tracker arrays as well; this will be discussed in Section 9.

6.1 Edgeless sensors

High resistivity (4-6 kΩ·cm) $p^+/n/n^+$ Si pad detectors, with a thickness of 400 μm, were processed at BNL's Semiconductor Detector Development and Processing Lab (SDDPL) on 100 mm diameter Si wafers. The dicing tools used were the BNL standard laser dicing machine and a diamond point pen for hand scribing. The dicing was performed from either the front p^+ side or the back n^+ side. The laser dicing depth was about one half of the detector thickness. The detectors had an active area of 0.25 cm^2 (5x5 mm^2) before dicing, reduced to 0.228 cm^2 after dicing. Standard I-V and C-V (at a frequency of 100 kHz) measurements were done at RT before and after dicing, and after RT aging in air. TCT measurements using a red laser were performed on all samples from RT down to 130 K. Some detectors were tested for charge collection efficiency with a ^{90}Sr (MIP) source at cryogenic temperatures using an automated CCE setup at LIP Algarve, Portugal. Samples used for these studies were from the batch #1 listed in Table 1.

Sample #	Sample type	Dicing method	Dicing side
799-22	$p^+/n/n^+$	Scribing	back
799-23	$p^+/n/n^+$	Laser cut	back
799-26	$p^+/n/n^+$	Laser cut	front

Table 6: Samples in the batch #1 for cutting (no edge treatment after dicing)

Some detectors were edge-etched after dicing. Before the dicing, these detectors were coated with black wax on both sides to protect the sensitive area from etching. In this way only the cut edge would be etched during the process. The uncoated edge was etched in an acid solution (HNO_3 : HF = 3:1). Etching time should be long enough to remove cutting-caused defects completely, normally 1–2 minutes. The samples in this batch #2 are listed in Table 7.

Sample #	Sample type	Dicing method	Dicing side
798-9	$p^+/n/n^+$	Laser cut	front
798-21	$p^+/n/n^+$	Laser cut	back

Table 7: Samples in the batch #2 with edge etching treatment after dicing

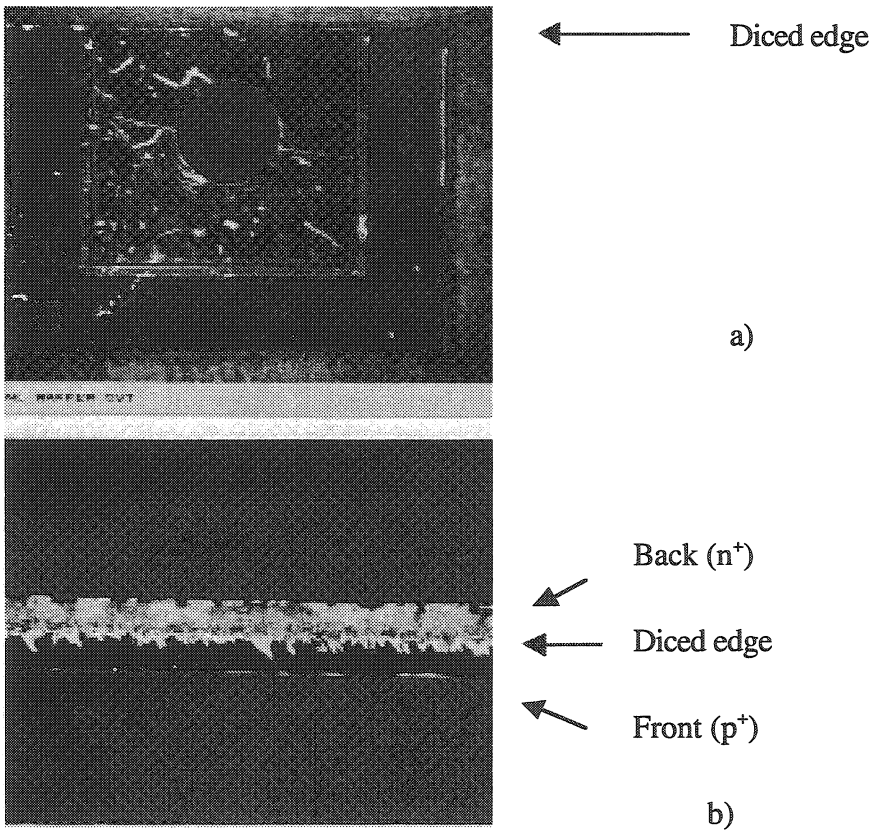

Figure 48: Photographs of a laser diced (from backside) Si detector: a) Top view; and b) cross section view.

Figure 48 shows the edge of a detector, laser diced from the backside, seen from the top (or front p^+-side) (Figure 48 a) and from the side of the edge (Figure 48 b). It is clear from the cross section view (Figure 48 b) that the portion of the edge surface damaged by the laser cutting, adjacent to the n^+-side, is much rougher than the break-off portion adjacent to the p^+-

side. Similar pictures were obtained for a detector diced with a scribing point pen. Since the hand scribing is less deep and not well controllable, the break-off cross section is not uniform, but it is still quite smooth all across.

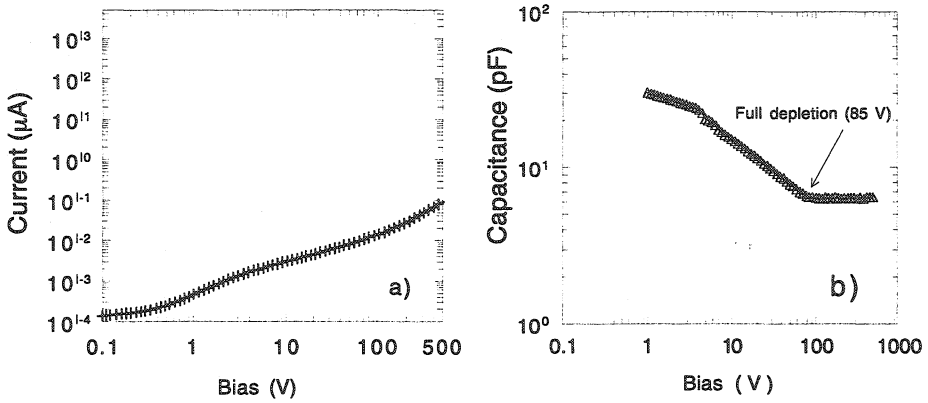

Figure 49: I-V a) and C-V b) characteristics of a detector (# 799-22) before laser cutting

Typical I-V and C-V characteristics of detectors before laser cutting are shown in Figure 49. The current was typically of the order of a few nA at full depletion voltage (V_{fd} = 85-100 V), and there was no breakdown up to 500 V.

Figure 50 shows the I-V and C-V data of a detector, laser diced from the back side (n^+ side), immediately after dicing (within one hour), and after one day RT aging in air. Immediately after dicing the leakage current was increased drastically by five orders of magnitude, with a current at $V = V_{fd}$ (I_{fd}) close to 1 mA, as shown in Figure 50 a. Due to this high leakage current, a C-V measurement could not yield data adequate for determining V_{fd}, as seen in Figure 50 b.

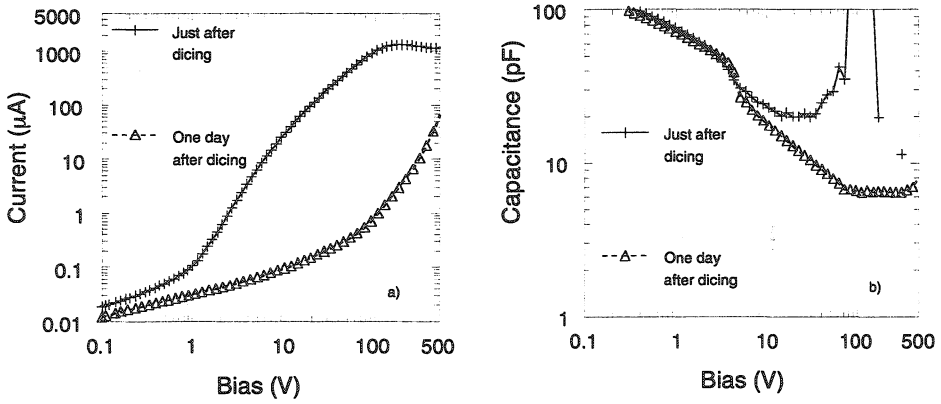

Figure 50: I-V a) and C-V b) characteristics of detector #799-23 laser diced from the backside, immediately after and one day after dicing.

Similar I-V and C-V data were obtained for detectors diced with laser from the front side, and for detectors diced with scribing from the back side and front side, when measured immediately after dicing. However, just after overnight aging at RT in air, the leakage current improved by three orders of magnitude for detectors diced from the back side with laser or scribing pen. Figure 50 a shows the I-V characteristics of a detector diced with laser from the backside. The value of I_{fd} is only 500 nA and the leakage current at 500 volts is about 70 μA. Now a perfect C-V curve could be measured, as shown in Figure 50 b which yields V_{fd} = 85 V. Similar results were obtained for a detector scribed by a diamond pen from the backside.

However, there is little aging improvement in the leakage current and in the C-V characteristic, for detectors laser diced from the front side. In the latter case, the value of I_{fd} only dropped slightly from 2 mA to 1.2 mA after overnight aging. The improvement seen in detectors diced from the backside is most likely due to the oxidation of the silicon with native oxide, which passivates the cut surface. The time constant for this aging process is ≤ 12 hours, since longer aging time did not produce further improvement. Since the dicing from the front side is cutting directly into the p^+-n junction, which yields a more damaged surface at and near the junction (see see Figure 48 b, just switch the n^+ and p^+ sides) with the highest electric field, it is apparent that 1) the portion of the actual laser cutting is more damaging (consistent with the rougher image in Figure 48 b) than the break-off portion, and 2) the RT aging process did not passivate the most damaged (caused by actual laser cut) region near the p^+ junction. It is clear that dicing from the ohmic side (non-junction side) is absolutely necessary to prevent large leakage current. Since the cutting with a scribing pen is also highly uncontrollable due to the unpredictable breaking direction, and it can only cut straight lines, the best choice is obviously the dicing by the laser tool from the ohmic side. It is clear that the degree of the damage on the cutting cross section caused by laser dicing controls the detector leakage current and breakdown behavior. In order to minimize this damage, some detector edges were etched as stated in Table 7.

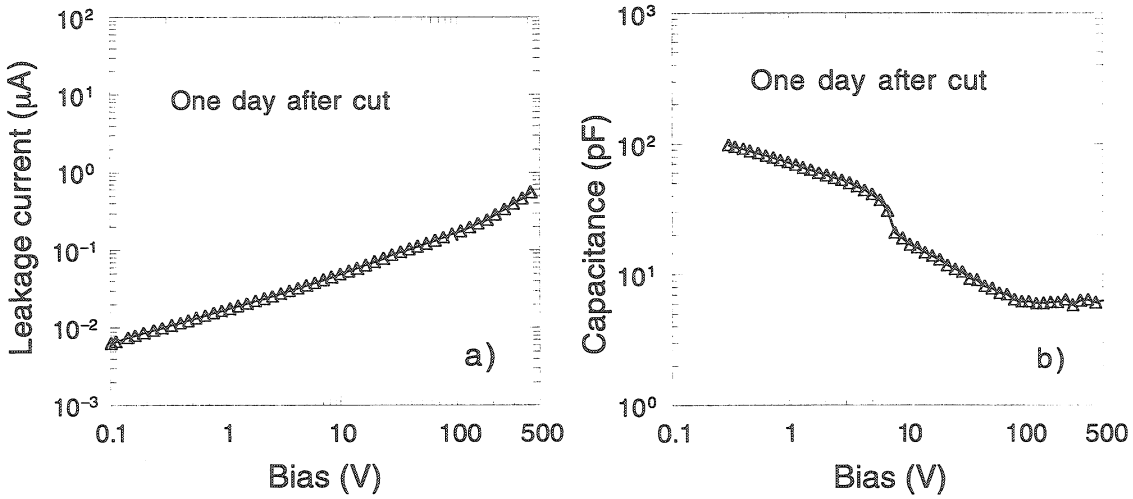

Figure 51: I-V a) and C-V b) characteristics of detector #798-9 laser diced from the front side and treated with edge etching. Measured one day after dicing.

Figure 51 shows the typical I-V and C-V data for a detector laser diced from the front side followed by edge etching treatment. It is clear that the leakage current is further decreased by more than an order of magnitude after edge etching treatment: at full depletion (about 90 V) the leakage current is about 0.15 μA, and at V = 400 V it is about 0.5 μA, as compared with leakage current values of 1 μA and 40 μA at corresponding voltages for a detector without edge etching treatment. The fact that this detector is being laser cut from the front side indicates that mechanical damage caused by the laser dicing can be removed by chemical etching. Similar results (lower leakage currents) have been found for detectors laser diced from the back side and chemically etched. It is obvious that, with chemical treatment, there is no difference between the front side and back side dicing. This is important since to cut a non-straight pattern, e.g. a hole in the wafer, one needs to cut it all the way through, which sees no

difference for front and back side dicing.We should mention here that the "edgeless" devices, diced from the back side and after aging, also behave nicely as detectors. TCT measurements [4] using a red laser, with an absorption length of a few μm in Si, were performed on these detectors from RT down to 130 K. Figure 52 shows the laser-induced current pulse response at 130 K and various *V* for a detector laser diced from the back side (not edge-etched). The current pulse response shapes are caused by holes, induced by red laser light illumination on the back (n^+) side of the detector, drifting in the electrical field that is provided by biasing the detector over the full depletion. It is clear that normal current pulse shapes are observed in this detector: pulse width decreasing with bias; current increasing with time (holes drifting from low field region to high field region); the collected charge (the area) is always preserved. The edgeless detectors shown here can be biased up to 900 V at 130 K.

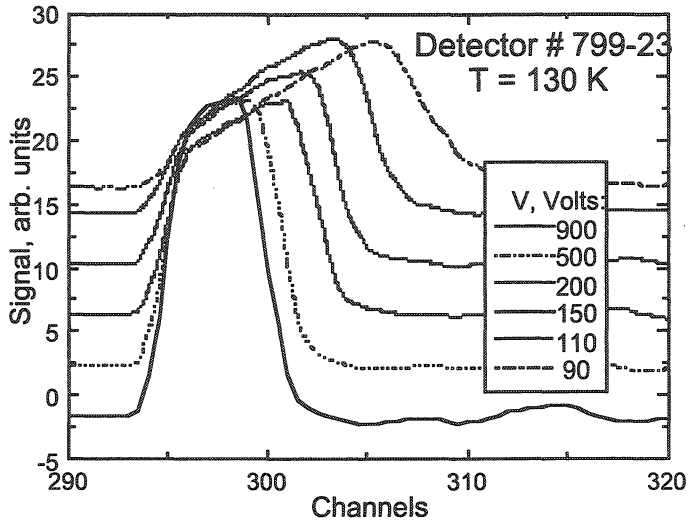

Figure 52: Current pulse shape (holes) of a detector laser diced from the backside.

The substantially narrowed pulse width is due to increased carrier mobility at lowered temperature. The only abnormal behavior observed in laser diced "edgeless" detectors is the temperature dependence of the detector leakage current. It is well known that, for a normal detector (before dicing in our case), the leakage current decreases steeply with inverse temperature. This is due to the fact that for a normal detector, the main component in its leakage current is the bulk current which decreases exponentially with inverse temperature, due to thermally activated processes of the bulk defects. For laser diced "edgeless" detectors in our study, the main component of the leakage current is the edge current, which is not affected by bulk defects. Although the leakage currents for our "edgeless" detectors still decrease with decreasing temperature, the rate of this decrease is much smaller, and the absolute value of the leakage current may still be as high as 0.1 to 1 nA at 130-150 K.

In order to check the actual MIP charge collection efficiency for these "edgeless" detectors, some detectors were measured using a 0.1 mCi ^{90}Sr beta source at LIP in Faro, Portugal. Figure 53 shows a detector laser cut from the backside and mounted on a PC board for CCE measurement. It was found that one can achieve 100% CCE at a bias of 100 V or less for detectors diced from the backside at temperatures of 270 K or less. For detectors diced from the front, however, one can only achieve 28.5% CCE (at 100 V) even at 110 K. This is due to the very high leakage current, in the order of μA's even at 110 K, which entails a large voltage

drop on the bias resistor that is 20 MΩ. This large bias drop on the bias resistor, which can be large than 20 volts, makes the effective voltage drop on the detector less than the detector full depletion voltage, causing a partial charge collection. The CCE data are summarized in Table 8.

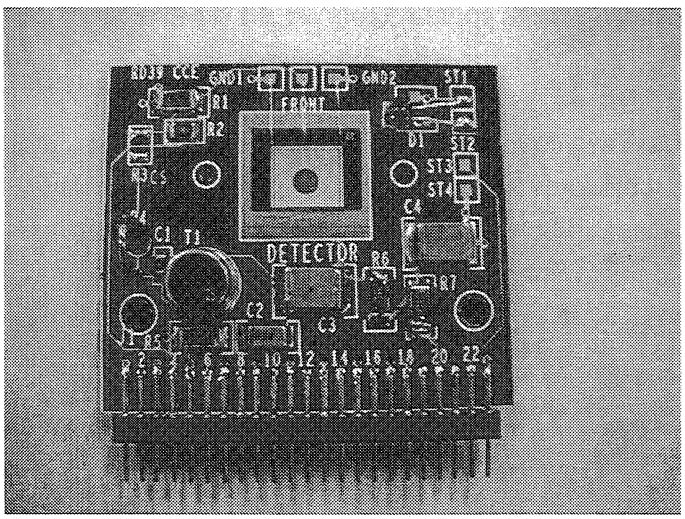

Figure 53: An "Edgeless" detector mounted on the PCB for CCE measurement

Detector #	Dicing method	Bias (V)	*T* (K)	CCE(%)
799-23	Laser, back	50	≤ 270	100
799-22	Scribe, back	100	≤ 270	100
799-26	Laser, front	100	110	28.5

Table 8: CCE data of "edgeless" detectors

In summary, the main issue to get a workable "edgeless" detector is to control and minimize the edge current. We have demonstrated that this can be achieved with the dicing and edge treatment technology developed in this study: 1) dicing from the non-sensitive side (the ohmic side) of the detector, and 2) chemical etching of the cut edge to remove the damage. It is obvious from the data presented above that it is essential to treat the damaged edge surface to get a low leakage current. Our results show that by chemical etching of the edge surface, the surface leakage may be further reduced by more than one order of magnitude. With chemical etching, one can obtain detectors with minimum leakage by laser dicing from either side (front or back side). With the technologies developed in this study, we have obtained working detectors that can be biased up to 500 V from RT down to 130 K without breakdown, and with a reasonable current below 1 μA at RT and a few nA at cryogenic temperatures. The etching technology developed here is non-invasive for the sensitive area of the detector, which is essential for its application to segmented strip and pixel detectors and for preserving the "edgeless feature".

It is interesting to point out that further reduction of the surface current may be achieved by irradiation of the detectors due to the surface passivation effect: reduction of edge current by deep level trapping [5]. This will make the application of "edgeless" detectors in a real experiment with radiation environment even more feasible.

6.2 TOTEM module design

The TOTEM strip detector prototype module design, shown in Figure 54, is based on single-sided sensors mounted on a base plate together with a pitch adapter and a hybrid readout circuit with four APV25 chips. Between the pitch adapter and the base plate there is a carbon fiber composite (CFC) spacer of 0.6 mm thickness, in which a cupronickel micropipe of 0.6 mm diameter is integrated for providing cooling to the hybrid and sensor of the module, while separating them thermally.

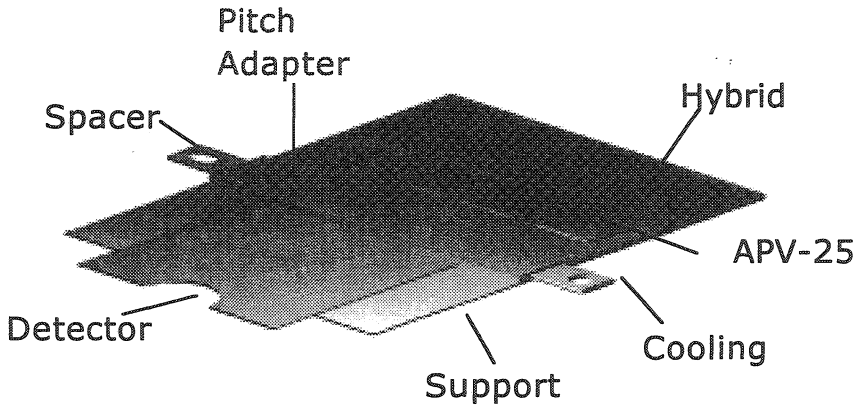

Figure 54: The main components of the single-sided TOTEM module

In each Roman pot there will be two such modules, having crossed strips for providing x- and y-coordinates for traversing charged particles.

An alignment hole and a slot will be located at the ends of the CFC spacer, close to the cooling pipe (see Figure 54). The pipe provides also cooling to the support points, in order to prevent the heat load conducted along the support rods from being applied directly to the detector module. A third support point (not shown) is located at the backside of the hybrid. The sensor has a semicircular indentation which will be precisely located close to the thin-wall window of the pot, located at a few millimeters from the LHC beam during the collection of small-angle elastic scattering data. In this area the sensor is edgeless (see previous Subsection) so that the sensitive area can be extended as close as possible to the beam.

Principle of precision alignment

The alignment of the cooled sensors with respect to the Roman pot window will be based on the use of precision pins and holes, which position the module on its support structure. The support structure is based on a flat plate which will be at room temperature. The plate will be aligned precisely inside the pot using also precision dowel pins and precision holes machined to the bottom of the pot. The three support rods are perpendicular to the plate, and they are thermally isolating. They also feature compensation of the thermal dilatation of the module, achieved by making one of the rods rigid, the second slightly pivotable along the line connecting it to the rigid rod, and the third slightly pivotable in two directions. These degrees of freedom are achieved by the appropriate design of the elasticity of the rods.

Mechanical design and choice of materials

The choice of the module materials is determined by thermal conductivity and thermal dilatation, in addition to elastic properties. Silicon is a very good heat spreader at low temperatures, with a thermal conductivity of about 7 W/cmK at 120 K (Figure 55). In order to achieve small temperature gradients and a uniform temperature profile in the module, we are planning to use silicon not only for the strip detector itself, but also as a constructional material. This also avoids the generation of mechanical stress or deformation during cool-down due to differences in thermal expansion.

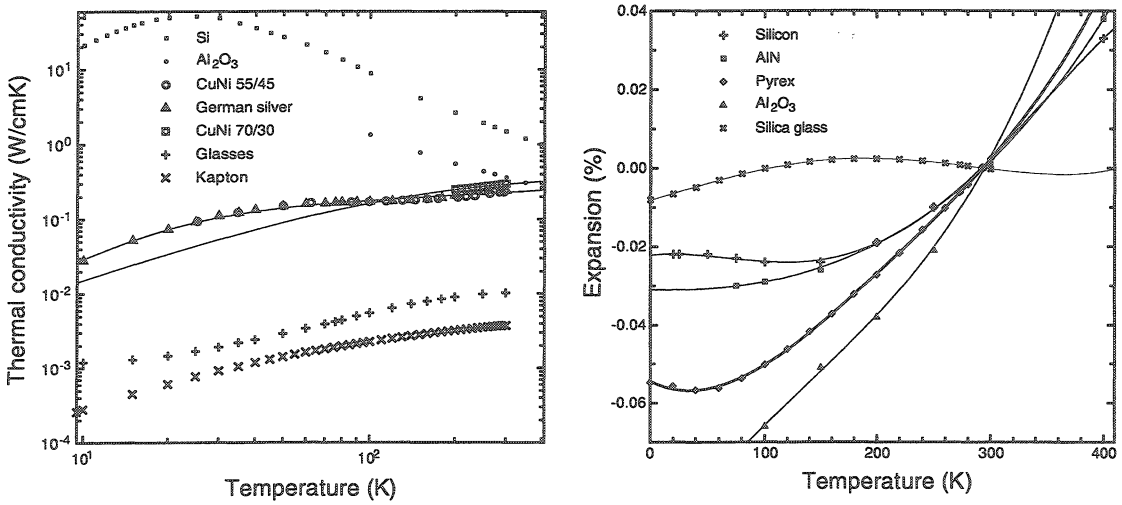

Figure 55: Thermal conductivity and thermal expansion of silicon as a function of temperature, compared with other materials which could be used in the construction of detector modules

Therefore, silicon will be used for all the components as far as possible. For thermal separation, a CuNi cooling pipe is inserted between the hybrid and the silicon sensor, embedded in a CF spacer in order to match thermal dilatation with the silicon support. A direct cooling path is established towards the hybrid (the main heat source) and an indirect one through the support towards the detector. Tests will be carried out to prove the mechanical stability during thermal cycling and the radiation tolerance of the assembly.

Modeling of the thermal behavior

Thermal loads: Operating the edgeless silicon sensors at 130 K entails a very small leakage current (a few nA) in the sensor, and consequently there is at most 1 μW of heat generated in the sensor itself. The main heat loads come from power dissipation in the readout electronics and from thermal radiation.

It is planned to use the CMS CMOS chip APV25-S1, which was already proven to work at liquid nitrogen temperature (see Section 7). The APV25 is a 128-channel chip with each channel dissipating 2.31 mW. Therefore, the heat load per double-sided module with 10 readout chips is about 3 W.

Thermal radiation occurs between the Roman pot, which is at about 300 K, and the detector module cooled at 130 K. For calculation we are using the formula for a diffuse-gray surface enclosure. With the total hemispherical emissivities of $\varepsilon_{Al} = 0.06$ for the aluminium pot and $\varepsilon_{Si} = 0.19$ for silicon, one module absorbs a thermal radiation heat load of 235 mW.

The thermal behavior of the half-module with vertical strips has been analyzed using finite element modeling in ANSYS. Heat loads were applied as heat flux boundaries, with the APV25 power dissipation of 4 x 300 mW applied on their bottom surfaces and the overall radiation heat load of 235 mW equally distributed on all surfaces. The heat sink was defined with a fluid bulk temperature inside the cooling pipe of 120 K and an assumed heat transfer coefficient of 10^4 W/m^2K.

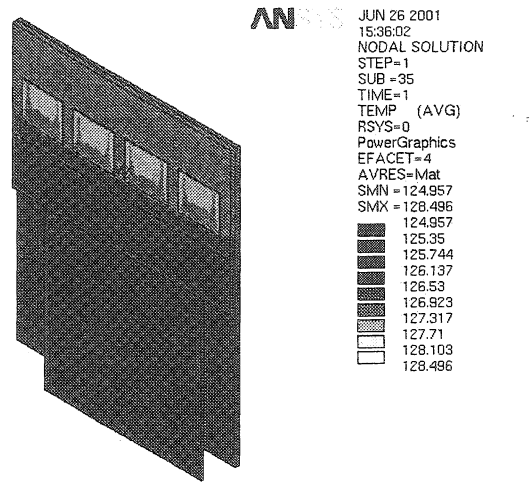

Figure 56: Thermal map of the TOTEM module.

Several geometries and material combinations were studied. The results for a layout with a simple spacer and the materials mentioned before are shown in the figure above. The maximum temperature difference between the fluid saturation temperature and the readout-electronics is less than 10 K. The biggest gradient is located within a small area around the cooling pipe, which is modeled as an epoxy with rather low thermal conductivity. The silicon sensor has a temperature of about 127 K and the hybrid is only marginally warmer.

The regularity of the temperature profile shown in the figure favours silicon to be used as constructional material. Experiments are planned to verify the thermal simulation results.

Gluing silicon to silicon: fused quartz filled epoxies

The thermal dilatation of standard epoxies is one order of magnitude higher than that of silicon. Therefore, when cooling down silicon to silicon joints a lot of stress is induced. This may result in either the joint or substrate cracking.

Several models describing matrix composite properties, such as Kerner's, predict a lower thermal dilatation coefficient for epoxies that are charged with low thermal dilatation particles such as fused quartz. Thus, a series of tests to study the thermo-elastic properties of charged epoxies are being conducted.

Preliminary results prove that we can reduce significantly the thermal dilatation of an epoxy by filling it with an appropriate powder. In the chart we see the comparison between the integral thermal dilatation of pure Stycast 1266 and the same epoxy filled to 40% vol. with fused quartz particles of 2 μm size. The filled epoxy reduced its thermal dilatation at 4.2 K by a factor of 1.6. Mechanical results for the same charged glue show that the Young Modulus increased by a factor of 3.

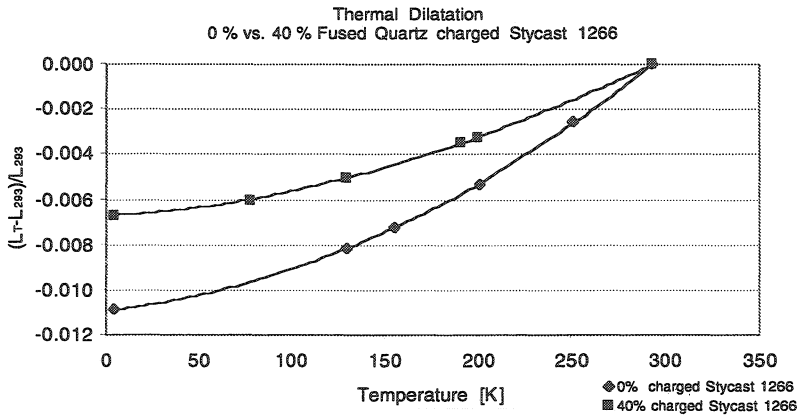

Figure 57: Thermal dilatation of a low-viscosity epoxy, with and without filling by fused quartz powder.

6.3 Microtube cooling of the modules

The basic layout of the cooling system is determined by the operating temperature, the power dissipation of the modules and the location and accessibility of the installation. The Roman pot stations are located in tunnel areas with restricted access and the distance to the intersecting point IP5 is up to 180 m, with distances in-between the stations of about 60 m and 28 m, respectively. Considering a power dissipation of 3 W per module, the only practical solution is to have one autonomous cooling system for each individual Roman pot station. With 4 detector modules per station and all the thermal losses in the system the overall cooling capacity amounts to 20 W.

Our cooling system concept is shown in Figure 58. The cooling capacity generated by a cryocooler is distributed to the detector modules in a closed capillary tube circuit by means of 2-phase flow of argon. The cryocooler is a commercial Stirling or Gifford-McMahon machine. A condenser/receiver-unit is attached to its cold finger, where a two-phase flow of argon is fully condensed and sub-cooled in a following heat exchanger. A cryogenic micropump, which is a new prototype design, generates a suitable pressure head to pump the fluid to the detector modules and compensate for all the pressure losses in the circuit. After the micropump the fluid supply line is split to transport the pressurized fluid through the internal capillaries of 4 coaxial transfer lines to the modules. There, the fluid is evaporated to about 50 % of its latent heat, picking up the heat load of the readout electronics in integrated capillary heat exchangers. The 2-phase argon is returned through the external capillaries of the transfer lines, recombined in one fluid return line and returned to the condenser/receiver unit. The entire volume including the vacuum cryostat, the flexible vacuum hoses and the Roman pots with the detector modules is interconnected, providing a cryogenic insulating vacuum of 10^{-6} mbar.

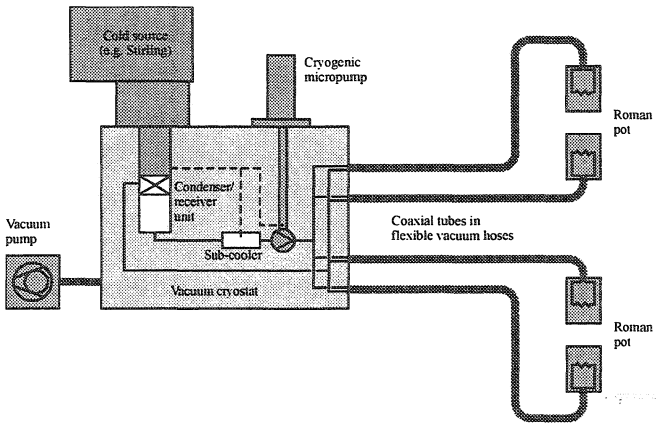

Figure 58: Cryogenic cooling system for the Roman pot stations

The key-component in our system development is the cryogenic micropump, which is based on a commercial micro annular gear pump for room temperature applications. Several modifications as hermetic encapsulation and the change of seals and bearings were necessary to make it suitable for cryogenic operation, with demanding requirements on mechanical precision and cleanness. First preliminary test results shown in Figure 59 are very promising. At a flow rate of argon of 100 mg/s, a pressure head of almost 3 bars was generated at the maximum pumping speed of 6000 rpm. This large pressure head enables a new technology of distributed cooling at a new level of miniaturization, with very small thermal losses, highly efficient heat exchangers and simple control. After a series of experiments and modifications the thermal management of the cooling circuit is now well understood.

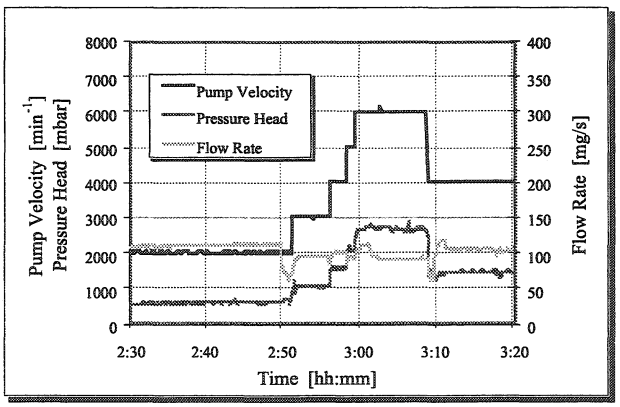

Figure 59: Preliminary test results of the micropump performance

Important engineering parameters for the layout of the cooling circuit and for the design of the capillary heat exchangers in the modules are two-phase flow pressure drop and flow boiling heat transfer.

Unfortunately, there is no universal theory for two-phase flow friction, which usually determines the overall pressure gradient. Correlations only exist for macroscale tubes with hydraulic diameters larger than about 5 mm, whereas in the Roman pot modules we are planning to use capillary pipes of 0.5-0.3 mm inner diameter. Fluid dynamics in these capillaries is rather different due to an increased influence of hydrodynamic boundary layers. The few studies on single-phase flow published so far show that the transition Reynolds numbers decrease with the hydraulic diameter, with critical Reynolds numbers as low as 200-

900. The data also suggest that the friction factor in laminar and turbulent flow is apparently lower than macroscale predictions, which, however, seems to strongly depend on the microchannel geometry. Despite a large uncertainty, the *Storek and Brauer* correlation was used to predict the pressure drop in the module heat exchangers. The correlation is based on the homogeneous flow model and uses a correction factor for the velocity differences between the phases. The results in Figure 60 propose an optimum capillary diameter of 0.3 mm. Experiments are presently carried out with microtubes of different diameter in order to verify our calculations and to derive better general correlations for microscale dimensions.

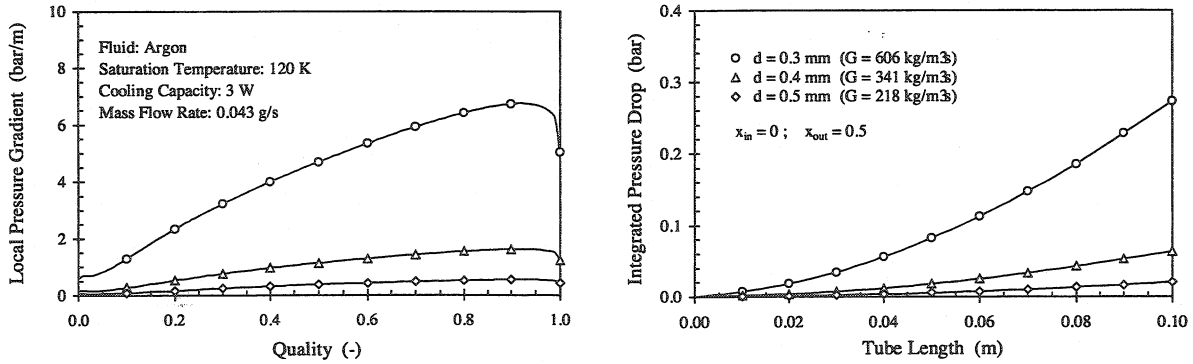

Figure 60: Calculated pressure gradient and integrated pressure drop in the module cooling pipes

The use macroscale correlations for calculating two-phase heat transfer coefficients in microtubes is even more uncertain, because it depends not only on operating conditions and fluid and wall properties, but also on phase distribution, fluid quality and, in case of nucleate boiling, on the wall superheating. In addition, there are new phenomena in microstructures related to the evaporating space necessary for bubble formation, which obviously alter the boiling characteristics significantly as compared to conventional situations. Since general models are not yet available, experimental data are essential for an optimum heat exchanger design. The calculated heat transfer coefficients presented in Figure 61 can only give a general idea, although we do expect high values of several tenths of kW/m^2K. Experiments will be soon carried out in a test stand for measuring the heat transfer coefficients in single- and two-phase flow in capillary pipes of 0.5, 0.4 and 0.3 mm inner diameter.

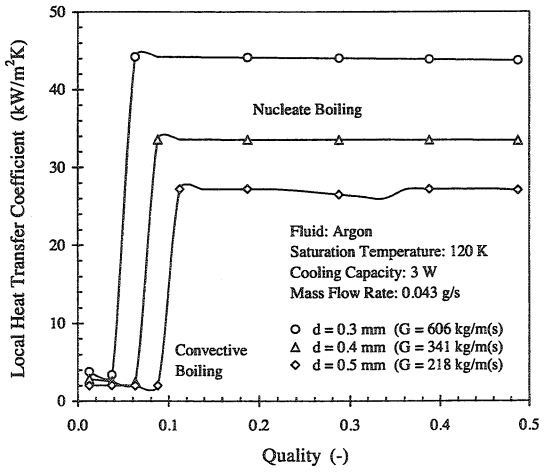

Figure 61: Calculated heat transfer in the module cooling pipes

References of Section 6

[1] TOTEM Technical Proposal, CERN/LHCC 99-7; LHCC/P5 (1999)

[2] L. Evenson, A. Hanneborg, T Happ, A.H. Wuosmaa, and R.R. Betts, "A Fast Low Noise Silicon Detector for Electron Spectroscopy Up to 1 MeV", Nucl. Instr. and Meth. **A326**, pp. 136-143 , 1993.

[3] Z. Li, D. Anderson, B. Barnett, R. Beuttenmuller, W, Chen, C.Y. Chien, M. Frautschi, G. Hu, S. Kwan, D. Lander, S. Mani, S. Pandey, Q. Wang, S. Willard, And X. Xie, "Simulation and Design of Various Configurations of Silicon Detectors for High Irradiation Tolerance Up to $6x10^{14}$ n/cm^2 in LHC Application," Nucl. Instr. and Meth. **A409**, pp. 180-183, 1998.

[4] V. Eremin, N. Strokan, E. Verbitskaya, and Z. Li; "Development of Transient Current and Charge Techniques for Measurement of Effective Impurity Concentration in the Space Charge Region of p-n Junction Detector, Nucl. Instr. and Meth. **A372**, pp. 388-398, 1996

[5] V. Eremin and Z. Li; "Effect of deep level trapping of free carriers on the stabilization of current-voltage characteristics of high resistivity silicon detectors irradiated by high fluence of neutrons", Nucl. Instr. and Meth. **A383**, pp. 528-536 , 1996.

7 COMPASS TRACKER DEVELOPMENT

As tracking detectors for the beam region the COMPASS experiment [1,2] will use segmented double-sided silicon detectors of 300μm thickness, with an active area of 7×5cm^2.

Because of the very high rate of the SPS M2 beam of COMPASS (~10^8 particles/spill), radiation hardness of the silicon detectors is required, and therefore the experiment decided to exploit the Lazarus effect.

The use of silicon detectors at cryogenic temperatures requires the read-out electronics to work in the same range of temperatures. The APV25 0.25μm CMOS read-out chip [3] was demonstrated to be a suitable device for our purposes.

We tested its performances at cryogenic temperatures. The chip was mounted on a dedicated board on which was also located an R-C network for the injection of charge. The board was inserted in a vacuum tight cryostat and operated at a pressure ~10^{-6}mbar. A scan of chip properties between room temperature and 77 K was performed, with special care for the Lazarus region (130 ± 20K). Figure 62 shows the output signal corresponding to 1 MIP equivalent input at room temperature and at 130 K in two chip operating modes [3]. In Figure 63 the noise as function of capacitance at room temperature and 130 K is plotted.

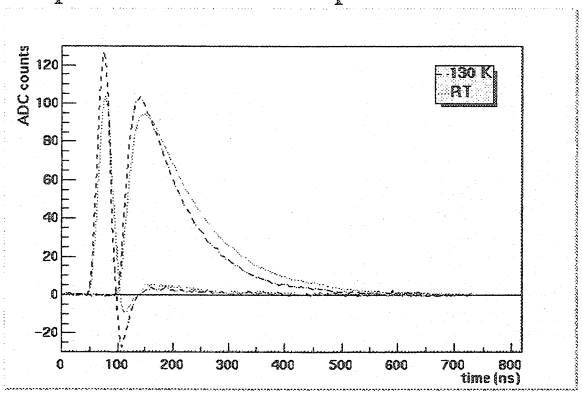

Figure 62: pulse shape corresponding to 1MIP input signal in two operating modes of the chip at room temperature and at 130K

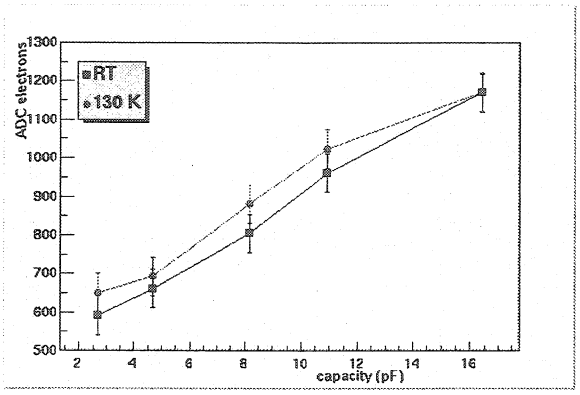

Figure 63: Noise vs. capacitance at room temperature and at 130K

The tests performed show that it is possible to use a CMOS technology read-out chip at cryogenic temperatures.

Nevertheless further studies on this topic are still needed. In particular a project to study the coupling of a silicon detector and an APV25 chip read-out is ongoing.

Because of the relatively large area of the silicon detector used in COMPASS, the design of a suitable cooling system on the read-out board is very important, to guarantee a uniform temperature all over the silicon. To this aim we performed a series of measurements on a test prototype. The test board was a 4-layer PCB with the same dimensions as the COMPASS silicon read-out board. Instead of the detector we used a 300μm thick glass piece and we measured the temperature on 15 point all along the glass with PT100 thermometers, read-out via a NI340 card. A set of parallel resistors was used to simulate the heat dissipation of the read-out chips. The cooling system consisted of a capillary tube (1.6 mm external diameter, 1.3 mm internal diameter) soldered on a golden pad all along the silicon position. The pad was connected to the electric ground. On Figure 64 a schematic of the foreseen cooling system and of the cooling structure implemented on the read-out PCB is shown.

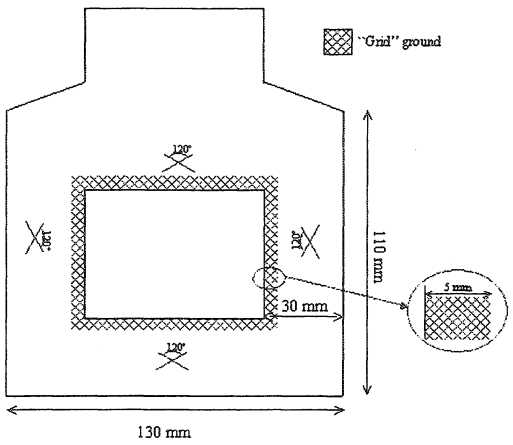

Figure 64: Schematic of the board for cooling test

The board was inserted in a vacuum tight cryostat and operated at a pressure ~10^6 mbar.

Studying the dependence of the temperature as function of the liquid nitrogen flux, we found that it is possible to obtain a uniform temperature distribution on the silicon with a flux of ~250 l/hour, in the limit of 10 K.

If we consider the position of silicon detector in COMPASS we can identify two regions: the target region, immediately in the neighborhoods of the target, and the spectrometer region, the main part of the detector.

The use of detectors in the two regions imposes different requirements to the support structure and to the cryostat. In particular in the spectrometer region, to minimize the effect of multiple scattering, materials with a very large radiation length have to be used, while in the target region there is no similar requirement, since the angular spread of the beam is so small that it is enough to minimize the quantity of material only in a small area along the beam direction.

From that follows the necessity to foresee two different types of cryostat for the two regions.

At the present moment, the cryostat for the target region had been realized. It consists of a stainless steel box (30×30×8 cm^3). On the two sides on the beam direction are bolted two stainless steel plates of 1 mm thickness, with a circular window of 86 mm diameter, centered on the beam axis. The windows are made of aluminised Mylar glued on the metallic structure

with Araldite 2011. On the lateral sides of the cryostat there are flanges for services and for the signal cabling.

Inside the cryostat 4 pins consent to position two silicon detectors, mounted on a Stesalit structure with a precision of ~10 μm. Figure 65 shows the cryostat with a silicon detector. This cryostat was used as support for the silicon detectors operating at room temperature used during the 2001 COMPASS data run.

For the cryostat on the spectrometer region, a prototype made of Rohacell foam and covered with aluminised Mylar was prepared. Further optimisations are ongoing.

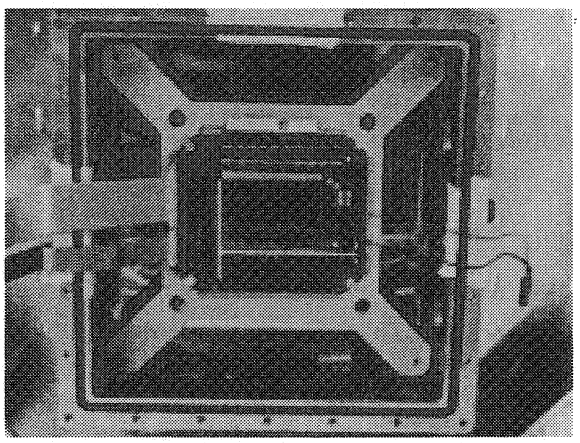

Figure 65: Front view of silicon detector in the cryostat

References of Section 7

[1] The COMPASS Collaboration, COMPASS proposal, CERN/SPSLC96-14, SPSC/P297 (Geneva, March 1996); CERN/SPSLC 96-30(Geneva, May 1996)

[2] Jahresbericht 2000 Beschleuinigerlaboratorium München,

[3] APV25 user manual http://www.te.rl.ac.uk/med_old/

PART II

Proposal for large cryogenic tracker development, and for the extension of the present projects of RD39

K. Borer, S. Janos and K. Pretzl
Laboratorium für Hochenergiephysik der Universität Bern, Sidlerstarsse 5, CH-3012 Bern, Switzerland

Wei Chen and Zheng Li*
Brookhaven National Laboratory, Upton, NY 11973-5000, USA

C. da Viá and V. Granata
Brunel University, Uxbridge, Middlesex UB8 3PH, UK

L. Casagrande, P. Collins, S. Grohmann, E. Heijne, C. Lourenço, T.O. Niinikoski*, B. Perea Solano, V.G. Palmieri and P. Sonderegger
CERN, CH-1211 Geneva, Switzerland

E. Borchi, M. Bruzzi, S. Lagomarsino, D. Menichelli, S. Pini, S. Sciortino
Dipartimento di Energetica, Universitá di Firenze, I-50139 Firenze, Italy

W. Bell, S.R.H. Devine, V. O'Shea, G. Ruggiero and K. Smith
Department of Physics and Astronomy, University of Glasgow, Glasgow G12 8QQ, UK

P. Berglund
Low Temperature Laboratory, Helsinki University of Technology, FI-02150 Espoo, Finland

Jaakko Härkönen and Eija Tuominen
Helsinki Institute of Physics, FI-00014 University of Helsinki, Finland

W. de Boer, A. Dierlamm, E. Grigoriev, F. Hauler and L. Jungermann
IEKP University of Karlsruhe, D-76128 Karlsruhe, Germany

M. Abreu, P. Rato Mendes and P. Sousa
LIP, Av. E. Garcia, P-1000 Lisbon, Portugal

K. Piotrzkowski, J.-S. Graulich
Universite Catholique de Louvain, HEP Lab., Chemin du Cyclotron 2, B-1348 Louvain-la-Neuve, Belgium

V. Cindro, M. Mikuz and M. Zavrtanik
Jozef Stefan Institute, Exp. Particle Physics Dep., PO Box 3000, 1001 Ljubljana, Slovenia

Rita De Masi and S. Paul
Physik Department E18, Technische Universität München, D-85748 Garching, Germany

S. Buontempo, N. D'Ambrosio and S. Pagano
Dipartimento di Fisica, Universitá "Federico II" and INFN, I-80125 Napoli, Italy

Reino Laiho, Leonid Vlasenko and Marina Vlasenko
Wihuri Physical Laboratory, University of Turku, FIN-20014 Turku, Finland

V. Eremin and E. Verbitskaya
Ioffe Physico-Technical Institute, Russian Academy of Sciences, St. Petersburg 194021, Russia

Jozsef Molnar, András Fenyvesi (under discussion)
ATOMKI, Debrecen, Hungary

---

* co-spokesperson

8 MAIN GOALS OF RD39 IN THE FUTURE

After a 3 to 5 years of operation at the full design luminosity and energy of the LHC, there may appear need for upgrading one or the other, if not both. The energy upgrade looks less likely at the moment, because the dipole magnets of LHC are already pushed quite close to limit of affordable technology. A luminosity increase of the LHC by a factor of 10 could be achieved by a combination of three factors [1]:

- Increasing the number of protons per bunch to the beam-beam limit of $1.7 \cdot 10^{11}$ instead of the nominal $1.05 \cdot 10^{11}$. Gain: factor 2.6.
- Decreasing the bunch spacing. A bunch spacing of 12.5 ns is suggested as working hypothesis, giving a factor 2 gain in luminosity.
- Decreasing the beta-function from the present 0.5 m. This will require an upgrade of machine optics around the interaction points, and could also yield a factor of about 2.

If the detector performance would permit, even shorter bunch spacing would be easier to accomplish than the two other factors of improvement. The LHC machine would prefer a spacing that is a multiple of 5 ns.

If the mass reach were taken as the main criterion for judging the physics interest of the upgrade options, the energy upgrade would be more powerful. For physics involving somewhat smaller masses, the luminosity upgrade could be more powerful *provided that the detector performance can be maintained* [2]. The most severely affected part of the large detectors is the tracker, and it is clear that the luminosity upgrade path would depend on the opportunities offered by the radiation hardness and speed of the new tracker detectors under development now.

The main goal of the presently proposed R&D program is the proof of the feasibility of large cryogenic trackers for LHC after the upgrade of its luminosity. For this goal, the planned program will involve the design, construction and tests of prototype detector modules with very low mass, satisfying the requirements of 10 times improved radiation hardness, and speed compatible with 5 ns bunch crossing interval. System and engineering aspects will also be covered to the extent that the resources will permit. These will be outlined in Section 9, whereas the extension of the present projects will be discussed in Section 10.

The present projects of RD39 have yielded important data and theoretical understanding for the application of silicon detectors in the environment with high fluence, and they have paved the way towards the realization of tracker detectors for the LHC experiments after the luminosity upgrade. Other applications, before the major luminosity upgrade of LHC, may be found in the very forward regions of ATLAS and CMS at nominal luminosity.

In the Device Physics and Basic Research projects, the quantitative understanding of the Lazarus effect was achieved, and this led to several new proposals for further experimentation and for new device structures. The extension of these projects will serve as the design basis for extremely radiation-hard segmented sensors for high-luminosity and high-speed applications. These will be discussed in the Sections 10.1. and 10.2.

While the main goals of the present common projects have been reached, notably for RD39/NA60, important development work is still required for the RD39/TOTEM and the RD39/COMPASS projects, before the prototyping work can be considered completed. During

the construction phase some help will also be required, while the main manpower should be obtained from the experiments directly in this and the subsequent operation phases. These projects will be detailed in the Sections 10.3, 10.4 and 10.5.

The future resource plans of RD39 will be in described in Section 11, including the scheduling, the manpower and financial resources, and the requirements of space and technical support at CERN. The facilities and beam time for detector and irradiation tests are also briefly discussed.

References of Section 8

[1] L. Casagrande et al., Part *Tracker* in the document *Physics Potential and Experimental Challenges of the LHC Luminosity Upgrade*, Conveners: F. Gianotti, M. Mangano and J. Virdee, (to be published as a CERN Report, 2002).

[2] G. Azuelos et al., "Impact of Energy and Luminosity upgrades at LHC on the Physics program of ATLAS", ATL-COM-PHYS-2001-033.

9 CONCEPTUAL DESIGN OF TRACKER DETECTORS FOR SUPER LHC

A new project will be shaped for the needs of the future high-luminosity hadron colliders. This project has the goal of an all-cryogenic tracker with optimum performance at the luminosity of 10^{35} $cm^{-2}s^{-1}$, surviving the integrated luminosity of 2500 fb^{-1} which has been taken as a basis for the upgrade of LHC. In addition to the sensor, readout and module design aspects, the project will address the engineering problems of the tracker system, including:

- electromagnetic interference control
- mechanical supports and their thermoelastic behaviour
- alignment
- cooling and thermal design
- power feed.

For practical reasons it may be convenient, at a later stage, to divide the work into Pixel and Microstrip projects which address the inmost and outermost layers of the tracker. In the intermediate region of the tracker the optimum segmentation may call for mini-microstrips or macro-pixels, which reduce the occupancy to an acceptable level; in this case an additional project may need to be set up.

Some of the engineering tasks could also be spun off into separate projects at a later stage, preferably as common projects with one or more of the LHC experiments.

The conceptual design of the cryogenic tracker will be handled in the beginning in an integrated manner, so that none of the main design problems will be dissociated from the whole. This principle has developed in the course of the design experience of the present LHC trackers. The prerequisite for such an approach is a coherent project team where all required scientific and engineering skills are present. We believe that the RD39 Collaboration has the required skills in all of the main domains, with the exception of DSM CMOS ASIC design where collaboration with other R&D efforts is being sought.

9.1 Sensors for trackers at the upgraded LHC

The cryogenic microstrip and pixel sensor design will be based on the requirements set by the luminosity and fluence of the LHC after its projected major upgrade, as discussed above. The bunch crossing interval is assumed to be 12.5 ns or lower, and our goal will be to make the sensors compatible with the bunch crossing interval of 5 ns, because the charge transit time in 300 μm thick silicon sensor is in this range at 130 K, even without strong overdepletion. Thinner detectors, however, will also be considered, because of the benefits entailing for the charge transit time, track and two-track resolution, occupancy, and for the tracker thickness. The signal-to noise ratio would not necessarily deteriorate from the present designs, because of the lower noise of the cold readout electronics, because of the higher signal due to the higher mobility, and because the current noise of the sensor is absent.

The sensor design will be based on the results of the Device Physics project, to be discussed in Section 10.2. The following are presently being considered for fluences above $2 \cdot 10^{15}$ cm^{-2} of charged hadrons:

- Forward biased sensors
- p^+np^+ symmetric sensors
- Current injected sensors

For fluences up to this value oxygenation does not seem to be necessary, and the resistivity of the silicon is not of major importance at low temperatures. We shall nevertheless pursue studies of the various material types in the framework of our Basic Research project, together with the annealing and defect identification work.

Other factors, which are important for the cost of the sensors, are related with the processing. We have shown that microstrip sensors can be produced using two or three masks only, and because the number of mask steps is a determining factor, a substantial cost reduction could be obtained. If the material characteristics can also be relaxed so that 8" wafers could be used, a very substantial advantage could follow from the simplified assembly procedure of large-surface strip modules.

9.2 DSM CMOS readout circuit development

Among the key performance questions at very high luminosity are the speed and signal-to-noise ratio of the front-end on-detector electronics. Because these electronic circuits will have to operate close to 130 K temperature, they can profit from the cryoacceleration and from the potentially lower noise available at that temperature. The 0.25 μm CMOS circuits work well at low temperatures, as was discussed in Sections 4 and 7. Both analog and digital circuits are operating faster, and the noise figure of the preamplifier theoretically reaches the minimum value at about 110 K, if the circuit design is optimized. The optimized design of the DSM CMOS circuits, however, require substantial development work and access to a facility which has the required design rules for a wide temperature range. This work could happen in collaboration with the CERN Microelectronics group. Collaboration with ESA might also be of interest, because they already have the design rules and experience in this domain.

As the initial current signal is much higher (in comparison with a sensor at room temperature) because of the increased carrier mobility, and because the charge transit time is shorter, it is necessary to optimize the preamplifier and shaper bandwidths for the conditions of cryogenic detectors.

If CERN decides to pursue the design and development of monolithic pixel detectors, a project in collaboration with RD39 might be of interest because some of the proposed schemes rely on the advantages offered by low temperatures.

In the design of the high-speed low-noise circuits the control of the electromagnetic interferences should be taken into account. It would be preferable to design the front-end chip in such a way that decoupling of the power supply lines would be already achieved on-chip for the fastest spectral part of the signals involved. The remainder of the decoupling should take place very near to the front-end chip. Other parasitic and interference signal control features should still be designed further upstream of the detector modules, and in particular at the feedthroughs to the cryogenic vacuum and in the power supplies. Designs with balanced lines should be preferred against asymmetric lines.

9.3 Module design and module assembly tooling

The design of cryogenic microstrip and pixel modules for the very high luminosity trackers will be based on the experience gained in the common projects with NA60, TOTEM and COMPASS. The microtube cooling will be applied in the microstrip modules, while for the

pixel modules the conceptual design using microtube cooling is yet to be developed. The same pixel module design, however, can be used for both the monolithic and for the bump-bonded pixel devices, because the sensor power dissipation is negligible in both cases.

The assembly tooling in the prototyping phase of the microstrip modules will follow the development made for the TOTEM Roman pot modules. In the module design it will be taken into account that the production assembly should be preferably carried out using pick-and-place robots or equivalent automated machinery.

The mechanical prototype modules will be irradiated up to the relevant fluence at low temperatures, and they will be subjected to temperature cycling and tests of mechanical resistance and integrity. A low-temperature irradiation set-up is presently being designed, and it is expected to be available in July 2002.

9.4 Other engineering problems

Vacuum

Because the large trackers in LHC use a superconducting solenoid magnet, it would be attractive to combine its cryogenic vacuum with that of the tracker. The solenoid cavity must be closed by end flanges, which connect to the outer shell of the solenoid vacuum chamber and to the beam pipe. The inmost pixel tracker removal must be made possible, together with the beam pipe.

The vacuum feedthroughs are an important technical problem. We consider the possibility of extending the vacuum along suitably sized pipes to outside the magnetic field of the detector, so that the feedthroughs can be equipped with electromagnetic interference control (EMI) filters using ferrite materials, which provide the best high-frequency barrier against interferences.

The beam pipe inside the cryogenic vacuum can be very thin.

Supports and alignment

The supports between the vacuum chamber at room temperature and the cold mass of the detector must be thermally isolating, and they must provide sufficient mechanical stability. These conflicting requirements can be easily solved in that same way as in superconducting magnet systems, with the exception that the load carrying capacity requirement is very much smaller.

The supports of the individual layers of the tracker, and the attachment of the modules onto the support structures, must be designed so that the thermal dilatation is adequately taken into account. Such a design is best based on the use of zero-dilatation CFC.

The following items apply to all supporting elements, whether isothermal or under thermal gradient:

- The thermoelastic behaviour of all mechanical supports must be understood;
- Control of the alignment before and after tracker cooldown, using optical, electrical and mechanical methods (to be evaluated);
- Tracker position control using a hydraulic system, based on an on-line precision measurement of a few coordinates (method to be chosen).

Cooling

The microstrip tracker could typically cover a surface of about 400 m^2, and feature average segmentation similar to those of ATLAS and CMS, i.e. one strip covering about 10^{-5} m^2. The total power dissipation is then about 100 kW for the $4 \cdot 10^7$ readout channels of these strips, basing on the power/channel of 2.3 mW for the APV25 chip, and taking into account other minor sources of heat. These additional heat sources are:

- Thermal radiation (< 1 kW if well shielded by superisolation)
- Heat conduction along supports, cables and fibers (typically a few hundred W)
- Sensor power (total of 40 W from current injection)

The primary source of cooling could operate somewhat below 100 K and use nitrogen as working fluid. The modules should be cooled using two-phase flow of suitable cryogenic coolants such as Ar, LN_2 or CH_4, in a secondary circuit. The choice of coolant depends on the choice of the sensors and on the thermal design of the modules. The secondary circuit should be driven by circulation pumps similar to those used in the LN_2 cooling loops of the LAr calorimeter of ATLAS.

The thermal and thermoelastic design of the modules and of the cooling circuitry will be developed and tested during the TOTEM prototyping.

The thermal load and the cooling system of the pixel detector would be similar to that of the microstrip detector. The thermal and thermoelastic design of the pixel modules should be started at an early stage.

Services

Two-phase cooling of 100 kW can be made with a fairly low mass contribution to the thickness of the tracker, whereas the transport of the 100 kW electrical power at a low voltage to the modules requires a much larger contribution to the thickness. We therefore propose to study improved low-voltage (LV) power transport systems, in view of reducing the tracker mass substantially from what is used in the present LHC trackers.

For the power feed using normal conductors, one usually considers lower than 6 A/mm^2 current density, whereas technical superconductors can carry kA/mm^2 currents. We therefore consider using HTC or ordinary superconducting wires for low-voltage power feed of the readout electronics. In addition to the benefits of low mass and low power dissipation, also the absence of voltage drop is an important factor, entailing excellent control of the voltages of the readout circuits.

The high-voltage (HV) power feeds can be conventional, because the leakage currents in the sensors are very small at 130 K, and if current injection is used, the currents drawn are in the range of 20 nA/cm^2 or less than 10 μA/module. The HV cables therefore need no cooling. The HV feedthroughs, however, should be filtered, as well as the LV lines.

The optical fibers for data and clock transmission may need to be tested for their radiation hardness at low temperatures.

Electromagnetic interference control

The metallic vacuum enclosure makes a Faraday cage, which provides excellent EMI control, if the instrumentation wires are filtered at the point of entry into the vacuum space.

While filters for multipin vacuum feedthroughs are already available commercially, their cost of about 30 CHF/pin may be prohibitive, and may require simplification and optimization of the filter designs. These filters can use ferrites if they are placed outside the magnetic fields of the tracker. If the superconducting LV power transmission lines are extended up to the power racks of the modules, the most efficient power supply interference rejection can be achieved, and the voltages of the modules do not need additional lines of their measurement, eliminating the need for their filters as well.

The EMI problem in a high magnetic field between cryogenic modules, and across the channels of an individual module, is slightly alleviated at low temperatures by the higher electrical conductivity of copper and aluminium. Otherwise the problems are similar to those of modules close to room temperature, and the main methods of decoupling involve RC filters, balanced lines, shields against displacement currents and radiated interference, and absorbing materials such as carbon composites and sintered metals for radiated power and for filters, among others. Some of the special materials should be examined for their application at low temperatures and under intense radiation. Ferrite materials are unfortunately precluded because of the high magnetic field of the tracker.

Among the system aspects, the higher bunch crossing frequency deserves some thoughts. The present crossing frequency of 40 MHz forces the passband of the preamplifiers and shapers to be centered on this frequency band, in which the natural frequencies of a sizable tracker are also accumulating. The natural damping around 40 MHz is small unless lumped resistive elements are inserted in the metallic structures. Moreover, the clock frequency was also selected to be 40 MHz. The susceptibility to interference is therefore maximized by these design choices.

If the bunch crossing frequency is 200 MHz, the natural damping in resonant structures is much higher, the RC filters will be smaller, and the emission control can be made much more effective. It would be preferable to set the clock frequency about 10 times higher than the bunch crossing frequency of 200 MHz, and the data should be transmitted using 10 GHz optical links.

Such high-speed optical fiber data communication circuits should be examined at low temperatures and in high radiation field. The cryoaccelerated DSM CMOS circuits have the required speed, as was discussed in Sections 4 and 7.

10 EXTENSION OF THE PRESENT PROJECTS

10.1 Device Physics

The investigations of Si detectors below room temperature gave several new results, which were overviewed in Section 2. They are important for the understanding of the physics of radiolytic defect formation, and for the operation of detectors in heavy radiation environment. They are also important for the design of the next generation of radiation hard detectors for the high luminosity colliders. The results clearly show that:

1. The dominant temperature-related features in irradiated detectors are very sensitive to the concentrations of deep levels. The features cannot be explained by these concentrations as determined from the results of defect studies at room temperature. About 10 – 100 times higher radiation yields are expected. This is one of the main points for the future Device Physics plan, and will need common investigations with other groups (experienced in DLTS, in EPR, and in the studies of the interaction of particles with crystals).
2. Investigation of the temperature-dependent effects in irradiated detectors shows that the bulk generation current is one of the key factors controlling the electric field distribution in the detector, and hence the current influences the detector quality. In practice this current can be easily controlled by the injection of additional free carriers by light or via a p/n junction. Therefore the bulk current can be considered as a parameter for optimizing the sensor performance, similar to the temperature and to the applied bias voltage. The operation at a low temperature is optimal for the realization of this approach.
3. The approach of detector operation with current injection was verified in forward biased mode, and by electric field manipulation with light-injected current. A numerical model of the current injection mode was developed. The model shows that this mode eliminates easily the problem of the collapse of the SCR thickness after irradiation, and is a new way to survive a very high fluence. The further development of this approach is one of the major goals for the future RD39 plan.

The Device Physics project will address the above key issues in the device physics of silicon sensors for the fluence range beyond 10^{15} cm^{-2}. The following itemized list gives in some detail the work program, which can be carried out mainly outside CERN.

A. Radiation hard detectors based on low temperature effects in irradiated silicon

A.1 Detectors based on electric field manipulation by current injection (CI)
- Current injection by light for electric field adjustment;
- Current injection through p-n junction;
- Detectors operated in Space Charge Limited Current mode.

A.2 Edgeless detectors (work started already for TOTEM, see section 5)

A.3 Resistor type detectors (symmetric structures p^+np^+, initial work reported in [1])

A.4 Avalanche MIP detectors (AMD) and avalanche photodetectors at low temperatures
- Pad detectors
- Monolithic array detectors

A.5 Thin detectors

B. Radiation hard detector investigation and development of related experimental techniques

B.1 Physics of edge current (theoretical and experimental)

B.2 Physics of CI detector operation (theoretical)

B.3 Charge limited current in irradiated silicon p-n junctions

- Detector polarization effect;
- Electric field manipulation by current injection.

B.4 Development of high time resolution TCT for electric field studies in segmented devices (equipment construction started already; the goal is to achieve < 50 ps time resolution and < 5 μm position resolution at saturated drift velocity)

C. Essential device physics related investigations

C.1 Free carrier trapping at low temperatures by charged deep traps

C.2 Free carrier trapping by neutral deep traps

C.3 Mobility and Lorenz angle in silicon at low temperature

C.4 Electric field distortion under free carriers in the detector space charge region

D. Technology of detectors operated at low temperatures

D.1 Technology of edgeless detectors (edge processing techniques; already started)

D.2 Detector processing using a small number of masks (already started)

D.3 Radiation technology for defect engineering (using a suitable radiation source for creating favourable defects and a high resistivity)

D.4 Impurity-engineered detectors operating at low temperatures (oxygenated materials)

D.5 Ultra radiation-hard advanced detector materials at low temperatures (epitaxial SiC materials for pixel devices, optimized for MIP signal detection)

10.2 Basic research

CCE measurements

CCE characterization of diodes at different temperatures

Study of CCE of segmented devices at cryogenic T

Defect studies

Continuation of studies of defect formation at cryogenic temperature including:

DLTS and EPR on line

EPR measurements

Deep level characterization by

- DLTS
- TCT
- EPR using magnetic resonance signal
- EPR using photoconductivity

Defect formation (annealing) at low temperatures

Radiation-assisted shallow level removal

DLTS – TSC analyses (new study)

In the next year the Florence team plans to further investigate the role of cluster defects in affecting the silicon detector performance. In particular, the evolution of the defect clusters contribution to the degradation of the detector performance will be investigated as a function of the fluence. The results obtained after irradiation with fast neutrons will be compared with those after proton and gamma irradiation, which should produce a lower fraction of extended defects in the semiconductor bulk.

Thermally Stimulated Current studies will be performed in the low-temperature range 10-130 K by means of an original system developed by the Florence group [2, 3]. This study is quite important to determine the shallow levels contribution to the charge collection efficiency of the irradiated devices operating at cryogenic temperatures. It is well known, in fact, that operating the Si detector at temperatures of the order of 130 K provides the frozen out of the deeper radiation-induced levels, mainly associated to divacancy related defects, which activates at higher temperatures. This brings to a beneficial effect in the charge collection efficiency of the device, as trapping-detrapping processes at deep levels become negligible at this temperature. Nonetheless, trapping-detrapping mechanisms due to shallow levels, which activate at temperatures lower than 130 K, can still significantly affect the charge collection efficiency of the device. A systematic study will be carried out to determine the trap parameters (energy level, cross section and trap concentration) of the radiation induced and native shallow levels. The emission and trapping coefficients will be evaluated to understand the influence of these traps in the performance of the silicon detector.

Cryogenic performance of Epitaxial Silicon Carbide Detectors in a Radiation Environment

The potential of wide band-gap semiconductors for radiation detection and dosimetry is now widely recognised. In particular, the outstanding optoelectronic properties of materials as diamond and silicon carbide have recently stimulated an increasing interest towards particle detection applications [4 - 7]. Silicon Carbide, in its 4H polytypic form, is characterised by electronic properties lying in between silicon and diamond, as shown in Table 9.

Property	Diamond	4H SiC	Si
Bandgap [eV]	5.5	3.3	1.12
Breakdown Field [V/cm]	10^7	$4 \cdot 10^6$	$3 \cdot 10^5$
Electron mobility [cm^2/Vs]	1800	800	1450
Hole mobility [cm^2/Vs]	1200	115	450
Saturation velocity [cm/s]	$2.2 \cdot 10^7$	$2 \cdot 10^7$	$0.8 \cdot 10^7$
Effective atomic number Z_{eff}	6	~10	14
Dielectric constant ε_r	5.7	9.7	11.9
e-h creation energy [eV]	13	8.4	3.6
minority carrier lifetime [s]	10^{-9}	$5 \cdot 10^{-7}$	$2.5 \cdot 10^{-3}$
Wigner Energy [eV]	43	25	13-20

Table 9: Properties of diamond, 4H SiC and Si.

Recently, Schottky diodes made with epitaxial n-type 4H SiC have proved to be efficient α-particle detectors [6] and dosimeters [7]. The devices used in this study are produced using epitaxial wafers purchased from CREE Research, consisting in a n-type, 4H-SiC epitaxial layer, 30 μm thick, grown on an n^+-type substrate of 4H-SiC (thickness: ~300μm). The net doping concentration in the epitaxial layer, due to aluminum and nitrogen compensation, is 10^{14}-10^{15} cm^{-3}. A Ti/Au thin film has been evaporated onto the backside of the wafer to form a large area backside low-resistance ohmic contact. Then the wafer has been patterned using standard photolithography and immediately before the deposition of the Schottky contact has been de-oxidized using an Ar-ion etch. Lift off has been used to pattern a circular Au (1000 Å) contact of 2 mm diameter.

Due to the high bandgap, the leakage current of the device is in the range 0.1 – 1 pA up to 1000 V. The high lattice quality of the epitaxial layer is characterized by a low concentration of native impurities [8]. This should provide a negligible contribution of trapping and recombination processes to the charge collection efficiency of the detector, giving rise also to a very high spatial uniformity of the device. Due to the high crystalline quality, these samples feature a diffusion length of the order of 10 μm [7] for the minority carriers. As a consequence, a significant contribution to the charge collection efficiency of the device in partial depletion conditions is due to the diffusion of the minority carriers in the neutral region of the epitaxial layer. For the same reason, a SiC epitaxial dosimeter shows sensitivity comparable to standard Si dosimeters operated unbiased [9]. A 100% charge collection efficiency (CCE) has been measured at room temperature with 5.48 MeV α-particles from an ^{241}Am source [7]. CCE measurements performed with a ^{90}Sr β-source are now in progress by the Florence group. Preliminary radiation hardness studies at room temperature have been performed by the group of Bologna after irradiation with 24 GeV/c protons at a fluence of 9.37×10^{13} cm^{-2}. The radiation resistance of this material, as compared to silicon, has been assessed: no changes in the depletion voltage and leakage current have been observed after irradiation, moreover a 100% CCE has been measured with the irradiated devices. As a consequence of the irradiation, a lowering of the diffusion length has been observed approximately to 1 μm. A major drawback in the application of these devices as particle detectors is the high doping level of the epitaxial layer, causing full depletion voltages at room temperature of the order of 400 V or higher. In the framework of this collaboration, our interest will be focused on the study of the performance of these devices in the cryogenic temperature region. We shall investigate the charge collection efficiency of the Schottky barrier epitaxial SiC detectors to minimum ionizing particles as a function of the voltage in the temperature range 100-300 K, after irradiation with different particles and fluences. The aim is to investigate the role of the operating temperature in controlling the depletion voltage of the device before and after irradiation. A complete study of the radiation-induced defects will be carried out, using Thermally Stimulated Current and Deep Level Transient Spectroscopy, by the groups of Florence and Bologna, to investigate if trapping-recombination processes can influence the detector performances in this temperature range.

Hall mobility and Lorentz angle

The experimental studies will be continued on sensors with higher radiation doses. The experimental and theoretical work will be pursued for understanding the large Hall scattering factor for electrons at 78 K.

10.3 RD39/NA60

The construction of the Beamscope trackers for the proton and lead ion primary beams was completed, and the persons who assumed the main responsibilities in the project are now moving to new duties. The experiment requires, however, technical support and training for new persons who will operate and maintain these detectors. RD39 therefore foresees the extension of the common project at the level of technical support and training.

10.4 RD39/TOTEM

The TOTEM experiment has decided to use cryogenic silicon microstrip detectors in their Roman pots, which will be mounted in the LHC beam pipe around the CMS interaction point. A major effort was started for the development of the autonomous cooling systems, and for the silicon detector modules, which can operate in the environment of the LHC beam tunnel. This development work, described in Section 6, is proposed to go on in the framework of the common project, up to the tests of the final prototype Roman pot system.

The mechanical parts of the vacuum chamber, the position controls of the pots, and the design aspects related with LHC beam impedance and LHC vacuum system, will be covered by TOTEM together with the LHC machine groups, although RD39 will be involved in those aspects which deal with the precision positioning of the detector modules inside the pots, with the beam window, and with the bakeout procedure of the vacuum chambers.

It is expected that support and help will be obtained from CMS for the development of the APV25 readout electronics of the microstrip modules.

The possibility of equipping the pots nearest to the interaction point with pixel sensors will be discussed with TOTEM. Preliminary work is underway in order to evaluate the sizes and shapes of the required sensors, and to decide which DSM readout chip would best satisfy the needs of the physics program.

In 2002 two additional cooling systems are scheduled for building and testing. The first will serve for irradiation studies in the PS irradiation facility; it is expected that the equipment will become available in July 2002. The second is designed for use in test beams, and will be equipped for the cooling of the prototype electrical modules. This is scheduled for October 2002, and it will also serve as a prototype for the cooling systems of the TOTEM Roman pots.

10.5 RD39/COMPASS

The COMPASS tracker is still in the prototyping phase for the microstrip module design and for the cryogenic systems for the two main parts after the target and near the spectrometer magnet. It is proposed that RD39 will increase its involvement in these, using the experience and knowhow gained in the RD39/TOTEM and RD39/NA60 projects.

The experience and knowhow of COMPASS in the operation of APV25 at low temperatures, on the other hand, will be valuable for the RD39/TOTEM project.

References of Section 10

[1] K. Borer et al., Nucl. Instr. and Meth. A **462** (2001) 474-483.

[2] E.Borchi, M.Bruzzi, S.Pirollo, S.Sciortino, "A method of TSC analysis of shallow levels applied to silicon", *Journal of Physics D: Applied Physics*, vol. **31**, (1998), L93-L96

[3] E. Borchi, M. Bruzzi, Z. Li, S. Pirollo, "Thermally Stimulated Currents analysis of the shallow levels in irradiated silicon detectors", *Journal of Physics D: Applied Physics* vol. **33**, 3, (2000), p.299-304.

[4] The RD42 Collaboration, "Review of development of diamond radiation sensors", Nucl. Instr. and Meth. A 434, (1999), pp. 131-145.

[5] T. Dubbs et al. "Development of radiation hard materials for microstrip detectors", IEEE Trans. Nucl. Sci., vol. 46, (1999), pp. 839-843.

[6] F.Nava P. Vanni, C. Lanzieri, C. Canali, "Epitaxial silicon carbide charge particle detectors", Nucl. Instr. Meth. A 437 , (1999), pp. 354-358.

[7] M. Bruzzi, F. Nava, S. Russo, S. Sciortino, P. Vanni, "Characterisation of silicon carbide detectors response to electron and photon irradiation", Diam. Rel. Mat. , vol. 10, (2001), pp. 657-661.

[8] A. Castaldini, A. Cavallini, L. Polenta, F. Nava, C. Canali, C. Lanzieri, Defective state analysis in silicon carbide, ASDAM 2000. Conference Proceedings. Third International EuroConference on Advanced Semiconductor Devices and Microsystems IEEE, Piscataway, NJ, USA, vol. 481, 2000, pp. 157-60.

[9] M. Bruzzi, F. Nava, S. Pini, S. Russo, "High Quality SiC Applications in Radiation Dosimetry", *Applied Surface Science*, Vol. 184/1-4 (2001), 425-430.

11 REQUEST FOR EXTENSION

11.1 Organization

The present organization of RD39 has been decided by the Institute Board of the Collaboration, where each Institute of RD39 has one vote. The constitutive rules of the collaboration have been agreed by the Institute Board, and they are recorded in the Minutes of the collaboration meetings. The main agreements are:

- Appointment of Co-spokespersons
- The Publication Policy agreement
- Approval of the breakdown of the approved program into Projects
- Appointment of Project Leaders
- Agreement on Team account and on its use

The main responsibility of the Institute Board is to oversee that the collaboration works coherently towards the goals approved by the LHCC and the Research Board of CERN, and that the organization and resources correctly reflect the planned work program.

The Co-spokespersons and the Project Leaders form an Executive Board, which discusses and decides on future projects prior to the final approval by the Institute Board. A unanimous support by the members of the Executive Board is required for the approval of a new project. The Executive Board also prepares some of the matters to be decided by the Collaboration meeting and by the Institute Board.

The RD39 Collaboration has appointed two Co-spokespersons: Zheng Li (BNL) and Tapio Niinikoski (CERN). They are willing to continue managing the collaboration.

The execution of the RD39 program is carried out presently in five projects, which are led by the following project leaders:

- Device Physics: Vladimir Eremin, Ioffe PTI
- Basic Research: Cinzia Da Viá, Brunel
- RD39/NA60: Luca Casagrande, CERN
- RD39/TOTEM: Tapio Niinikoski, CERN (*ad interim*)
- RD39/COMPASS: Rita de Masi, Munich

A new project is being prepared for Large Cryogenic Trackers (Section 9), and its approval is submitted to the LHCC in the present request.

In the future the Institute Board will continue to decide upon the above matters. It is presently under discussion that the Institute Board will elect also its Chairman, who will prepare the possible future elections and chair the Institute Board meetings.

The proposed enlarged scope and longer time scale for the RD39 could make it necessary and profitable to produce a Memorandum of Understanding (MoU) for the collaborating institutes. As the collaboration is executing several projects in common with approved experiments, and because the work is R&D-oriented, the MoU would have to be rather specific, and in some areas different from the usual formula for experiments at CERN. Some of the present agreements and rules could be included in the MoU, and the remainder could be appended to it.

11.2 Schedule

The following items should serve as a basis of discussions:

- Time scale for the proposed program: 6 years, with milestones defined by LHCC for each project, basing on proposals from the projects as given below
- Status reports as requested by LHCC.

The short-term (12 month) milestones for each project can be defined with some certainty, while the medium- and long-term milestones are better defined as topical Reviews at this point. This follows from the need of reorienting and refocusing the research and development according to the results obtained. The Collaboration has discussed the following provisional plan for the milestones and reviews:

- Device Physics: First Current Injected devices tested (6 months); Review of Current Injection schemes (1.5 years); Review of segmented device structures (2 years).
- Basic Research: Review of defect yield and annealing reactions at low temperatures (2 years)
- RD39/NA60: Training completed for the new beamscope team in NA60 (6 months)
- RD39/TOTEM: Low-temperature irradiation set-up ready (6 months); beam test set-up ready (12 months); TOTEM TDR (9 months); Cooling system review (12 months); Thermoelastic design review of irradiated TOTEM modules (1.5 years); Electrical module review (2 years)
- RD39/COMPASS: Cryostat review (6 months); module design review (12 months)
- Large Cryogenic Trackers: Review of requirements (6 months); review of the conceptual design of microstrip modules (12 months); review of pixel module designs (2 years)

Major milestones:

- Review of best radiation-hard sensor technologies (after 3 years)
- Decisions on the shortest possible bunch crossing interval, and on the front-end electronics (after 4 years)
- Review of SLHC tracking (after 6 years)

11.3 Manpower

Most of the present Institutes plan to continue their activities in RD39, and the following new Institutes are considering joining the RD39 Collaboration:

- Louvain-la-Neuve (Team led by Krzysztof Piotrzkowski)
- Helsinki Institute of Physics (Team led by Jaakko Härkönen)
- Wihuri Physical Laboratory, University of Turku (Team led by Reino Laiho)
- ATOMKI, Debrecen, Hungary (not confirmed yet)

The new full list of Institutes and their Team members is given above Section 8.

The manpower resources required for carrying out the approved program are drawn from the RD39 institutes and from the experiments with which there is a common project:

- Common projects: manpower drawn mainly from the approved experiments
- Basic research and Device Physics: manpower mainly from RD39 Institutes
- Large Cryogenic Trackers: manpower from RD39 Institutes and from LHC experiments

11.4 Financial resources

Existing CCE and TCT equipment will be used at CERN, and the Team account will be used for covering the rental costs of equipment from the EP Electronics pool. The materials costs will be covered directly by the participating institutes of each active project. Some minor operating costs, such as minor stores withdrawals, printing of reports etc., will be covered by the common Team account, following the agreed rules.

The new equipment at CERN should be funded as follows:

- Common projects: funds mainly via RD39 institutes during prototyping, via experiments for production and operation;
- Basic research and Device Physics: to be funded by RD39 institutes, as in the past;
- Trackers for Super LHC: funding via RD39 and via LHC experiments; details to be agreed with the experiments.

Team account: Use and contributions to be redefined in MoU or in an appendix of MoU.

11.5 Requirements of space at CERN

RD39 presently uses the following space at CERN:

- Small space (about 10 m^2) in ATT-SC laboratory in B602, with a laminar flow bench, microscope and small manual wire bonder
- Cryolab of B151: about 30 m^2

The following space is requested in the year 2002 and onwards:

- In the Cryolab the presently used space is sufficient.
- A semi-clean lab in the SSD section (B28): this would replace the presently used lab space in B602.
- An office is requested in B28 near the future semi-clean space, for use by the CERN RD39 team members, by visiting RD39 team members, and by temporary persons such as summer students participating in the work of RD39.

11.6 Technical support at CERN

Cryolab: Technical support is requested at the same level as earlier.

TA1-SSD: Technical support is requested for clean room facilities and for the PS irradiation facility.

EP Microelectronics group: Help and technical support is requested for the assembly and wire bonding of small test devices, at the same level as in the past two years. Technical support or collaboration is also needed for the development of DSM CMOS readout electronics, optimized for cryogenic temperatures.

RD39 has used the CERN services, paid by the users, in the Central Workshop (EST-MF), and in the Electronic Design and Electronic Systems Support groups. These services will be needed in the future at least on the same level as up till now.

11.7 Beams for detector and irradiation tests

As in the past, the Collaboration plans to use the test beams available at CERN, allocated directly to the experiments with which the common projects are set up. A request is made to

have access to the CERN PS irradiation facility, where an *in situ* low-temperature irradiation apparatus is being designed currently.

The planned list of irradiation facilities at CERN and elsewhere includes:

- PS (TA1-SSD) (PS protons)
- Ljubljana (reactor neutrons)
- Karlsruhe (21 MeV protons)
- Debrecen (15 to 16 MeV neutrons up to fluences of 10^{15} cm^{-2}, under discussion)
- Louvain-la-Neuve (primary protons, 10 MeV neutrons up to fluences of 10^{15} cm^{-2}).

12 ACKNOWLEDGEMENTS

This work would not have been possible without the enthusiastic support of several CERN experiments, including in particular the NA60, COMPASS and TOTEM, and we are indebted to their management and participating members. The contributions of the CERN Microelectronics group (Pierre Jarron) and Cryolab (Michel Rieubland) are also gratefully acknowledged. The support of the CMS and ATLAS experiments is greatly appreciated and recognized. The Beam Instrumentation group is thanked for their helpful advice. The Karlsruhe team wishes to thank Dr. Iris Abt from the MPI, Munich, Germany for supplying them with double sided strip detectors from the HERA-B produced by Sintef. The BNL team is supported by the US Dept of Energy, contract No: DE-AC02-98CH10886.